Physics Potential of the India-based Neutrino Observatory (INO)

A Thesis

Submitted to the

Tata Institute of Fundamental Research, Mumbai

For the Degree of Doctor of Philosophy

in Physics

by

Tarak Thakore

Department of High Energy Physics

Tata Institute of Fundamental Research, Mumbai.

May 2014.

Final Version Submitted in November 2014.

DECLARATION

This thesis is a presentation of my original research work. Wherever contributions of others are involved, every effort is made to indicate this clearly, with due reference to the literature, and the acknowledgement of collaborative research and discussions. As this work was carried out within the INO collaboration, the thesis author wishes to state that the ICAL muon simulation and reconstruction algorithms and computer programs were adapted from the work of the other INO collaborators. The analysis strategy and the code for the physics analysis were largely devised by the author, with some inputs from the other collaborators. In addition, the author acknowledges many informal discussions with the senior collaborators, which have been very useful for this work.

The work was done under the guidance of Prof. Naba K Mondal at the Tata Institute of Fundamental Research, Mumbai.
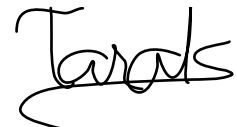
Tarak Thakore

[Candidate's name and signature]

In my capacity as the supervisor of the candidate's thesis, I certify that the above statements are true to the best of my knowledge.

Prof. Naba K Mondal

[Supervisor's name and signature]

Date:

To My Parents
and to the Nature whose manifestations are
grand and infinite

Acknowledgements

First of all, I thank my PhD thesis supervisor Prof. N K Mondal to let me participate in the research work for the ICAL experiment at INO and for his role as a supervisor. I highly appreciate the hard work he is putting in for setting up the ICAL neutrino experiment in India. Secondly, I thank Prof. Amol Dighe for his role as a teacher, a mentor and a collaborator. It has been a pleasant experience to work with him and learning to solve problems efficiently with a clear thinking process.

I also specially thank Prof. D. Indumathi, who got me started with the simulations for the ICAL physics analysis. She is always enthusiastic and energetic to discuss physics, which has greatly encouraged me. I am greatly indebted to my other INO collaborators, Prof. S UmaSankar, Prof. Sandhya Choubey, Prof. Gobinda Majumder, Prof. Srubabati Goswami, Prof. M. Naimuddin, Prof. Prafulla Behera, Prof. Amitava Raychaudhuri, Prof. Sajjad Athar, Prof. Raj Gandhi, Prof. Nita Sinha, Dr. Pomita Ghoshal and Prof. Sanjib Agarwalla. Amongst my peers, I thank Asmita Redij, Kolahal Bhattachraya, Moon Moon Devi, Anushree Ghosh, Sudeshna Dasgupta, Meghana K, Animesh Chatterjee, Kanishka Rawat and Deepak Samuel. All of these people have been of tremendous help while carrying out my thesis work. A special thanks to Dr. B Satyanarayan for being a fantastic mentor to the INO students and for always being a source of encouragement. I also acknowledge many useful discussions with Prof. Thomas Schwetz, Prof. Costas Andreopoulos and Prof. Brett Viren. My thesis work would not have been possible without the support of the computer administration staff members Mr. P Nagraj, Mrs. Noopur Srivastava and Mr. Pavan Vengala.

I have been fortunate to have many good friends with whom I shared a good time at TIFR. Thank you, R. Loganayagam, Sayantan, Vibhor, Sayan, Satyabrata,

Anya, Ganesh, Ashish, Vandna, Atul, Aditya, Sam, John, Dimitra, Richard, Soham, Suratna, Ramkrishna, Nihit, Devdatta, and Satej. I am thankful to everyone in TIFR for making it a wonderful research institution.

Finally, I thank my parents for always being there for me. They have always encouraged me to make progress in my career. I would like to mention that my father introduced me to science and technology at a young age, who explained me about atoms, chemistry, telescopes, microscopes, planets and satellites amongst many other things. He has always been a strong pillar whom I rely upon.

Physics Potential of the India-based Neutrino Observatory (INO)

<u>Thesis Synopsis</u>

Tarak Thakore

Thesis Advisor : Prof. Naba K Mondal

Department of High Energy Physics

Tata Institute of Fundamental Research

1 Neutrino Oscillations

Neutrino oscillations have been well established by several experiments over last 10 years. They provide a proof for massive neutrinos. In the standard model of particle physics, neutrinos are massless particles. Therefore, the discovery of massive neutrinos provide important hints for the physics beyond the standard model. Neutrino oscillations arise, because the neutrino mass eigenstates and the flavor eigenstates are not coincident, but are connected by a unitary transformation (U_{PMNS}). This is illustrated graphically in Fig. 1.
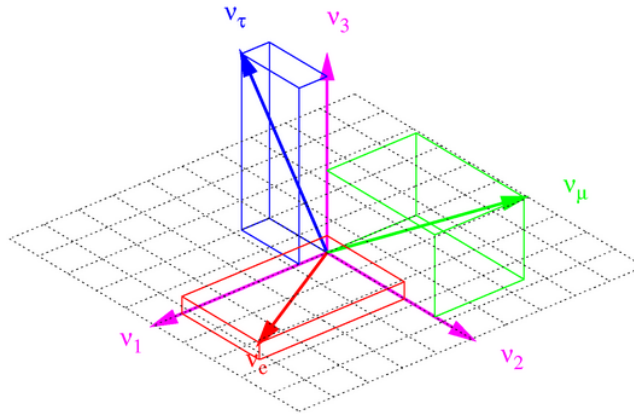

Figure 1: An Illustration of neutrino mass states rotated away from the flavor states

All neutrino oscillation experimental data (with the exception of two experiments), can be explained in the 3 neutrino oscillation framework. Pontecorvo–Maki–Nakagawa–Sakata mixing matrix U_{PMNS} [1, 2] for three neutrino flavors can be expressed as Eqn. 1. It is described in terms of three mixing angles, one CP violating phase and two Majorana phases.

$$U_{\text{PMNS}} = \begin{pmatrix} 1 & 0 & 0 \\ 0 & c_{23} & s_{23} \\ 0 & -s_{23} & c_{23} \end{pmatrix} \begin{pmatrix} c_{13} & 0 & s_{13}e^{-i\delta_{\text{CP}}} \\ 0 & 1 & 0 \\ -s_{13}e^{i\delta_{\text{CP}}} & 0 & c_{13} \end{pmatrix} \begin{pmatrix} c_{12} & s_{12} & 0 \\ -s_{12} & c_{12} & 0 \\ 0 & 0 & 1 \end{pmatrix} \begin{pmatrix} e^{i\alpha_1/2} & 0 & 0 \\ 0 & e^{i\alpha_2/2} & 0 \\ 0 & 0 & 1 \end{pmatrix},$$

$$\tag{1}$$

where $c_{ij} = \cos\theta_{ij}$ and $s_{ij} = \sin\theta_{ij}$. Here δ_{CP} is the CP violating phase and α_1 and α_2 are the Majorana phases. In Eqn. 1, the first matrix is related with the atmospheric neutrino oscillations, the second matrix with the reactor neutrino oscillations and the third matrix with the solar neutrino oscillations. The fourth matrix describes the Dirac or Majorana nature of neutrinos and is not observable in the oscillation experiments. The second matrix also contains the CP violating phase δ_{CP}. The amplitude of the oscillations is governed by these three mixing angles, whereas the frequency of the oscillations is determined by the mass squared differences $\Delta m_{ij}^2 = m_i^2 - m_j^2$. One of the mass squared difference, Δm_{31}^2, is related with the atmospheric neutrino oscillations and the other Δm_{21}^2, is related to the solar neutrino oscillations. The neutrino mass states can have two possible arrangements as shown in Fig. 2, known as the normal mass hierarchy (NH) and the inverted mass hierarchy (IH). Neutrino oscillation probabilities can significantly be modified while passing through matter due to forward scattering of electron neutrinos, known as the Mikheyev-Smirnov-Wolfesnstin (MSW) effect [3, 4] .
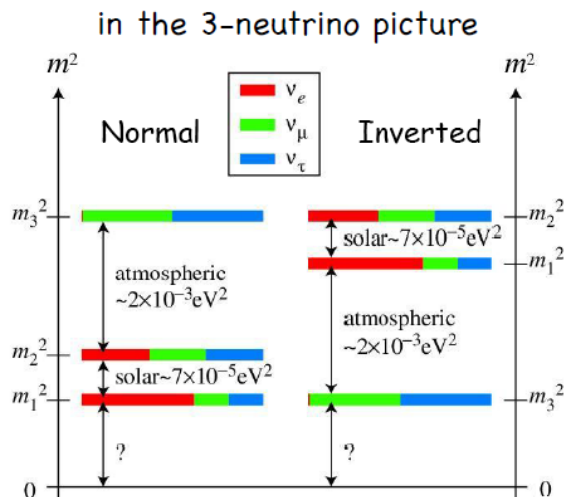

Figure 2: Neutrino mass hierarchy, Left : Normal, Right : Inverted

Various solar, atmospheric, accelerator and reactor neutrino experiments have made measurements of these oscillation parameters. A summary of best fit oscillation parameters values from the global neutrino data analysis is indicated in Table 1. While both the magnitude and the sign of Δm_{21}^2 is known experimentally, only the magnitude of Δm_{31}^2 is currently known. Hence the neutrino mass hierarchy is not yet known. The absolute neutrino mass scales are also unknown, we only have upper bounds on them from cosmological data [5, 6, 7], from neutrinoless double beta decay [8, 9], and from tritium beta decay experiments. [10, 11]

Parameter	Best Fit Value	3σ Bounds
$\sin^2\theta_{12}$	0.307	0.259-0.359
$\sin^2\theta_{23}$	0.386	0.331-0.637 (NH)
	0.392	0.335-0.663 (IH)
$\sin^2\theta_{13}$	0.0241	0.0169-0.0313 (NH)
	0.0244	0.0171-0.0315 (IH)
Δm_{21}^2 (eV^2)	7.54×10^{-5}	$6.99\text{-}8.18 \times 10^{-5}$
$\|\Delta m_{31}^2\|$ (eV^2)	2.43×10^{-3}	$2.19\text{-}2.62 \times 10^{-3}$ (NH)
	2.42×10^{-3}	$2.17\text{-}2.61 \times 10^{-3}$ (IH)

Table 1: Summary of current best-fit neutrino oscillation parameter values from a global fit [12].

With the last unknown mixing angle θ_{13} measured recently, the current and planned neutrino experiments will now focus on the precision measurements of the oscillation parameters, and more importantly, on the determination of the mass hierarchy and the value of δ_{CP}.

The Iron CALorimeter(ICAL) at the India-based Neutrino Observatory(INO) is a planned experiment, which will make precision measurement of the parameters ($\sin^2\theta_{23}$, $|\Delta m_{32}^2|$), and determine the neutrino mass hierarchy. It will also try to measure deviation of θ_{23} from the maximal mixing value as well as its octant[13]. Additionally, the ICAL detector may be able to provide limits on Non-Standard Neutrino Interactions(NSI) and sterile neutrino mixing.

In this thesis, we study the response of the ICAL detector with GEANT4 simulations to muons and parametrize it. Using this muon response, we obtain the sensitivity of the ICAL to make precision measurement of the atmospheric oscillation parameters ($\sin^2\theta_{23}$, $|\Delta m_{32}^2|$) and for determining the neutrino mass hierarchy.

2 The INO Experiment

The India-based Neutrino Observatory(INO) will be located in the Bodi West Hills in Theni district of Tamilnadu in Southern India. The cavern will be set up under a 1589 m high mountain peak. This peak provides a minimum rock cover of 1 km in all directions to reduce the cosmic muon background. The ICAL detector setup will be housed in this cavern. The ICAL detector consists of 150 alternate layers of 5.6 cm thick iron plates and Resistive Plate Chambers (RPCs) stacked vertically. The total mass of the detector is 50 kt. The iron plates act as the target mass for neutrino interactions and the RPCs as the active detector elements. The iron plates are magnetized with a field of 1.3–1.5 Tesla, which enables the charge identification for the muons. The ICAL detector will primarily measure CC ν_μ interactions. Muon charge identification capability is essential to determine the neutrino mass hierarchy using the earth matter effects in neutrino oscillations.

As the outgoing leptons and hadrons produced in a neutrino interaction propagate through the detector volume, they give hit points in the RPCs. For every hit point, the (x,y) position, time of hit, and the RPC layer number are recorded. The information contained in the hit points is used to reconstruct the energy and direction of the particles. A muon passing through the ICAL detector typically gives hit points in several layers which can be cleanly joined to form a track. In contrast, a pion or other hadron passing though the detector give rise to a hadron shower with multiple hit points in single layers which cannot be joined to form a track.

The ICAL setup is optimized primarily to measure the muon momentum with good precision. Energy, direction and the charge of muons are reconstructed as discussed in the following section.

The hadron energy and direction can be calibrated based on the number of hit points. By combining the muon and hadron information, the neutrino momentum can be reconstructed.

3 Muon Reconstruction for the ICAL detector

A precise measurement of the muon energy and direction with good efficiencies is crucial in order to achieve the oscillation physics goals for the ICAL detector. A GEANT4-based toolkit for the ICAL detector simulation has been developed by the INO collaboration. The reconstruction code employs a Kalman Filter derived algorithm. It has been used to obtain the ICAL response to muons.

GEANT4 is used to simulate the propagation of particles in the ICAL detector taking into account various interaction processes(electromagnetic and strong interactions) as well as the magnetic field that a particle experiences during its travel in the detector. This simulation gives the position of the particle in the active detector elements (RPCs). The hit position is then digitized to obtain the location number of X and Y direction strips of RPCs that become active.

3.1 Muon Track Reconstruction Algorithm

The task of the muon reconstruction algorithm is to use the measured hit point positions to determine the interaction vertex position, energy, direction and charge of muons produced in neutrino interaction with good accuracy and efficiency. Muon reconstruction is done in two steps : (i) Track Finding, (ii) Track Fitting.

1. Track Finding : The topology of the hit points is analyzed to determine whether the hit points can be joined to form a long track or they form a hadron shower.

2. Track Fitter : If the hit points are found to be forming a track, then a Kalman Filter based algorithm is used to reconstruct the muon momentum at the vertex position. It also determines the charge of the muon.

3.2 Muon Response Parametrization

In the data analysis of a real experiment, we would use the reconstructed energy and direction of particles. This would involve passing the generator level particle information through the reconstruction code, imposing various cuts on events based on the position of the hit points and the goodness of track reconstruction. However, in the current work, we characterize the detector response to muons in terms four key quantities, in the form of a look-up table. This table is used to obtain the measured distribution of muons from the true distribution as explained in Section 4. We have parametrized the response of the ICAL detector in terms of (i) energy resolution (σ_E), (ii) zenith angle resolution ($\sigma_{\cos\theta}$), (iii) reconstruction efficiency (ϵ_R), and (iv) charge identification efficiency (CID) (ϵ_C). All these quantities are estimated as a function of true muon energy (E_μ) and direction ($\cos\theta_\mu$), separately for μ^- and μ^+.

The vertex position of the muons is set in the central volume of the detector with a uniform smearing of $\pm$(400,400,600) cm around the point (0,0,0), which is the centre of the detector. The magnetic field is approximately uniform in this region except for the boundaries. We assume that the detector response obtained in this region can be extrapolated to the entire volume of the detector.[1] The azimuthal angle ϕ is smeared uniformly between $0 - 2\pi$. The energy and

---

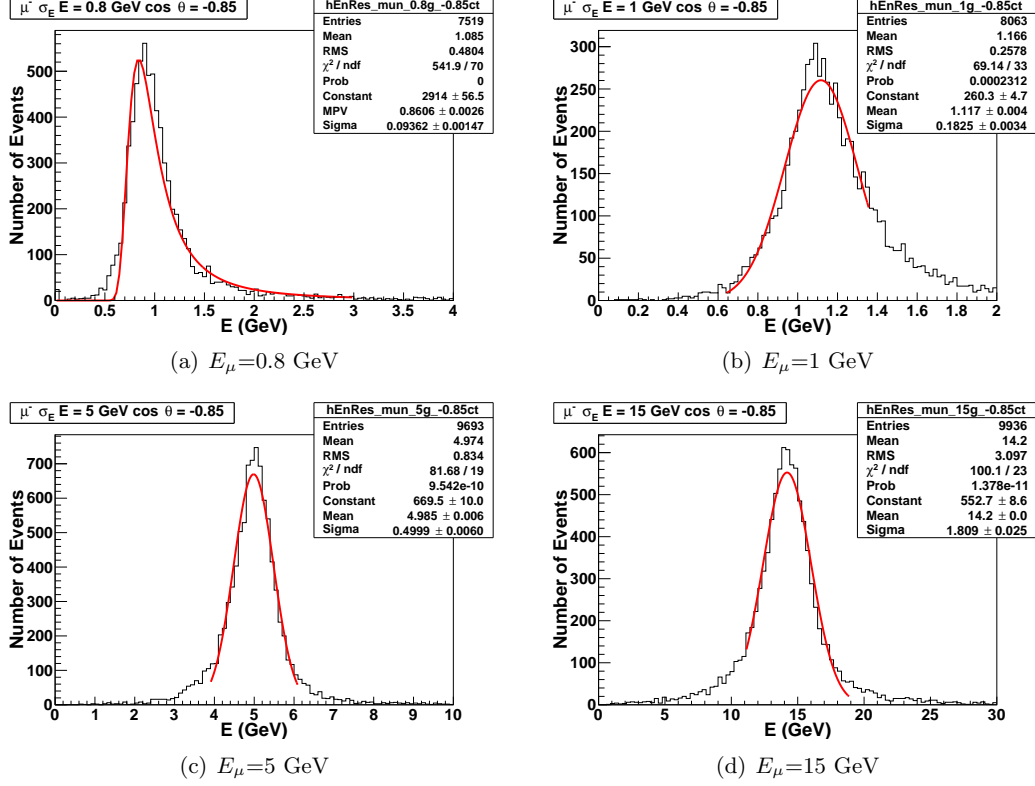[1]The assumptions made here will be relaxed as the ICAL detector simulations progress.

Figure 3: Reconstructed energy distribution for $\cos\theta_\mu$=-0.85 for four different muon energies : (a) E_μ=0.8 GeV, (b) E_μ=1 GeV, (c) E_μ=5 GeV, and (d) E_μ=15 GeV

direction (E_μ, $\cos\theta_\mu$) are not smeared. We have prepared the look-up table in the range, E_μ = [0.6,25] GeV (20 sample points), and for $\cos\theta = [-1,1]$ (20 sample points). For each one of the 400 possible combination of energy and direction, we simulate 10,000 μ^- (μ^+) in the detector with GEANT4, digitize and reconstruct them with the ICAL reconstruction code. We obtain the resolutions and efficiencies at a particular (E_μ, $\cos\theta_\mu$) point from the distribution of the reconstructed energy and direction.

Fig. 3 and Fig. 4 show a few distributions of the reconstructed E and $\cos\theta$, respectively. The same figures also show the fits used to obtain the resolutions. We fit the Landau distribution function to the distribution of reconstructed energy for $E_\mu < 1$ GeV, while the normal distribution function is used for fitting with $E_\mu \geq 1$ GeV. As we see from Fig. 3, the reconstructed energy distributions have tails on one or both sides and we cannot fit them with the normal distribution function in the full range. These tails arise because the muon reconstruction algorithm has not yet been completely fine tuned. For example, in cases, where a muon is passing through the support structure, the current reconstruction algorithm doesn't work well. A Landau distribution convoluted with the Gaussian would make more appropriate fits to these reconstruction distributions. However, in this analysis, we perform fits with the normal distribution function around the peak of the distribution, in the range [$E\mu$ - FWHM, E_μ + FWHM], where FWHM is the full width at half maxima found from the distribution. The energy resolution (σ_E) is obtained from this fit. We define the reconstruction efficiency as the ratio of the number of events in the range [E - $3\sigma_E$, E + $3\sigma_E$] to the number of incident events (10,000), while the CID efficiency is defined to be the ratio of the number of events reconstructed

5

with the correct charge to the total number of reconstructed events (in the same range). For the reconstructed $\cos\theta$ distributions, double-Gaussian function fits might be used. However, for simplicity in the analysis, the $\cos\theta$ resolution is obtained by fitting the normal distribution function to the reconstructed $\cos\theta$ distribution in all cases.
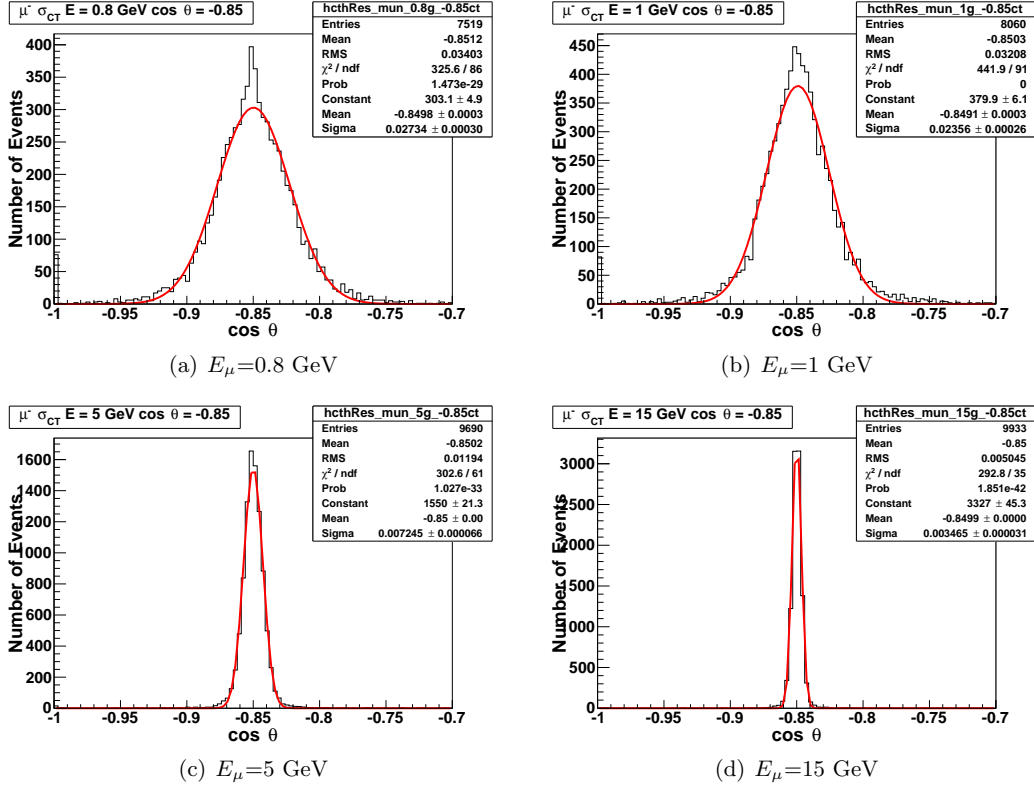

Figure 4: Reconstructed $cos\theta$ distribution for $\cos\theta_\mu$=-0.85 for four different muon energies : (a) E_μ=0.8 GeV, (b) E_μ=1 GeV, (c) E_μ=5 GeV, and (d) E_μ=15 GeV

Fig. 5 shows the energy and direction resolutions as well as the reconstruction and charge identification efficiency for μ^-. Depending on the true energy and direction the energy resolution vary between 10% to 22% and angular resolutions of 1° to 2° are achieved. The efficiency of reconstruction is found between 15–99 %. The CID efficiency is always better than 90%. We notice that the energy resolution improves up to 8 GeV and then starts to degrade with increasing energy for all angles. The angular resolution, the reconstruction efficiency and the CID efficiency improve with energy.

4   Oscillation Analysis Procedure

The oscillation analysis is carried out in four steps : (i) neutrino event generation, (ii) inclusion of the oscillation effects, (iii) folding in the detector response, and finally, (iv) the χ^2 analysis.

4.1   Event Generation

We use the neutrino event generator NUANCE (version 3.5) [14] to simulate neutrino interactions. The atmospheric neutrino fluxes provided by Honda et al. [15] at the Super Kamiokande

6

(a) Energy Resolution   (b) $\cos \theta_\mu$ Resolution

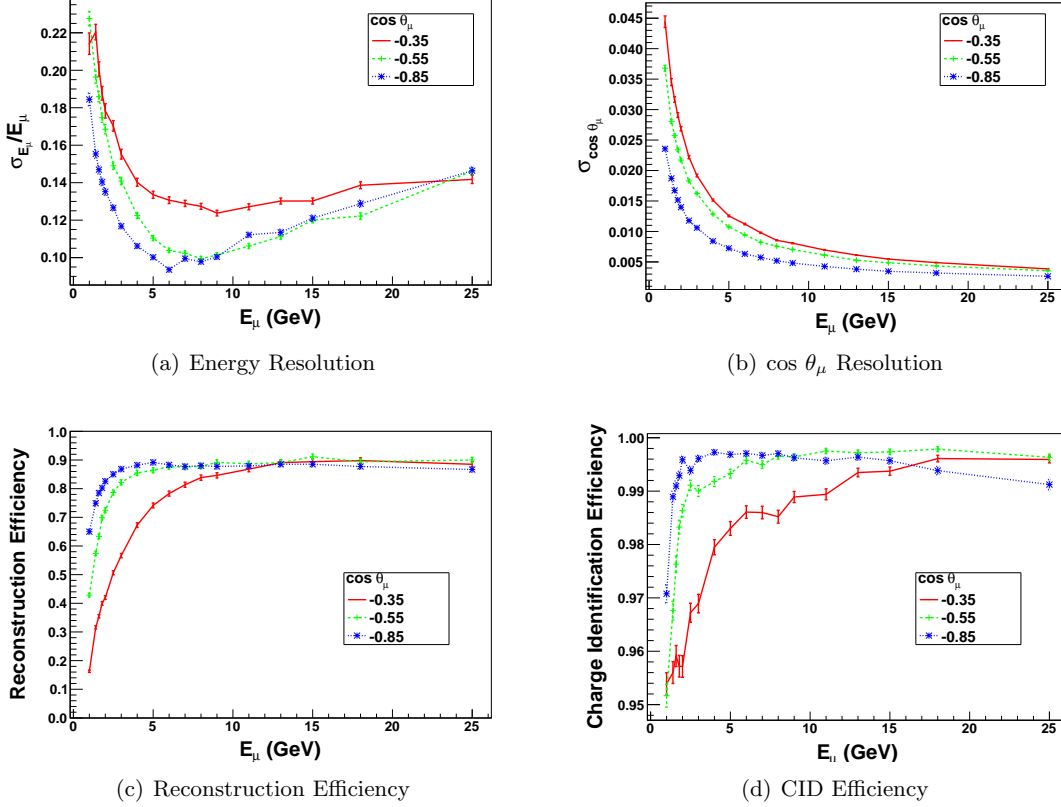(c) Reconstruction Efficiency   (d) CID Efficiency

Figure 5: The energy resolution (a), $\cos \theta_\mu$ resolution (b), the reconstruction efficiency (c), and the charge identification efficiencies (d), for μ^- as a function of the true muon energy and for three cases of true muon zenith angle. The red, green and blue lines are for the zenith angle bins with $\cos \theta_\mu = (-0.4, -0.3), (-0.6, -0.5), (-0.9, -0.8)$ respectively.

location are used. The ICAL detector composition and geometry are specified as an input. We generate CC ν_μ events for a large exposure of 1000 years $\times$ 50 kt, and scale it down to 10 years $\times$ 50 kt(or other required exposure). We do so in order to reduce the statistical fluctuations, that are introduced by NUANCE in the exact event rates. Since it is not possible to generate this large event-set for all possible oscillation parameters, we generate these events using un-oscillated neutrino fluxes and later include the oscillation effects using the Re-Weighting method.

4.2 Re-Weighting Method

The total number of ν_μ events coming from $\nu_\mu \to \nu_\mu$ and $\nu_e \to \nu_\mu$ channels is :

$$\frac{d^2N}{dE_\nu \, d(\cos \theta_\nu)} = N_T \times N_D \times \sigma_{\nu_\mu} \times \left[P_{\mu\mu} \frac{d^2\Phi_{\nu_\mu}}{dE_\nu \, d(\cos \theta_\nu)} + P_{e\mu} \frac{d^2\Phi_{\nu_e}}{dE_\nu \, d(\cos \theta_\nu)} \right], \qquad (2)$$

where N_T is the exposure time and N_D is the number of nucleons in the detector. Here Φ_{ν_μ} and Φ_{ν_e} are the fluxes of ν_μ and ν_e respectively, and $P_{\alpha\beta}$ is the $\nu_\alpha \to \nu_\beta$ oscillation probability. In order to include the oscillation effects in our NUANCE event sample, we apply the Re-Weighting method as follows.

7

To obtain the number of μ^- events from ν_μ that have survived oscillations, we first calculate the oscillation probabilities $P_{\mu\beta}$ ($\beta = e, \mu, \tau$) using its true neutrino energy (E_ν) and zenith angle (θ_ν). We compare these probabilities with a uniform random number r in the range [0,1]. If $P_{\mu e} \leq r < P_{\mu e} + P_{\mu\mu}$, we keep this event as a ν_μ event. Otherwise this ν_μ is considered to have oscillated into a different flavor. An analogous procedure is used to obtain the number of μ^- events from atmospheric ν_e oscillated into ν_μ. The events from these two oscillation channels are combined to get the total number of μ^- events. Similarly, we form the μ^+ event sample.

After obtaining the oscillated μ^- and μ^+ events, we bin them according to energy (E_μ) and direction ($\cos\theta_\mu$) in the range $E_\mu = [0.5,15.5]$ GeV (300 bins) and $\cos\theta_\mu = [-1,1]$ (20 bins). We keep track of μ^- and μ^+ events separately. At this stage, we have the distribution of muon events in terms of their "true" energy (E_μ) and the cosine of the zenith angle ($\cos\theta_\mu$).

4.3 Folding in the Detector Response

The detector response is folded in next. We apply the reconstruction efficiency (ϵ_{R-}) for μ^- by multiplying the number of events in a given true energy (E_μ) and true zenith angle ($\cos\theta_\mu$) bin with the corresponding reconstruction efficiency:

$$N_{\mu-}(E_\mu, \cos\theta_\mu) = \epsilon_{R-}(E_\mu, \cos\theta_\mu) \times N_{\mu-}^{\text{true}}(E_\mu, \cos\theta_\mu)\,, \tag{3}$$

where $N_{\mu-}^{\text{true}}$ is the number of μ^- events in a given ($E_\mu, \cos\theta_\mu$) bin. Exactly the same procedure is used for determining the μ^+ events. The CID efficiency (ϵ_{C-} for μ^- and ϵ_{C+} for μ^+ event sample) is next applied as follows:

$$N_{\mu-}^C = \epsilon_{C-} \times N_{\mu-} + (1 - \epsilon_{C+}) \times N_{\mu+}\,, \tag{4}$$

where $N_{\mu-}$ and $N_{\mu+}$ are the number of μ^- and μ^+ events, respectively, given by Eqn. (3). Now $N_{\mu-}^C$ is the number of μ^- events after taking care of the CID efficiency. All the quantities appearing in Eqn. (4) are functions of E_μ and $\cos\theta_\mu$.

Finally, the muon resolutions σ_E and $\sigma_{\cos\theta}$ are applied as follows:

$$(N_{\mu-}^D)_{ij} = \sum_k \sum_l N_{\mu-}^C(E_\mu^k, \cos\theta_\mu^l)\, K_i^k(E_\mu^k)\, M_j^l(\cos\theta_\mu^l)\,, \tag{5}$$

where $(N_{\mu-}^D)_{ij}$ denotes the number of muon events in the ith E-bin and the jth $\cos\theta$-bin after applying the energy and angle resolutions. Here E and $\cos\theta$ are the measured muon energy and zenith angle. The summation is over the true energy bin k and true zenith angle bin l, with E_μ^k and $\cos\theta_\mu^l$ being the central values of the kth true muon energy and l^{th} true muon zenith angle bin. The quantities K_i^k and M_j^l are the integrals of the detector resolution functions over the bins of E and $\cos\theta$, the measured energy and direction of the muon, respectively. These are evaluated as:

$$K_i^k(E_\mu^k) = \int_{E_{L_i}}^{E_{H_i}} dE \frac{1}{\sqrt{2\pi}\sigma_{E_\mu^k}} \exp\left(-\frac{(E_\mu^k - E)^2}{2\sigma_{E_\mu^k}^2}\right)\,, \tag{6}$$

and

$$M_j^l(\cos\theta_\mu^l) = \int_{\cos\theta_{L_j}}^{\cos\theta_{H_j}} d\cos\theta \frac{1}{\sqrt{2\pi}\sigma_{\cos\theta_\mu^l}} \exp\left(-\frac{(\cos\theta_\mu^l - \cos\theta)^2}{2\sigma_{\cos\theta_\mu^l}^2}\right)\,, \tag{7}$$

where $\sigma_{E_\mu^k}$ and $\sigma_{\cos\theta_\mu^l}$ are the energy and zenith angle resolutions, respectively, in these bins. We perform the integrations between the lower and upper boundaries of the measured energy (E_{L_i} and E_{H_i}) and the measured zenith angle ($\cos\theta_{L_j}$ and $\cos\theta_{H_j}$). At this stage, we get the measured distribution of the muon events.

4.4 The χ^2 Analysis

Muon events are re-binned in wider bins for the χ^2 analysis. We use the Poisson definition of χ^2 as :

$$\chi^2_{\text{ino}}(\mu^-) = \min_{\xi_k} \sum_{i=1}^{N_E} \sum_{j=1}^{N_{\cos\theta}} \left[2(N_{ij}^{\text{pred}} - N_{ij}^{\text{obs}}) - 2N_{ij}^{\text{obs}} \ln\left(\frac{N_{ij}^{\text{pred}}}{N_{ij}^{\text{obs}}}\right) \right] + \sum_{k=1}^{5} \xi_k^2 , \qquad (8)$$

with

$$N_{ij}^{\text{pred}} = N_{ij}^0 \left(1 + \sum_{k=1}^{5} \pi_{ij}^k \xi_k \right). \qquad (9)$$

Here N_{ij}^{pred} and N_{ij}^{obs} are expected and observed number of μ^- events in a given $(E, \cos\theta)$ bin. N_E and $N_{\cos\theta}$ are the number of energy and $\cos\theta$ bins, respectively. N_{ij}^{obs} is calculated for a set of assumed "true value" of the oscillation parameters. N_{ij}^0 is the predicted number of events for a given set of oscillation parameters without the systematic errors included. The systematic uncertainties are included via the "pull" variables ξ_k, one each for every systematic uncertainty σ_k [16]. Here π_{ij}^k is the change in the number of events in the $(ij)^{\text{th}}$ bin caused by varying the value of kth pull variable ξ_k by σ_k.

In this analysis we have considered the following five systematic uncertainties. We take 20% error on the flux normalization, 10% error on cross sections, and an overall 5% error on the total number of events. In addition, we take a 5% uncertainty on the zenith angle dependence of the flux, and an energy dependent "tilt error" is included according to the following prescription. The event spectrum is calculated with the predicted atmospheric neutrino fluxes and then with the flux spectrum shifted according to

$$\Phi_\delta(E) = \Phi_0(E) \left(\frac{E}{E_0}\right)^\delta \simeq \Phi_0(E) \left(1 + \delta \ln \frac{E}{E_0}\right), \qquad (10)$$

where $E_0 = 2$ GeV and δ is the 1σ systematic tilt error, taken to be 5%. The difference between $\Phi_\delta(E)$ and $\Phi_0(E)$ is then included as the error on the flux.

For each set of oscillation parameters, we calculate χ^2 separately for the μ^- and μ^+ data samples, and add them to obtain the total χ^2 as

$$\chi^2_{\text{ino}} = \chi^2_{\text{ino}}(\mu^-) + \chi^2_{\text{ino}}(\mu^+). \qquad (11)$$

This χ^2_{ino} is used obtain our results for the precision measurement of the oscillation parameters and the mass hierarchy sensitivity, after adding suitable priors for oscillation parameters.

5 Precision Measurement of the atmospheric oscillation parameters

We describe our results on the precision measurements of $(\sin^2\theta_{23}, |\Delta m^2_{32}|)$ in this section. For the results presented in this section, we take $N_E = 10$ (in the range $E_\mu = [0.8, 10.8]$ GeV) and $N_{\cos\theta} = 20$ (in the range $\cos\theta_\mu = [-1,1]$) in Eqn. 8. The true values of oscillation parameters are given in Table 2 for the results presented in this section, unless specified otherwise.

Parameter	$\sin^2 2\theta_{12}$	$\sin^2 2\theta_{23}$	$\sin^2 2\theta_{13}$	Δm^2_{21} (eV^2)	$|\Delta m^2_{32}|$ (eV^2)	δ_{CP}	Hierarchy
True Value	0.86	1.0	0.113	7.6×10^{-5}	2.424×10^{-3}	0.0	Normal

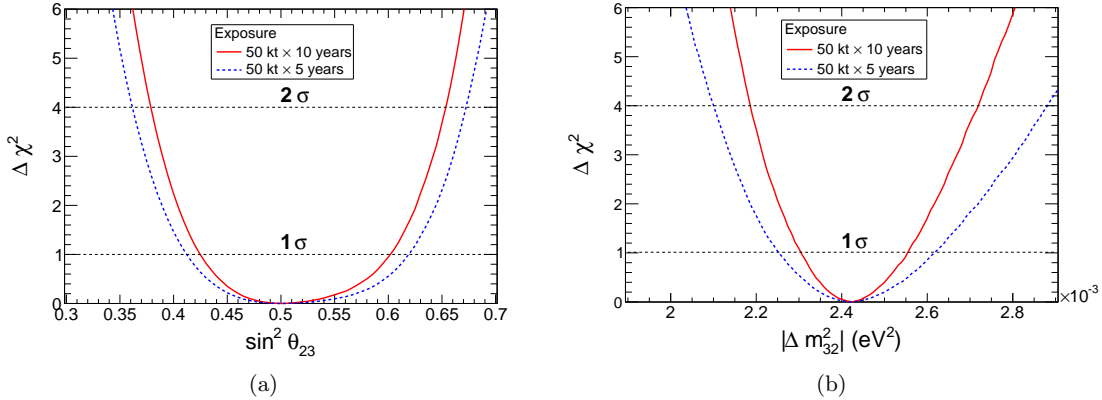Table 2: True values of oscillation parameters used for the precision measurement analysis

Figure 6: The panel (a) shows the χ^2 as a function of $\sin^2\theta_{23}$ for $|\Delta m^2_{32}| = 2.424 \times 10^{-3}$ eV^2 and $\sin^2\theta_{23}(\text{true}) = 0.5$. The panel (b) shows the χ^2 as a function of $|\Delta m^2_{32}|$ for $\sin^2\theta_{23} = 0.5$ and $|\Delta m^2_{32}|(\text{true}) = 2.424 \times 10^{-3}$ eV^2

We consider the solar oscillation parameters θ_{12} and $|\Delta m^2_{21}|$ to be fixed. A prior is imposed on the parameter $\sin^2 2\theta_{13}$ to allow for the uncertainty in its current measurement :

$$\chi^2 = \chi^2_{\text{ino}} + \left(\frac{\sin^2 2\theta_{13}(\text{true}) - \sin^2 2\theta_{13}}{\sigma_{\sin^2 2\theta_{13}}} \right)^2 , \tag{12}$$

where $\sigma_{\sin^2 2\theta_{13}}$ is the 1σ error on $\sin^2 2\theta_{13}$, taken to be 0.013.

5.1 Constraining $(\sin^2\theta_{23}, |\Delta m^2_{32}|)$ with ICAL

We use the parameter Δm^2_{32} ($= \Delta m^2_{31}$ - Δm^2_{21}) instead of $|\Delta m^2_{31}|$. The χ^2 as functions of $\sin^2\theta_{23}$ and $|\Delta m^2_{32}|$ is shown in Fig. 6(a) and Fig. 6(b), respectively.

The precision on these parameters is defined as :

$$\text{precision} = \frac{p_{max} - p_{min}}{p_{max} + p_{min}} , \tag{13}$$

where p_{max} and p_{min} are the largest and smallest value of the concerned oscillation parameters determined at the given C.L. from the atmospheric neutrino measurements at ICAL for a given exposure.

We find that after 5 years run, the ICAL would be able to measure $\sin^2\theta_{23}$ to a precision of 20% and $|\Delta m^2_{32}|$ to 7.4% at 1σ. With 10 years exposure, these numbers improve to 17% and 5.1%. The observed asymmetry in χ^2 as a function of $\sin^2\theta_{23}$ is a result of non-zero θ_{13}. The correlated reach of ICAL for these parameters is shown in Fig. 7(a) and Fig. 7(b) for 5 and 10 years of operation.

In Fig. 8 we show the comparison of ICAL with other experiments on the precision reach of $(\sin^2\theta_{23}, |\Delta m^2_{32}|)$. We observe that, with 5 years of exposure, ICAL will be able to almost match the precision on $|\Delta m^2_{32}|$ obtained from the SK L/E analysis currently. With 10 years data this will improve, though it will still not be comparable to the precision we already have from the MINOS experiment. The precision of ICAL on $\sin^2 2\theta_{23}$ in 10 years may be expected to be comparable to the T2K result[17] released recently. We can see that the sensitivity of ICAL to $\sin^2 2\theta_{23}$ and $|\Delta m^2_{32}|$ is not expected to surpass the precision we already have from the currently operating experiments. However, the ICAL data will be used for global neutrino data analysis.
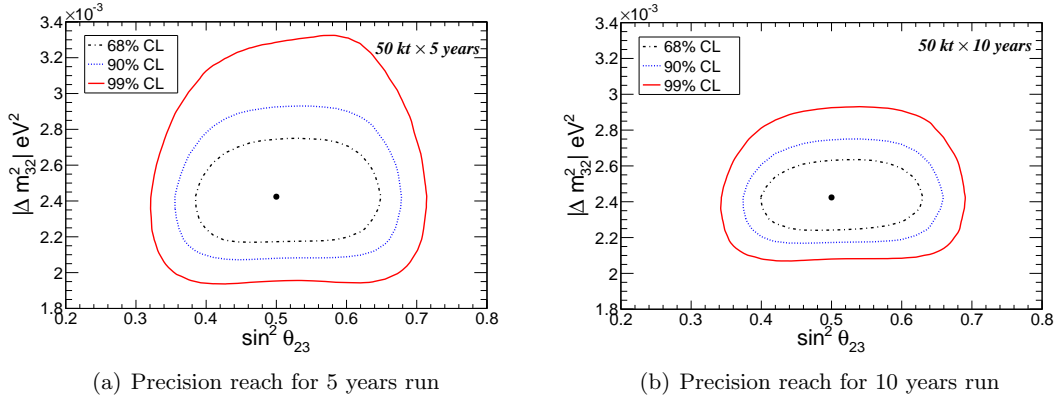
10

(a) Precision reach for 5 years run   (b) Precision reach for 10 years run

Figure 7: The precision reach expected at ICAL in the $\sin^2\theta_{23} - |\Delta m^2_{32}|$ plane at various confidence levels. The black(broken), blue(dotted) and red(solid) lines show 68%, 90% and 99% C.L. contours. The true values of $\sin^2\theta_{23}$ and $|\Delta m^2_{32}|$ used for generating data are shown by the black dots. The true values of other parameters used are given in Table 2. Panel (a) is for five-year running of the 50 kt detector while (b) is for ten years exposure.
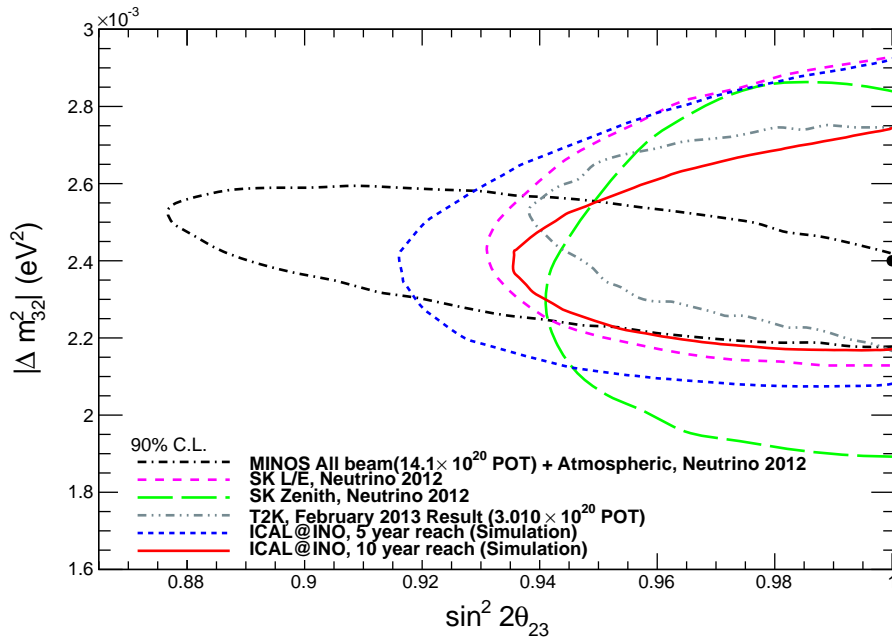
Figure 8: Comparison of the reach of ICAL@INO with the current results from other neutrino experiments. The black dot in the figure denotes the point where the ICAL data was generated. The true values of the other oscillation parameters are given in Table 2.

5.2 Sensitivity to probe θ_{23} Deviations from Maximal Mixing and its Octant Determination

Earth matter effects in atmospheric neutrinos can be used to probe deviations in θ_{23} from the maximal mixing and can lead to the determination of the correct θ_{23} octant [18, 19, 20]. We show in Fig. 9 the potential of 10 years of ICAL run for distinguishing a non-maximal value of θ_{23} from maximal mixing in the cases where $\sin^2 2\theta_{23} = 0.90$ ($\sin^2 \theta_{23} = 0.342, 0.658$) and $\sin^2 2\theta_{23} = 0.95$ ($\sin^2 \theta_{23} = 0.388, 0.612$). Note that the current 3σ allowed range of $\sin^2 2\theta_{23}$ is $(0.91, 1.0)$. The figure shows that, if the value of θ_{23} is near the current 3σ bound and in the first octant, then it may be possible to exclude maximal mixing to 99% C.L. If θ_{23} is in the second octant, or if $\sin^2 2\theta_{23}$ is larger than 0.9, the exclusion of the maximal mixing becomes a much harder task.

(a) $\sin^2 2\theta_{23} = 0.9$, first octant ($\sin^2 \theta_{23} = 0.342$)

(b) $\sin^2 2\theta_{23} = 0.9$, second octant ($\sin^2 \theta_{23} = 0.658$)

(c) $\sin^2 2\theta_{23} = 0.95$, first octant ($\sin^2 \theta_{23} = 0.388$)

(d) $\sin^2 2\theta_{23} = 0.95$, second octant ($\sin^2 \theta_{23} = 0.612$)
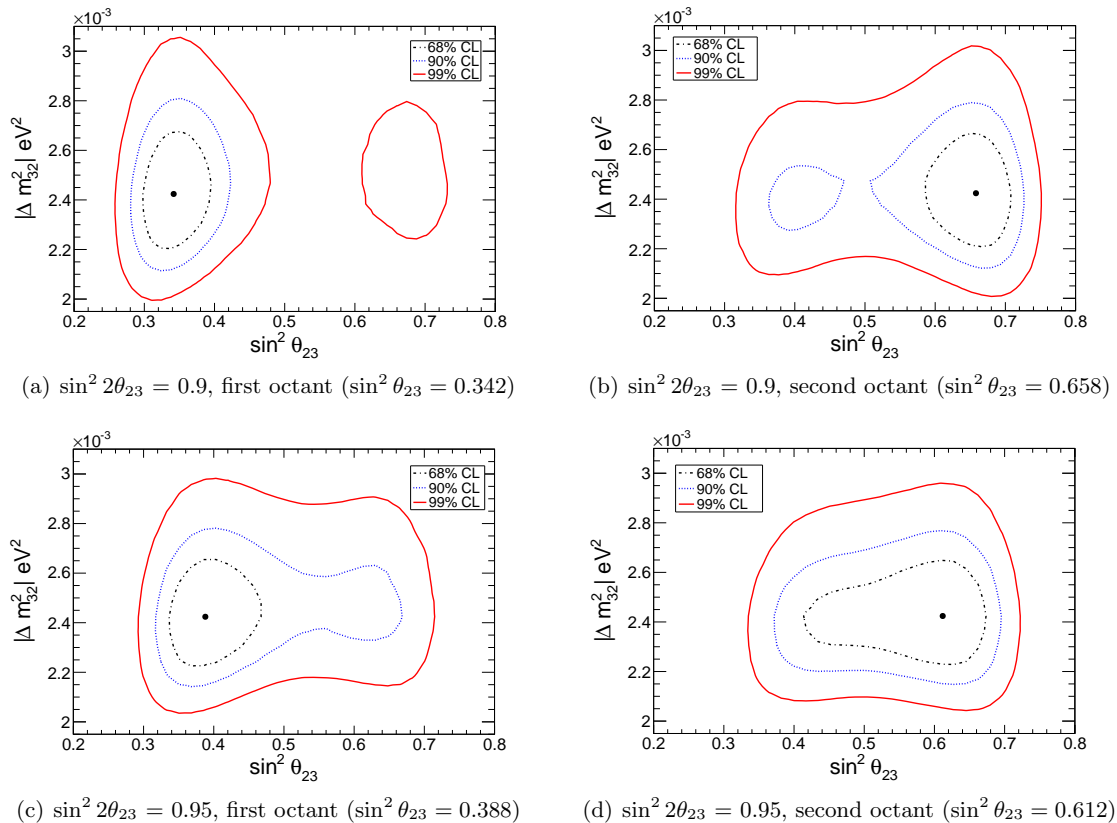
Figure 9: The projected reach in the $\sin^2 \theta_{23} - |\Delta m_{32}^2|$ plane for four different non-maximal choices of θ_{23}. The black(broken), blue(dotted) and red(solid) lines show 68%, 90% and 99% C.L. contours for 10 years of 50 kt ICAL run. Note that we use normal hierarchy, and assume that it is already known.

Fig. 9 can also be used to quantify the reach of ICAL for determining the correct octant of θ_{23}, if the value of $\sin^2 2\theta_{23}$ is known. This can be seen by comparing the χ^2 value corresponding to the true value of $\sin^2 \theta_{23}$, but in the wrong octant, with that corresponding to the true value of $\sin^2 \theta_{23}$. We find that, for $\sin^2 2\theta_{23} = 0.9$, i.e. just at the allowed 3σ bound, the octant can be identified at $>95\%$ C.L. with 10 years of ICAL run if θ_{23} is in the first octant. However if θ_{23} is in the second octant, the identification of the octant would be much harder: θ_{23} in the

wrong octant can be disfavored only to about 85% C.L.. The situation is more pessimistic if $\sin^2 2\theta_{23}$ is closer to unity.

6 Neutrino Mass Hierarchy Sensitivity

This section describes the sensitivity of the ICAL experiment in determining the neutrino mass hierarchy. Relatively large θ_{13} value has opened up the possibility of determining the mass hierarchy in the near future. It has been shown in [21] that a magnetized detector with fine resolutions is a good option to determine the mass hierarchy. The ICAL detector will attempt this task using the earth matter effects in the atmospheric neutrinos. Matter effects give rise to different event rates for μ^+ and μ^- in the detector. The charge identification efficiency of ICAL plays an essential role here to observe ν_μ and $\overline{\nu}_\mu$ separately.

ICAL can rule out the wrong mass hierarchy with a significance of nσ, where n = $\sqrt{\Delta\chi^2_{\text{ino}}}$, and

$$\Delta\chi^2_{\text{ino}} = \chi^2_{\text{ino}}(\text{false}) - \chi^2_{\text{ino}}(\text{true}). \tag{14}$$

Here $\chi^2_{\text{ino}}(\text{true})$ is calculated by fitting the true mass hierarchy to the observed data set and $\chi^2_{\text{ino}}(\text{false})$ is calculated by fitting the wrong mass hierarchy to the observed data set. Hence, $\Delta\chi^2_{\text{ino}}$ gives the statistical significance for ruling out the wrong mass hierarchy.

For the results described in this section, we use Δm^2_{eff} [22] instead of Δm^2_{31}, in order to have a consistent definition for the neutrino mass hierarchy, defined as :

$$\Delta m^2_{\text{eff}} = \Delta m^2_{31} - (\cos^2\theta_{12} - \cos\delta_{\text{CP}}\sin\theta_{13}\sin 2\theta_{12}\tan\theta_{23})\Delta m^2_{21} . \tag{15}$$

The mass hierarchy is defined to be normal, when $\Delta m^2_{\text{eff}} > 0$. If $\Delta m^2_{\text{eff}} < 0$, the hierarchy is defined to be inverted. Table 3 shows the oscillation parameters used in this section. For all the results presented in this section, we take $N_E = 20$ (in the range $E_\mu = [1,11]$ GeV) and $N_{\cos\theta} = 80$ (in the range $\cos\theta_\mu = [-1,1]$) in Eqn. 8.

Parameter	True Value	Marginalization Range
$\sin^2 2\theta_{12}$	0.86	
$\sin^2\theta_{23}$	0.4,0.5,0.6	$\sin^2\theta_{23}(\text{true}) \pm 0.1$
$\sin^2 2\theta_{13}$	0.08,0.10,0.12	$\sin^2 2\theta_{13}(\text{true}) \pm 0.03$
Δm^2_{21} (eV^2)	7.5×10^{-5}	
Δm^2_{eff} (eV^2)	2.4×10^{-3}	$[2.1 - 2.6] \times 10^{-3}$
δ_{CP}	$0°$	$[0 - 360]$ °

Table 3: True values of oscillation parameters used for the mass hierarchy analysis

6.1 Sensitivity for fixed oscillation parameters

Fig. 10 shows the mass hierarchy sensitivity for $\sin^2\theta_{23} = 0.5$ for three different values of $\sin^2 2\theta_{23}$. We see that for 10 years of ICAL operation, the wrong hierarchy can be ruled out at a significance of 2.7σ (2.7σ), for $\sin^2 2\theta_{13} = 0.1$, if the true hierarchy is normal (inverted). We find that χ^2_{ino} increases linearly with increasing exposure, as the hierarchy measurement is dominated by statistics. We notice that a larger θ_{13} value enhances the sensitivity, as expected. The matter effects are enhanced for large θ_{13} values and give rise to a larger difference in the μ^- and μ^+ event rates. The same effect is observed for the true value of the parameter θ_{23}. Fig. 11 shows χ^2_{ino} for $\sin^2 2\theta_{23} = 0.4$ and 0.6. With 10 years of ICAL exposure, 3.8σ hierarchy determination may be made if $\sin^2\theta_{13} = 0.12$ and $\sin^2\theta_{23} = 0.6$.
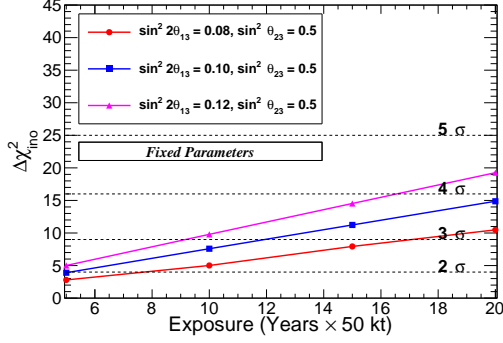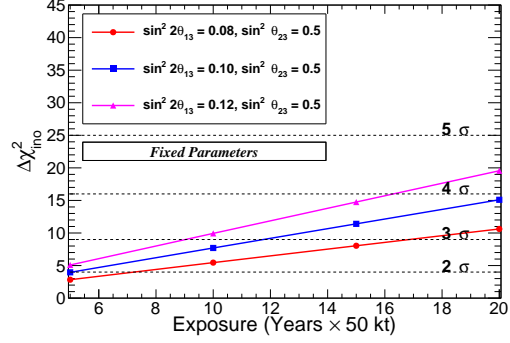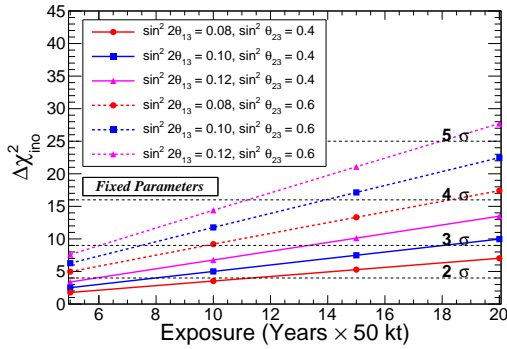
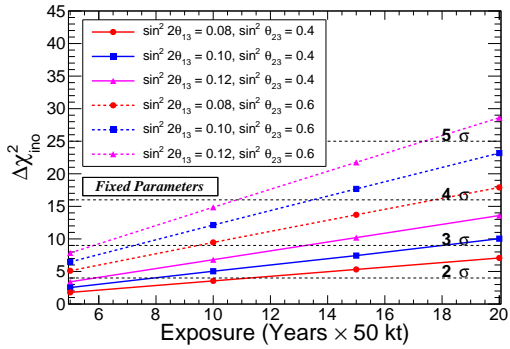(a) True Hierarchy : Normal
(b) True Hierarchy : Inverted

Figure 10: Mass hierarchy sensitivity for the fixed oscillation parameters, and $\sin^2 \theta_{23} = 0.5$

(a) True Hierarchy : Normal
(b) True Hierarchy : Inverted

Figure 11: Mass hierarchy sensitivity for the fixed oscillation parameters, and $\sin^2 \theta_{23} = 0.4, 0.6$
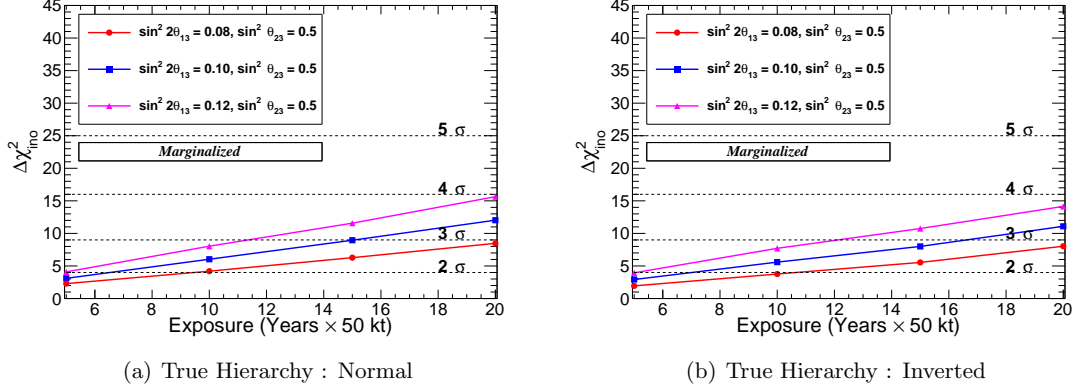
14

(a) True Hierarchy : Normal

(b) True Hierarchy : Inverted

Figure 12: Marginalized mass hierarchy sensitivity for $\sin^2\theta_{23} = 0.5$

(a) True Hierarchy : Normal

(b) True Hierarchy : Inverted
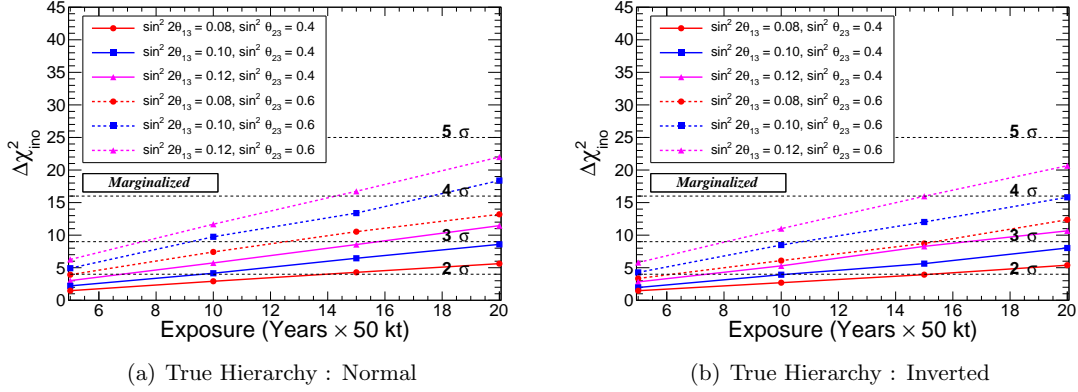
Figure 13: Marginalized mass hierarchy sensitivity for $\sin^2\theta_{23} =$ 0.4 and 0.6

6.2 Sensitivity after marginalization over the oscillation parameters

In the previous subsection, we assumed that the neutrino oscillation parameters are known to an infinite precision. However, this is not the case. In order to get a realistic estimate of the hierarchy sensitivity, we must allow for the uncertainty in the oscillation parameters while fitting the data. The marginalized $\Delta\chi^2_{\text{ino}}$ is found by allowing $\sin^2\theta_{23}$, $\sin^2 2\theta_{13}$ and Δm^2_{eff} to vary in the ranges indicated in Table 3. The solar oscillation parameters ($\sin^2 2\theta_{12}$, Δm^2_{21}) are kept fixed at values mentioned in Table 3. We also keep δ_{CP} fixed at $0°$. Fig. 12 shows the marginalized sensitivity for $\sin^2\theta_{23} = 0.5$. We observe that for 10 years of ICAL exposure and for $\sin^2 2\theta_{13} = 0.1$, the statistical significance for the hierarchy discovery drops to 2.4σ from 2.7σ(for fixed parameters) after marginalization

The marginalized $\Delta\chi^2_{\text{ino}}$ for different $\sin^2\theta_{23}$ is shown in Fig. 13. If $\sin^2\theta_{13} = 0.12$ and $\sin^2\theta_{23} = 0.6$, ICAL can determine the hierarchy with a 3σ significance for 10 year of exposure. The effect of marginalization is seen more for the normal hierarchy.

6.3 Sensitivity with Priors on Oscillation Parameters

By the time the ICAL detector starts taking data, values of the oscillation parameters $\sin^2\theta_{23}$, $\sin^2 2\theta_{13}$ and Δm^2_{eff} will further be constrained by other accelerator and reactor neutrino ex-

periments, such as T2K, NOνA, Daya Bay, RENO and Double Chooz. To reflect this, we add priors to χ^2_{ino} defined in Eqn. 11 :

$$\chi^2_{\text{ino}} = \chi^2_{\text{ino}} + \left(\frac{\sin^2 2\theta_{23}(\text{true}) - \sin^2 2\theta_{23}}{\sigma_{\sin^2 2\theta_{23}}}\right)^2 + \left(\frac{|\Delta m^2_{\text{eff}}|(\text{true}) - |\Delta m^2_{\text{eff}}|}{\sigma_{\Delta m^2_{\text{eff}}}}\right)^2$$
$$+ \left(\frac{\sin^2 2\theta_{13}(\text{true}) - \sin^2 2\theta_{13}}{\sigma_{\sin^2 2\theta_{13}}}\right)^2 . \tag{16}$$

We have taken $\sigma_{\sin^2 2\theta_{23}} = 0.02\sin^2 2\theta_{23}$, $\sigma_{\Delta m^2_{\text{eff}}} = 0.05\Delta m^2_{\text{eff}}$ and $\sigma_{\sin^2 2\theta_{23}} = 0.01$. Fig. 14 shows the comparison of χ^2_{ino} for fixed parameters, marginalized without priors and marginalized with priors. We see that with the addition of priors, the marginalized χ^2_{ino} is restored to the fixed parameter value.
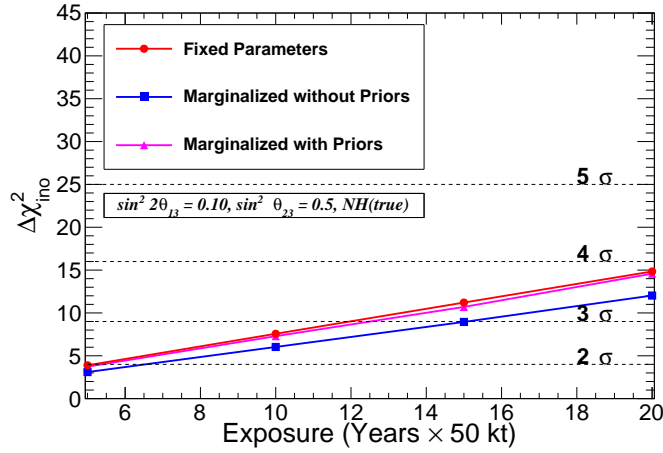
Figure 14: Marginalized hierarchy sensitivity with priors

6.4 Sensitivity as a function of δ_{CP}

In the analysis so far, δ_{CP} was assumed to be fixed to $0°$. In Fig. 15, we show the effect on $\Delta\chi^2_{\text{ino}}$ as a function of δ_{CP} (true). It can be seen that the fixed parameter $\Delta\chi^2_{\text{ino}}$ is independent of true δ_{CP} value (pink line). Further, a marginalization over δ_{CP} only, produces no change in the hierarchy sensitivity (blue line). A full marginalization over $\sin^2\theta_{23}$, $\sin^2 2\theta_{13}$, Δm^2_{eff} and δ_{CP} also gives the hierarchy sensitivity independent of true δ_{CP} value (red line). Therefore, it is not necessary to marginalize χ^2_{ino} over δ_{CP} and the mass hierarchy sensitivity at ICAL is independent of δ_{CP} value.

7 Summary

The ICAL detector at INO is an upcoming experiment in India. It consists of a 50 kt magnetized iron calorimeter with 150 alternate layers of iron plates as target mass for neutrino interactions and the RPCs as active detector elements. The detector is magnetized with a field of 1.3–1.5 T, that will enable it to identify the charge of particles and to separate neutrinos and anti-neutrinos.
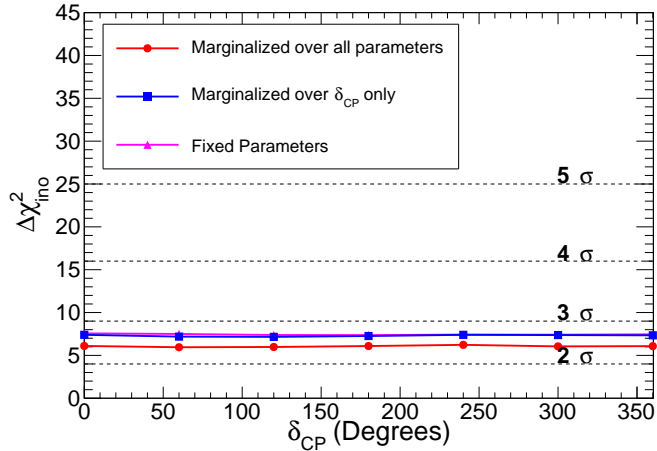
Figure 15: Effect of changing δ_{CP} on the sensitivity

The detector is primarily tuned to measure muon energy, direction and charge with high efficiency and good accuracy. We have studied the muon reconstruction in the ICAL detector in terms of (i) energy resolutions (ii) direction resolutions (iii) reconstruction efficiency, and (iv) charge identification efficiency in the energy range 0.5–25 GeV and for all directions. We find that all of the above quantities are strongly dependent on the incident energy and direction. The energy resolutions for muons is found to be 10–25 %, while the θ resolutions are about $1°$–$2°$. The efficiency of reconstruction varies between 10–90 %, improving with energy. The charge identification efficiencies are found to be between 95–100 %.

For the oscillation analysis, we have developed a ROOT-based package. We use the event generator NUANCE to produce the neutrino interactions inside the detector using un-oscillated fluxes. The oscillation effects are included using a Re-Weighting algorithm. The ICAL response to muons is folded in with the true muon event distribution to obtain the measured $(E, \cos\theta)$ distribution of muons. The χ^2 analysis is performed using this measured muon distribution. We have included 5 systematic errors in this analysis.

From our precision measurement analysis, we find that with 10 years of ICAL operation, we can determine $\sin^2\theta_{23}$ and $|\Delta m_{32}^2|$ to a precision of 17 % and 5.1 %, respectively. We also explore the possibility of determining the deviation of θ_{23} from maximal mixing and its octant. We find that both these tasks will be possible with ICAL, if the true value of θ_{23} is close to its current 3σ bound and is in the first octant. Otherwise they appear to be difficult for the ICAL to determine.

We report from the mass hierarchy analysis that the ICAL detector can determine the hierarchy to a significance of $(1.4$–$3.3)\sigma$ in 10 years run, depending on the value of the oscillation parameters θ_{23} and θ_{13}. The capability of muon charge identification to distinguish ν_μ and $\bar{\nu}_\mu$ to take advantage the enhanced matter effects is very important in this measurement. Including information on oscillation parameters obtained from other neutrino experiments will improve the statistical significance to $(2.2 - 3.8)\sigma$ in 10 years run. The hierarchy measurement at ICAL is independent of δ_{CP} value.

References

[1] B. Pontecorvo, Sov. Phys. JETP **26**, 984 (1968) [Zh. Eksp. Teor. Fiz. **53**, 1717 (1967)].

[2] Z. Maki, M. Nakagawa and S. Sakata, Prog. Theor. Phys. **28**, 870 (1962).

[3] L. Wolfenstein, Phys. Rev. D **17**, 2369 (1978).

[4] S. P. Mikheev and A. Y. .Smirnov, Sov. J. Nucl. Phys. **42**, 913 (1985) [Yad. Fiz. **42**, 1441 (1985)].

[5] D. N. Spergel *et al.* [WMAP Collaboration], Astrophys. J. Suppl. **148**, 175 (2003) [astro-ph/0302209].

[6] S. Hannestad, Prog. Part. Nucl. Phys. **65**, 185 (2010) [arXiv:1007.0658 [hep-ph]].

[7] J. Lesgourgues and S. Pastor, Adv. High Energy Phys. **2012**, 608515 (2012) [arXiv:1212.6154 [hep-ph]].

[8] H. V. Klapdor-Kleingrothaus, A. Dietz, L. Baudis, G. Heusser, I. V. Krivosheina, S. Kolb, B. Majorovits and H. Pas *et al.*, Eur. Phys. J. A **12**, 147 (2001) [hep-ph/0103062].

[9] N. Ackerman *et al.* [EXO-200 Collaboration], Phys. Rev. Lett. **107**, 212501 (2011) [arXiv:1108.4193 [nucl-ex]].

[10] C. Kraus, B. Bornschein, L. Bornschein, J. Bonn, B. Flatt, A. Kovalik, B. Ostrick and E. W. Otten *et al.*, Eur. Phys. J. C **40**, 447 (2005) [hep-ex/0412056].

[11] J. Wolf [KATRIN Collaboration], Nucl. Instrum. Meth. A **623**, 442 (2010) [arXiv:0810.3281 [physics.ins-det]].

[12] G. L. Fogli, E. Lisi, A. Marrone, D. Montanino, A. Palazzo and A. M. Rotunno, Phys. Rev. D **86**, 013012 (2012) [arXiv:1205.5254 [hep-ph]].

[13] M. S. Athar *et al.* [INO Collaboration], INO-2006-01.

[14] D. Casper, Nucl. Phys. Proc. Suppl. **112**, 161 (2002) [hep-ph/0208030].

[15] M. Honda, T. Kajita, K. Kasahara and S. Midorikawa, Phys. Rev. D **83**, 123001 (2011) [arXiv:1102.2688 [astro-ph.HE]].

[16] M. C. Gonzalez-Garcia and M. Maltoni, Phys. Rev. D **70**, 033010 (2004) [hep-ph/0404085].

[17] T. Dealtry, T2K Collaboration, "Muon neutrino disappearance at T2K", http://indico.cern.ch/contributionDisplay.py?contribId=36&sessionId=12&confId=214998.

[18] S. Choubey and P. Roy, Phys. Rev. D **73**, 013006 (2006) [hep-ph/0509197].

[19] V. Barger, R. Gandhi, P. Ghoshal, S. Goswami, D. Marfatia, S. Prakash, S. K. Raut and S U. Sankar, Phys. Rev. Lett. **109**, 091801 (2012) [arXiv:1203.6012 [hep-ph]].

[20] D. Indumathi, M. V. N. Murthy, G. Rajasekaran and N. Sinha, Phys. Rev. D **74**, 053004 (2006) [hep-ph/0603264].

[21] R. Gandhi, P. Ghoshal, S. Goswami, P. Mehta and S. U. Sankar, Phys. Rev. D **73**, 053001 (2006) [hep-ph/0411252].

[22] H. Nunokawa, S. J. Parke and R. Zukanovich Funchal, Phys. Rev. D **72**, 013009 (2005) [hep-ph/0503283].

List of Publications

[1] T. Thakore, A. Ghosh, S. Choubey and A. Dighe, JHEP **1305**, 058 (2013) [arXiv:1303.2534 [hep-ph]].

[2] A. Ghosh, T. Thakore and S. Choubey, JHEP **1304**, 009 (2013) [arXiv:1212.1305 [hep-ph]].

[3] A. Chatterjee, Meghna K, K. Rawat, T. Thakore, et al., JINST **9**, P07001 (2014) [arXiv:1405.7243 [physics.ins-det]].

List of Publications

Publications related to this Thesis

- The Reach of INO for Atmospheric Neutrino Oscillation Parameters
  T. Thakore, A. Ghosh, S. Choubey and A. Dighe
  JHEP **1305**, 058 (2013) [arXiv:1303.2534 [hep-ph]].

- Determining the Neutrino Mass Hierarchy with INO, T2K, NOvA and Reactor
  Experiments
  A. Ghosh, T. Thakore and S. Choubey
  JHEP **1304**, 009 (2013) [arXiv:1212.1305 [hep-ph]].

- A Simulations Study of the Response of ICAL Detector to Muons
  Animesh Chatterjee, Meghna K, Kanishka Rawat, Tarak Thakore, et al.,
  JINST **9**, P07001 (2014) [arXiv:1405.7243 [physics.ins-det]].

Other Publications (under Preparation)

- Enhancing sensitivity to neutrino parameters at INO combining muon and
  hadron information
  Moon Moon Devi, Tarak Thakore, Sanjib Agarwalla, Amol Dighe
  arXiv:1406.3689 [hep-ph]. (Accepted in JHEP)

- ICAL Physics Analysis with Full GEANT4 Simulations
  Tarak Thakore, Kolahal Bhattacharya, et al.

- Combined Future Sensitivity to the Neutrino Oscillatino Parameters using the
  ICAL, T2K and NOνA data
  Tarak Thakore, Sanjib Agarwalla, et al.

- Sensitvity to NSI parameters at ICAL
  Tarak Thakore, Sanjib Agarwalla, Amina Khatun, Sabya Sachi Chatterjee .

Contents

List of Figures

List of Tables

Chapter 1

Introduction

The Standard Model of particle physics has been a phenomenal success in our attempts to understand how nature works at microscopic scales. It consists of three generations of quarks and leptons which come in doublets. These particles interact with each other through the gauge bosons. The last missing piece of the Standard Model, the Higgs Boson, was discovered at the CMS and ATLAS experiments at the Large Hadron Collider in 2012 [1, 2].

In the Standard Model, the neutrinos are massless. However, various experiments in the last decade have firmly established the neutrino oscillation phenomenon. Neutrino oscillation requires at least two of them to be massive particles. Various extensions of the Standard Model have been proposed to accommodate massive neutrinos [3]. The simplest extension is to allow for the right handed neutrinos. Another favoured model involve the see-saw mechanism [4, 5].

1.1   Neutrino Oscillations in Vacuum

The theory of neutrino oscillation was first proposed by Pontecorvo in 1950s. In 1962, Maki, Nakagawa and Sakata proposed the model of neutrino oscillation for the active flavors of neutrinos [6]. It was later developed in the standard theory by Eliezer, Swift Bilenky and Pontecorvo [7]. Here, we present a brief derivation of neutrino oscillation

probabilities in vacuum [8, 9].

Neutrinos interact with the SM particles through the exchange of $W^{\pm}$ or Z bosons in charged current (CC) or neutral current (NC) processes. The states which participate in these interactions are the flavor states. The flavor states ($|\nu_{\alpha}\rangle$) do not have definite mass, but they are superposition of the mass states ($|\nu_i\rangle$) with definite masses.

$$|\nu_{\alpha}\rangle = \sum_i U_{\alpha i}^* |\nu_i\rangle. \tag{1.1}$$

Here, U is the unitary mixing matrix. If the neutrino is created in the flavor state α at time t=0, then at a later time the state evolves as,

$$|\nu_{\alpha}(t)\rangle = \sum_{\beta} |\nu_{\beta}\rangle \langle \nu_{\beta}|e^{-iH_0 t}|\nu_{\alpha}\rangle, \tag{1.2}$$

where H_0 is the free particle Hamiltonian. The amplitude of flavor transition $\nu_{\alpha} \to \nu_{\beta}$ is,

$$A(\nu_{\alpha} \to \nu_{\beta}) = \langle \nu_{\beta}|\nu_{\alpha}(t)\rangle. \tag{1.3}$$

The oscillation probability can be calculated as,

$$\begin{aligned} P(\nu_{\alpha} \to \nu_{\beta}) &= |\langle \nu_{\beta}|e^{-iH_0 t}|\nu_{\alpha}\rangle|^2 \\ &= |\sum_i \langle \nu_{\beta}|\nu_i\rangle \, e^{-iE_i t} \langle \nu_i|\nu_{\alpha}\rangle|^2 \\ &= |\sum_i U_{\beta i} e^{-iE_i t} U_{\alpha i}^*|^2 \end{aligned} \tag{1.4}$$

For ultra-relativistic neutrinos, we can write,

$$\begin{aligned} E_i &= \sqrt{p^2 + m_i^2} \\ &\approx E + \frac{m_i^2}{2E}, \end{aligned} \tag{1.5}$$

where E = p is the energy of the neutrino, in the limit $m_i \to 0$. Also, using the

approximation, t = L, where L is the distance between the source and the detector, we obtain,

$$P(\nu_\alpha \to \nu_\beta) = |\sum_i U_{\beta i} e^{-i\frac{m_i^2 L}{2E}} U_{\alpha i}^*|^2. \tag{1.6}$$

It follows that,

$$P(\nu_\alpha \to \nu_\beta) = \sum_i |U_{\beta i}|^2 |U_{\alpha i}|^2 + 2Re \sum_{i>k} U_{\beta i} U_{\alpha i}^* U_{\beta k}^* U_{\alpha k} e^{-2i\Delta_{ki}}, \tag{1.7}$$

where $\Delta_{ki} = \frac{\Delta m_{ki}^2 L}{4E}$, and $\Delta m_{ki}^2 = m_k^2 - m_i^2$.

Using the unitarity of the matrix U ($\sum_i U_{\beta i} U_{\alpha i}^* = \delta_{\alpha\beta}$) in Eqn. 1.7, we obtain the probability of the transition $\nu_\alpha \to \nu_\beta$,

$$\begin{aligned} P(\nu_\alpha \to \nu_\beta) = \delta_{\alpha\beta} &- 4Re \sum_{i>k} U_{\beta i} U_{\alpha i}^* U_{\beta k}^* U_{\alpha k} \sin^2 \frac{\Delta m_{ki}^2 L}{4E} \\ &+ 2Im \sum_{i>k} U_{\beta i} U_{\alpha i}^* U_{\beta k}^* U_{\alpha k} \sin \frac{\Delta m_{ki}^2 L}{2E} \ . \end{aligned} \tag{1.8}$$

Assuming CPT invariance, the oscillation probability expression for the anti-neutrinos can be found by changing $U_{\alpha i}$ to $U_{\alpha i}^*$. We get,

$$\begin{aligned} P(\overline{\nu}_\alpha \to \overline{\nu}_\beta) = \delta_{\alpha\beta} &- 4Re \sum_{i>k} U_{\beta i} U_{\alpha i}^* U_{\beta k}^* U_{\alpha k} \sin^2 \frac{\Delta m_{ki}^2 L}{4E} \\ &- 2Im \sum_{i>k} U_{\beta i} U_{\alpha i}^* U_{\beta k}^* U_{\alpha k} \sin \frac{\Delta m_{ki}^2 L}{2E}. \end{aligned} \tag{1.9}$$

Including the factors of $\hbar$ and c in Eqn. 1.8, we get,

$$\frac{\Delta m_{ki}^2 L}{4E} \approx 1.27 \Delta m_{ki}^2 (eV^2) \frac{L(km)}{E(GeV)} \ . \tag{1.10}$$

In the case of two flavor neutrino oscillation, the mixing matrix U becomes,

$$U = \begin{pmatrix} \cos\theta & \sin\theta \\ -\sin\theta & \cos\theta \end{pmatrix}. \qquad (1.11)$$

We obtain a simple expression for the transition, $\nu_\alpha \to \nu_\beta$.

$$P(\nu_\alpha \to \nu_\beta) = \sin^2 2\theta \sin^2\left(1.27\Delta m^2 \frac{L}{E}\right) \qquad (1.12)$$

From Eqn. 1.9 and 1.12 we note the following points :

1. Neutrino oscillations require non-zero, as well as non-degenerate neutrino masses.

2. Observation of neutrino oscillations implies that the mixing matrix is not unity, e.g. $U \neq I$.

3. Observing neutrino oscillation can give information on the neutrino mass squared difference, Δm_{ij}^2, but not on the absolute neutrino mass, m_i.

4. An experiment operating at energy E(GeV) and of baseline L(km) will be sensitive to the neutrino mass squared difference of,

$$\Delta m_{ij}^2(\text{eV}^2) \geq \frac{E(\text{GeV})}{L(\text{km})} . \qquad (1.13)$$

If the matrix U is real, then the last term in Eqn. 1.8 and 1.9 vanish and there is no CP violation. In the case where matrix U is complex, the CP asymmetry is,

$$P(\nu_\alpha \to \nu_\beta) - P(\overline{\nu}_\alpha - \overline{\nu}_\beta) = 4\,Im \sum_{i>k} U_{\beta i} U_{\alpha i}^* U_{\beta k}^* U_{\alpha k} \sin\frac{\Delta m_{ki}^2 L}{2E} . \qquad (1.14)$$

1.2 Three Flavor Neutrino Oscillations

The expressions for neutrino oscillation probability derived in the previous section hold for any number of neutrinos. However, the current experimental evidences, notably, the decay of Z^0 boson and the cosmological constraints strongly suggest

that there are three neutrino flavors, ν_e, ν_μ and ν_τ. They are related to three mass states ν_1, ν_2 and ν_3 with masses m_1, m_2 and m_3 through the unitary matrix U. In the three neutrino framework, matrix U is called as Pontecorvo-Maki-Nakagawa-Sakata matrix, U_{PMNS}, defined as follows.

$$U_{\mathrm{PMNS}} = \underbrace{\begin{pmatrix} 1 & 0 & 0 \\ 0 & c_{23} & s_{23} \\ 0 & -s_{23} & c_{23} \end{pmatrix}}_{\text{Atmospheric } (\theta_{23} \sim 45^\circ)} \underbrace{\begin{pmatrix} c_{13} & 0 & s_{13}e^{-i\delta_{\mathrm{CP}}} \\ 0 & 1 & 0 \\ -s_{13}e^{i\delta_{\mathrm{CP}}} & 0 & c_{13} \end{pmatrix}}_{\text{Reactor } (\theta_{13} \sim 9^\circ)} \underbrace{\begin{pmatrix} c_{12} & s_{12} & 0 \\ -s_{12} & c_{12} & 0 \\ 0 & 0 & 1 \end{pmatrix}}_{\text{Solar } (\theta_{12} \sim 33^\circ)} \begin{pmatrix} e^{\frac{i\alpha_1}{2}} & 0 & 0 \\ 0 & e^{\frac{i\alpha_2}{2}} & 0 \\ 0 & 0 & 1 \end{pmatrix}$$

$$(1.15)$$

where $s_{ij} = \cos\theta_{ij}$ and $s_{ij} = \sin\theta_{ij}$. Here, θ_{ij} refers to three mixing angles θ_{12}, θ_{13} and θ_{23}.

The most general three flavor oscillation probabilities expressions are complicated. The simplified expressions can be obtained in the One Mass Squared Dominant(OMSD) approximation, e.g., $\Delta m_{31}^2 (\sim \Delta m_{atm}^2 \sim 10^{-3}$ eV^2) $>> \Delta m_{21}^2 (\sim \Delta m_\odot^2 \sim 10^{-5}$ eV^2),

$$P_{e\mu} = \sin^2 2\theta_{13} \sin^2 \theta_{23} \sin^2 \left(1.27 \frac{\Delta m_{31}^2 L}{E} \right) \tag{1.16}$$

$$P_{\mu\tau} = \cos^4 \theta_{13} \sin^2 2\theta_{23} \sin^2 \left(1.27 \frac{\Delta m_{31}^2 L}{E} \right) \tag{1.17}$$

1.3 Neutrino Oscillation in Matter

We obtained neutrino oscillation probabilities while they propagate in vacuum in Section 1.1. Despite the low cross sections, when neutrinos propagate through matter, the probabilities can significantly be modified due to coherent forward current scattering with the electrons, protons and neutrons, present in the matter [10]. This phenomenon is know as the matter effect.

While all three flavors can interact with an electron in the neutral current process,
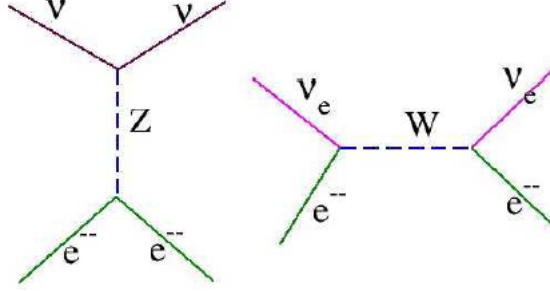
Figure 1.1: NC and CC neutrino interactions with electrons. While all neutrino flavors can undergo NC interactions, only the ν_e can interact through CC interaction with electrons.

only ν_e can interact through the charged current process.

$$\nu_x + (e, p, n) \rightarrow \nu_x + (e, p, n)(\text{NC})(\nu_x = \nu_e, \nu_\mu, \nu_\tau) \tag{1.18}$$

$$\nu_e + e^- \rightarrow \nu_e + e^- (\text{CC} + \text{NC}) \tag{1.19}$$

The additional CC interaction in the process $\nu_e + e^- \rightarrow \nu_e + e^-$ gives ν_e an extra potential V_{CC}. All neutrino flavors experience the potential V_{NC} due to NC interactions. The effective potentials are,

$$V_{\text{CC}} = \sqrt{2}G_F n_e, \tag{1.20}$$

$$V_{\text{NC}} = -\frac{\sqrt{2}}{2}G_F n_n, \tag{1.21}$$

where n_e and n_n are the number density of electrons and neutrinos, respectively. G_F is the Fermi coupling constant. For an electrically neutral material, $n_e = n_p = n_n$. Then, the matter Hamiltonian is,

$$H_m = H_0 + V_f, \tag{1.22}$$

where,

$$V_f = \begin{pmatrix} V_{\text{CC}} + V_{\text{NC}} & 0 \\ 0 & V_{\text{NC}} \end{pmatrix} \tag{1.23}$$

For pedagogical reasons, let us illustrate the matter effects for two flavor oscilla-

tions, $\nu_e \leftrightarrow \nu_\mu$. The Hamiltonian in the mass basis can be written as,

$$H_0 = \frac{1}{2E} \begin{pmatrix} m_1^2 & 0 \\ 0 & m_2^2 \end{pmatrix}. \tag{1.24}$$

In the flavor basis, it becomes,

$$U H_0 U^\dagger, \tag{1.25}$$

where, U is defined in Eqn. 1.11. Simplifying Eqn. 1.25 and dropping the terms proportional to the unit matrix **I**,

$$H_0 = \frac{\Delta m^2}{2E} \begin{pmatrix} -\cos 2\theta & \sin 2\theta \\ \sin 2\theta & \cos 2\theta \end{pmatrix}. \tag{1.26}$$

The matter Hamiltonian in Eqn. 1.22 after dropping the terms proportional to **I** becomes,

$$H_m = \frac{\Delta m^2}{4E} \begin{pmatrix} -\cos 2\theta + \xi & \sin 2\theta \\ \sin 2\theta & \cos 2\theta - \xi \end{pmatrix}, \tag{1.27}$$

where,

$$\xi = \frac{2V_{\text{CC}}E}{\Delta m^2} = \frac{2\sqrt{2}G_F n_e}{\Delta m^2}. \tag{1.28}$$

After diagonalizing H_m in Eqn. 1.27, we obtain,

$$H_m = \frac{\Delta m_m^2}{4E} \begin{pmatrix} -\cos 2\theta_m & \sin 2\theta_m \\ \sin 2\theta_m & \cos 2\theta_m \end{pmatrix}. \tag{1.29}$$

The effective mass squared difference and the mixing angles become :

$$\tan 2\theta_m = \frac{\Delta m^2 \sin 2\theta}{\Delta m^2 \cos 2\theta - A}, \tag{1.30}$$

$$\Delta m_m^2 = \left[\left(\Delta m^2 \cos 2\theta - A \right)^2 + \left(\Delta m^2 \sin 2\theta \right)^2 \right]^{1/2}, \tag{1.31}$$

where $A = \pm 2\sqrt{2}G_F n_e E$ (+ neutrino, - anti-neutrino), and n_e is the electron number density.

The neutrino oscillation probability is now given by the same expression as in vacuum (Eqn. 1.12), but with the mixing angle and the mass squared difference given in Eqn. 1.30 and 1.31. We note the following points about the matter effects.

1. For $n_e \to 0$, Eqn. 1.30 and 1.31 reduce to the vacuum mixing angle and the mass squared difference.

2. For very high density, $n_e \to \infty$ (or very high energy, $E \to \infty$), $\theta_m \to \frac{\pi}{2}$. Thus, even though the vacuum mixing angle is small, in dense matter, the mixing angle becomes maximal.

3. If $A = \Delta m^2 \cos 2\theta$ then the denominator of Eqn. 1.30 goes to zero giving rise to a resonance phenomena, known as the MSW (Mikheyev–Smirnov–Wolfenstein) Resonance [11, 12, 13]. If $\Delta m^2 > 0$ then resonance occurs for the neutrinos and if $\Delta m^2 < 0$ then the resonance occurs for the anti-neutrinos. Thus, the MSW effect results in different oscillation probabilities for the neutrinos and anti-neutrinos.

4. In general, for varying density matter, both the two flavor and three flavor neutrino propagation has to be solved numerically.

1.4   Experimental Results

Since the discovery of a deficiency in the solar neutrino flux from the predicted flux, several experiments have confirmed neutrino oscillation with large statistical significance. Observation of neutrinos require large detectors due to small cross sections, via CC and NC interactions inside the detector volume. Most of the neutrino detectors are setup in the underground facilities, in order to provide natural rock shield from the cosmic particle background. The sources can be natural such as solar and atmospheric neutrinos. Artificial neutrino sources like nuclear reactors and particle accelerators are also used. A variety of detector technologies have been used, such as water or ice Cherenkov, liquid scintillates, iron calorimeters, nuclear emulsions. Depending on which oscillation parameter has to be studied, a disappearance or an

appearance experiment may be designed with one of these sources and detector technology. Here, we present only a brief review of the important neutrino experiments. For an extensive compilation of neutrino experiments can be found in [14].

1.4.1 Solar Oscillation Parameters $(\theta_{12}, \Delta m_{21}^2)$

The 'Standard Solar Model (SSM) describes the energy production in the sun using known physics processes [15, 16]. The sun produces energy primarily through the net nuclear fusion reaction,

$$4p \rightarrow {}^4He + 2\nu_e(\text{Q} = 26.7 \text{ MeV}) + 2e^+ \ . \tag{1.32}$$

This process can happen via the pp chain reactions or the CNO cycle. The Sun generates 98.1% of the total energy through the set of pp chain reactions. The energy produced in this process is shared by all final state particles. The average neutrino energy E_ν in this process is 0.3 MeV, with a flux of 6×10^{10} cm^{-2}sec^{-1} at the Earth. The major components of the solar neutrino spectrum are shown in Fig. 1.2.

The solar neutrino flux was first measured by the Homestake[17, 18] experiment through the reaction, $\nu_e + {}^{37}Cl \rightarrow e^- + {}^{37}Ar$. By measuring the half life of radioactive Ar, the number of neutrino interactions were found. From this measurement, the solar neutrino flux was measured to be 2.56±0.16±0.16 Solar Neutrino Unit (SNU) [19], against the prediction of $8.46^{+0.87}_{-0.88}$ SNU [20]. This deficit in the measured flux of solar ν_e came to be know as the "solar neutrino problem". The observed deficit was later confirmed by the Gallium experiments, SAGE[21] and GALLEX[22, 23]. Both the Chlorine and Gallium experiments observed the solar neutrino deficit at low energies produced in the pp chain and were radiochemical experiments. Later, real time experiments, Kamiokande[24] and Super-Kamiokande[25, 26, 27] also reported the deficit in ^{8}B neutrinos from the SSM prediction.

The solar neutrino problem was finally resolved by the SNO experiment by observing ^{8}B neutrinos. The SNO experiment[28] was designed to measure both CC interaction of ν_e in the process $\nu_e + d \rightarrow e^- + p + p$, and the NC interaction of all flavors in the process $\nu_x + d \rightarrow \nu_x + p + n$. The number of observed CC interactions were
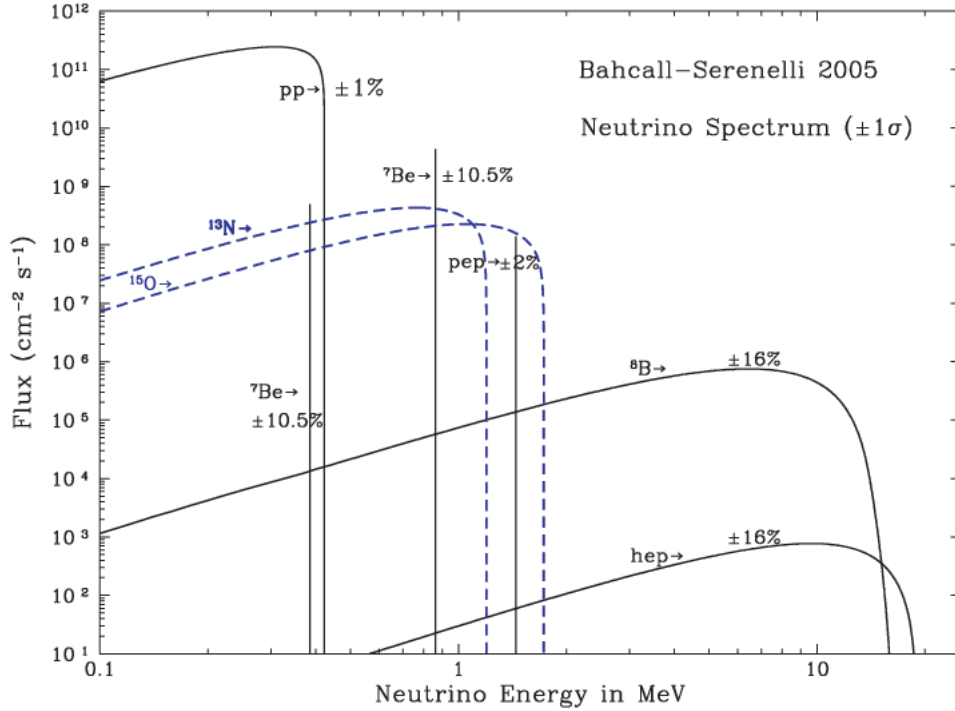
Figure 1.2: The spectrum of solar neutrinos predicted by the standard solar model [15]

about 1/3 of the expectation, whereas the observed NC interactions were consistent with the prediction [29, 30]. These observations are consistent with the oscillation hypothesis [30]. Since the solar neutrinos travel through the dense core of the sun with the density falling in the radial direction, they undergo the MSW resonance on their way out to the surface. The SNO data favor the Large Mixing Angle (LMA) solution with the best fit point [30],

$$\tan^2 \theta_{12} = 0.427^{+0.033}_{-0.029},$$
$$\Delta m^2_{21} = 5.62^{+1.92}_{-1.36} \times 10^{-5} \text{ eV}^2. \tag{1.33}$$

The solar neutrino oscillation were confirmed by the reactor neutrino experiment KamLAND[31]. KamLAND measured the oscillations in the $\bar{\nu}_e$ emitted from a complex of nuclear reactors. The average energy of these neutrinos are E $\sim$ 3 MeV, and the distances from the reactors to the detector are between $100-700$ km. This energy and distance are compatible to measure $\Delta m^2 \sim 10^{-5}$ eV^2. Fig. 1.3 shows the ratio of $\bar{\nu}_e$ event spectrum observed by KamLAND to no oscillation prediction spectrum [32].
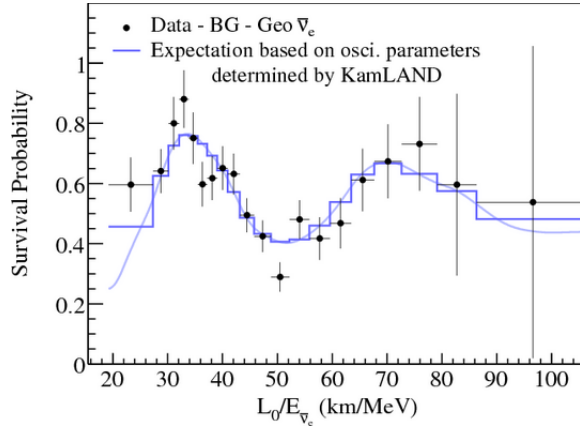
Figure 1.3: Ratio of $\overline{\nu}_e$ observed by KamLAND to no oscillation prediction[32]
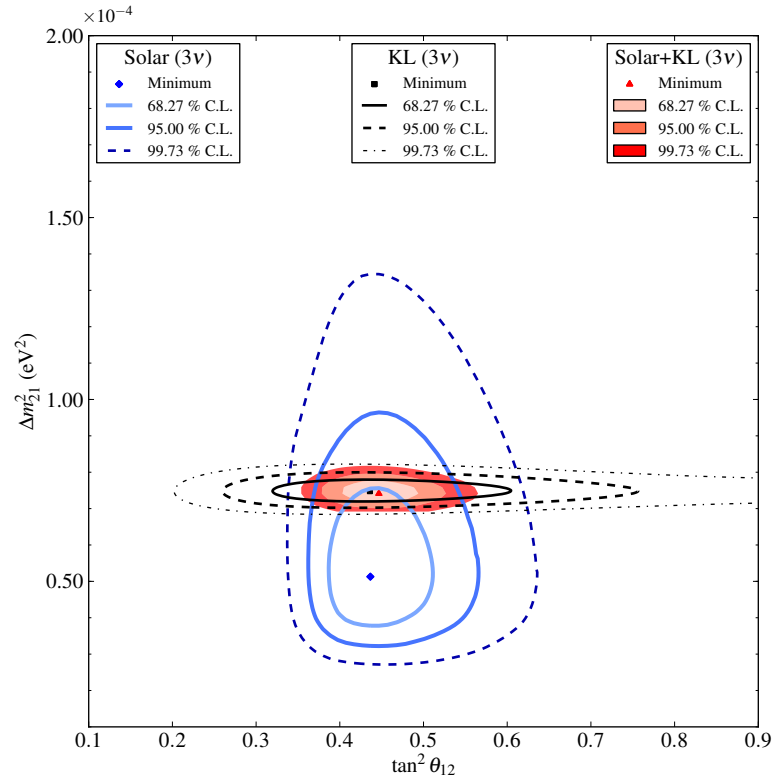
Figure 1.4: Allowed parameter space from the combined analysis of solar and KamLAND data[32]

The KamLAND best fit point is consistent with the LMA solution from SNO.

Fig. 1.4 shows the allowed parameter space from a combined analysis of solar and KamLAND data. The best fit point in this analysis is [32],

$$
\begin{aligned}
\tan^2 \theta_{12} &= 0.427^{+0.027}_{-0.024}, \\
\Delta m^2_{21} &= 7.46^{+0.20}_{-0.19} \times 10^{-5} \text{ eV}^2.
\end{aligned}
\tag{1.34}
$$

1.4.2 Atmospheric Oscillation Parameters ($\theta_{23}, \Delta m^2_{31}$)

The atmospheric neutrinos are produced in the interaction of the cosmic rays with the atmospheric nuclei (Section 4.1). Both ν_e, ν_μ as well as $\bar{\nu}_e$, $\bar{\nu}_\mu$ are generated in these interactions. The flux of the atmospheric neutrinos peak around 1 GeV and they can have baselines of 15 km for the down-going neutrinos to 13,000 km for the up-going neutrinos. With this L/E combination, the atmospheric neutrino experiments can probe $\Delta m^2 \sim 10^{-4}$ eV^2.

The first hints of the atmospheric neutrino oscillations were found by IMB [34], Kamiokande [35] and Soudan-2 [36]. All these experiments observed a deficit in the flux of ν_μ compared with the no oscillation prediction. The most compelling evidence of the deficit in the observed ν_μ flux came from the Super-Kamiokande (SK) experiment [37]. It observed the first L/E dip in the characteristic muon neutrino survival probability [38].

Fig. 1.5 shows the zenith angle distribution for ν_e and ν_μ by the SK experiment [39]. The up-down asymmetry seen in the SK ν_μ zenith angle distribution is consistent with the oscillation hypothesis. The down-going neutrinos travel a small distance for the oscillations to develop. However, the up-going neutrinos can travel thousands of kilometers and can undergo significant oscillations. Such an asymmetry is not observed in the ν_e zenith angle distribution. This means that in the atmospheric section, the dominant oscillations are $\nu_\mu \leftrightarrow \nu_\tau$. The analysis of the SK data gives the best fit point [39],

$$
\begin{aligned}
\sin^2 \theta_{23} &= 0.5 \\
|\Delta m^2_{32}| &= 2.5 \times 10^{-3} \text{ eV}^2.
\end{aligned}
\tag{1.35}
$$
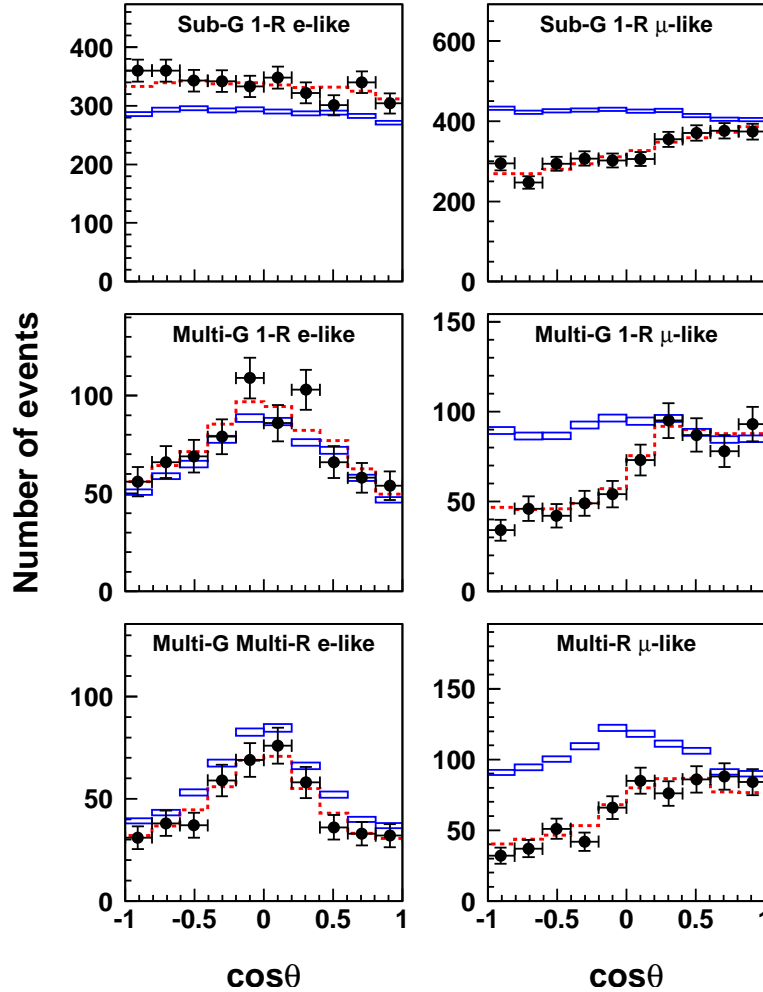
Figure 1.5: Super-Kamiokande zenith angle distributions for e-like and μ-like events [39]. The top, middle and lower panels show the distributions for Sub-GeV one ring, Sub-GeV multi ring and Multi-GeV multi ring respectively. The data are shown with the black dots. Continuous blue curves show the MC distribution without oscillations, and the dashed red curves show the best fit to the data.

The atmospheric neutrino oscillation parameters can also be probed using long baseline accelerator neutrino experiments, with $E_\nu \sim 1$ GeV and L ~ 100 km. The accelerator experiments produce neutrinos by colliding an energetic proton beam onto a fixed target, which produce pions. The direction of the charged pions is controlled through the magnetic horns and then passed on to the decay tunnel to produce a collimated $\nu_\mu(\bar{\nu}_\mu)$ beam. Typically, such experiments employ a near and a far detector setup, which allows them to reduce systematics and obtain a good

understanding of the un-oscillated neutrino flux. The experiments K2K, MINOS and T2K have employed this strategy to constrain the atmospheric oscillation parameters.
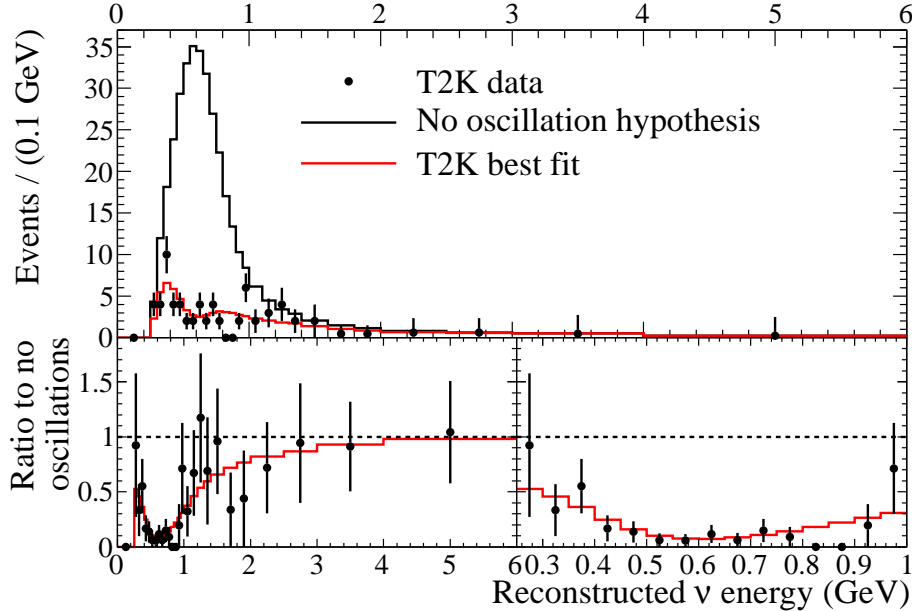
Figure 1.6: The top panel shows ν_μ spectrum observed by SK from the T2K beam. The bottom panel shows the ratio of observed spectrum to no oscillation prediction in two different energy ranges [45].

The first experiment to take this approach was K2K, with an average beam energy of 1.4 GeV and a baseline of 250 km. The K2K experiment confirmed the Super-Kamiokande atmospheric neutrino result [40] with 0.92×10^{20} protons on target (POT). The MINOS experiment [41, 42] uses the neutrino beam produced in the NuMI facility at Fermilab. The neutrinos are observed in the far detector located in the Soudan Mine, 735 km away from Fermilab. MINOS has taken data with both neutrino and anti-neutrino runs of NuMI. Because of its fine L/E resolution, MINOS has provided a tighter constraint on Δm^2_{32} than the SK atmospheric data [43]. More recently, the super-beam experiment T2K has provided the most accurate measurement of the atmospheric parameters so far. The T2K experiment [44] utilized an off-axis beam, which results in a narrow beam spectrum at the far detector, Super-Kamiokande. The neutrino beam in T2K is created at the J-PARC accelerator with a beam power of 750 kW. The T2K design beam power is 750 kW, but it has not achieved this power yet. So far, the maximum power achieved in the neutrino beam of T2K is about 250 kW. With an intense neutrino beam, the T2K is able to collect

large event statistics in a short time. Fig. 1.6 shows the event spectrum observed by SK from the T2K beam and the no oscillation prediction.

Fig. 1.7 shows the constraints on the atmospheric parameters from the SK, MINOS and T2K [45]. The best fit point with the T2K data of 3.01×10^{20} POT is,

$$\sin^2 \theta_{23} = 0.514 \tag{1.36}$$
$$|\Delta m_{32}^2| = 2.44 \times 10^{-3} \text{ eV}^2.$$

As T2K is still taking more data, the constraints on the atmospheric parameters will improve further.
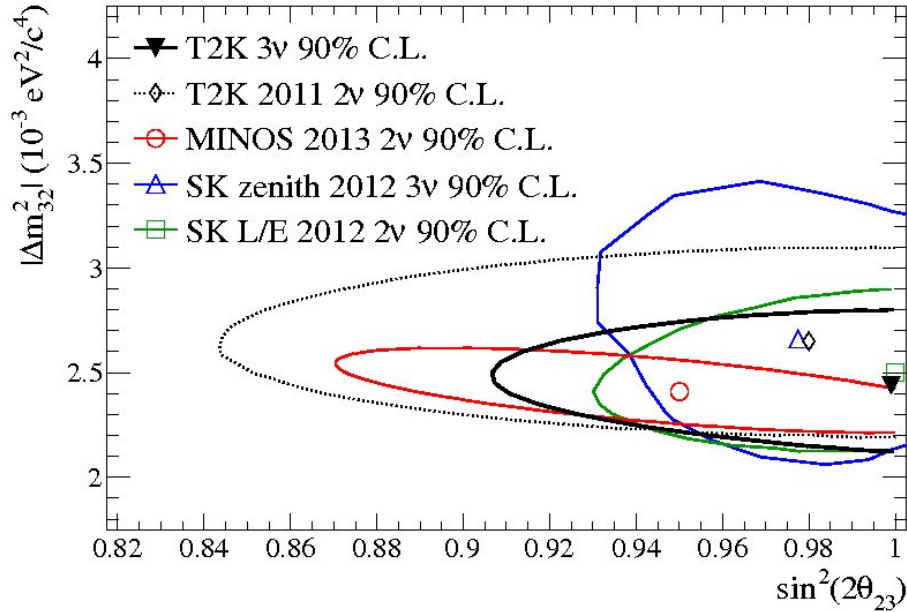
Figure 1.7: The 90% CL contours for the atmospheric parameters $(\sin^2 2\theta_{23}, |\Delta m_{32}^2|)$ for SK, MINOS and T2K [45].

1.4.3 Measurement of θ_{13}

Until the year 2012, the mixing angle θ_{13} was unknown and only the upper bound, $\sin^2 \theta_{13} \leq 0.16$ (at 90% C.L.) was known on this parameter from the reactor neutrino experiment CHOOZ[46].

The parameter θ_{13} can be measured in two ways.

1. **The appearance channel $\nu_\mu \to \nu_e$ in the accelerator neutrino experiments :**

   The first indication of a non-zero θ_{13} was given by T2K with the observation of 6 ν_e events in a ν_μ beam at 2.5σ [47]. The expectation for $\theta_{13} = 0$ was 1.5 ± 0.3 events. This result gave the best fit value of $\sin^2 2\theta_{13} = 0.11$ with $\delta_{\rm CP} = 0$. The MINOS collaboration also reported 62 ν_e events with the expectation of $49.6 \pm 7.0 \pm 2.7$ events for $\theta_{13} = 0$ [48]. This gives the bound $2\sin^2 \theta_{23} \sin^2 2\theta_{13} < 0.12$ for NH and $\delta_{\rm CP} = 0$.

   A more recent T2K appearance result excludes $\theta_{13} = 0$ at 7.3σ with the observation of 28 ν_e events [49]. The best fit value is, $\sin^2 2\theta_{13} = 0.14$ for the NH and $\delta_{\rm CP} = 0$.

2. **The disappearance channel $\overline{\nu}_e \to \overline{\nu}_e$ in the short baseline reactor neutrino experiments :**

Three reactor neutrino experiments confirmed the non-zero θ_{13} in a short time interval in the year 2012. The Daya Bay experiment reported $\sin^2 2\theta_{13} = 0.092 \pm 0.016 ({\rm stat}) \pm 0.005 ({\rm syst})$ in 2012, excluding $\theta_{13} = 0$ at 5.2σ [50]. Shortly, the RENO experiment also reported $\sin^2 2\theta_{13} = 0.113 \pm 0.013 ({\rm stat}) \pm 0.019 ({\rm syst})$ [51]. RENO excluded $\theta_{13} = 0$ at 4.9σ. The Double CHOOZ experiment measured $\sin^2 2\theta_{13} = 0.109 \pm 0.030 ({\rm stat}) \pm 0.025 ({\rm syst})$, and excluded $\theta_{13} = 0$ at 3.1σ [52]. An improved measurement at Daya Bay gives the best fit point at $\sin^2 2\theta_{13} = 0.089 \pm 0.009$ [53].

A non-zero and large value of θ_{13} has been the latest breakthrough in the area of neutrino oscillation. It has opened up the way to determine the neutrino mass hierarchy and the measurement of $\delta_{\rm CP}$.

1.5   Current Status and Unanswered Questions

As outlined in the previous section, a number of experiments have not only established the neutrino oscillations, but also have made precision measurement of the oscillation parameters. All three mixing angles, $\theta_{12}, \theta_{13}, \theta_{23}$ as well as the two mass squared

Parameter	Best Fit Value	3σ Ranges
$\sin^2\theta_{12}$	0.307	0.259-0.359
$\sin^2\theta_{23}$	0.386	0.331-0.637 (NH)
	0.392	0.335-0.663 (IH)
$\sin^2\theta_{13}$	0.0241	0.0169-0.0313 (NH)
	0.0244	0.0171-0.0315 (IH)
Δm^2_{21}(eV^2)	7.54 $\times 10^{-5}$	6.99-8.18 $\times 10^{-5}$
$|\Delta m^2_{31}|$(eV^2)	2.43 $\times 10^{-3}$	2.19-2.62 $\times 10^{-3}$ (NH)
	2.42 $\times 10^{-3}$	2.17-2.61 $\times 10^{-3}$ (IH)

Table 1.1: The current best fit values of the neutrino oscillation parameters [54] for the global analysis of neutrino data.

differences $\Delta m^2_{21}, \Delta m^2_{31}$ have been measured. Table 1.1 shows the current best fit values and errors on these parameters for the analysis of global neutrino data [54].

The sign of Δm^2_{21} is determined to be positive from the solar neutrino data. This allows for two different arrangements of the three neutrino mass states as shown in Fig. 1.8. If $\Delta m^2_{31} > 0$ then the mass hierarchy (MH) is defined to be normal. If $\Delta m^2_{31} < 0$, the mass hierarchy is defined to be inverted.
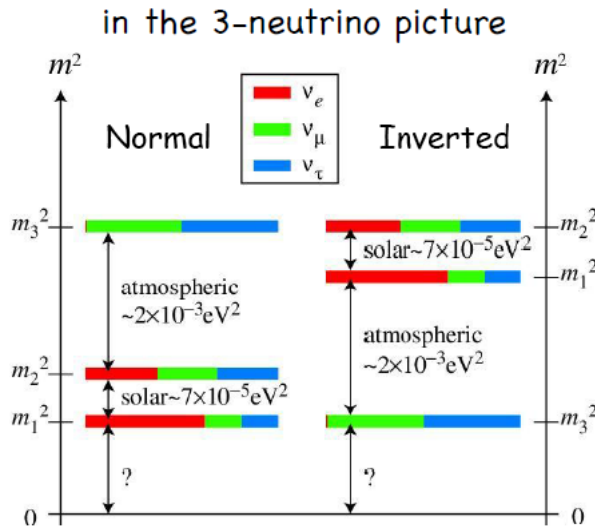
Figure 1.8: Normal and Inverted neutrino mass hierarchy

There are still many important unanswered questions regarding neutrino oscillations and masses.

1. What is the neutrino mass hierarchy ?

2. What is the value of $\delta_{\rm CP}$?

3. Is the mixing angle θ_{23} exactly equal to $\frac{\pi}{4}$? If not, then what is its octant ?

4. Are there sterile neutrinos in addition to three active flavors?

5. What are the absolute neutrino masses?

6. Are neutrinos Dirac or Majorana particles?

Most of the current and planned oscillation experiments will now try to address the first two questions. These experiments include NOνA [55, 56, 57], LBNE [58], LBNO [59, 60, 61], PINGU [62], ORCA [63], HK [64], T2HK [65], JUNO [66] and RENO-50 [67]. They will employ novel detector technologies, intense neutrino sources, long baselines and some of them will be of mega tonne mass to collect huge statistics.

The current constraints on the absolute neutrino masses have been obtained from cosmological data [68, 69, 70], from neutrinoless double beta decay [71, 72], and from tritium beta decay experiments [73, 74]. The neutrinoless double beta decay experiments will also seek to answer the question of whether the neutrinos are Dirac or Majorana particles.

1.6   Conclusion

Since the discovery of neutrino oscillations in 1964, the field of neutrino oscillation has made a tremendous progress. Neutrino oscillations are a neat example of quantum mechanical interference. The propagation of neutrinos and their oscillation probabilities can significantly be modified in the presence of matter.

After the observation of a deficit in the solar and atmospheric neutrino prediction, various solar, atmospheric, reactor and accelerator neutrino experiments have established neutrino oscillations to a high degree of confidence. In the standard three flavor oscillations, all three mixing angles and two mass squared difference have been

measured. The upcoming experiments are now being fine tuned to discover the neutrino mass hierarchy and to measure the phase δ_{CP} along with the other unknown quantities. The field of neutrino oscillation is expected to be as vibrant in the future as it has been in the past.

Chapter 2

The India-based Neutrino Observatory (INO)

The India-based Neutrino Observatory (INO) [75] is an upcoming facility for a number of experiments. The primary experiment in INO will be the Iron CALorimeter (ICAL) for studying neutrino oscillations. Additionally, it will host experiments for Neutrino-less Double Beta Decay (NDBD) and for direct dark matter search. In this chapter, we discuss some important aspects of the ICAL experiment.

2.1   Location

INO will be located in the Theni district of the state of Tamilnadu in Southern India. Fig. 2.1 shows the location of Theni. It is located approximately 110 km away from the city of Madurai. The site for the ICAL experiment has been chosen keeping in mind the geological stability of the region, availability of water, electricity and other infrastructure facilities. Also, the impact on the local environment due to the construction activities will be minimal at this location. The control center for the ICAL is being set up at Madurai.

The cavern for the INO will be constructed under the mountain, which will provide a rock cover of minimum 1 km in all directions to shield the experiments from the

20
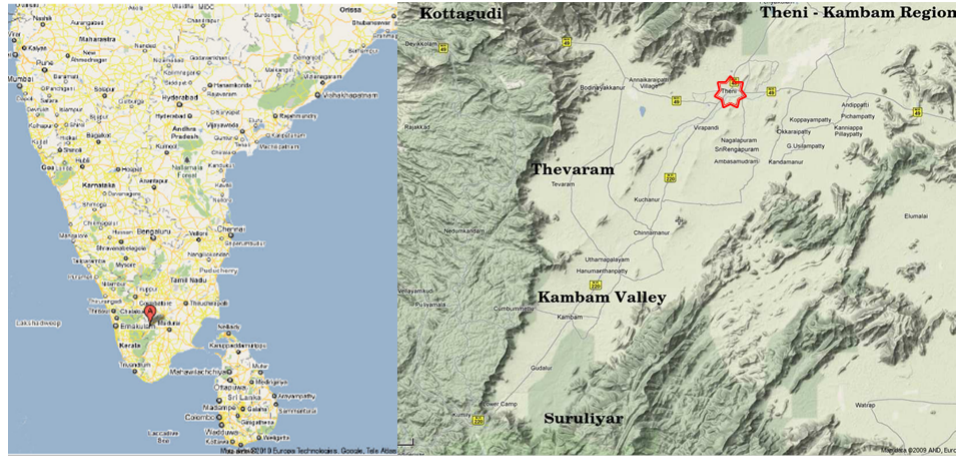
Figure 2.1: The location of Theni. The picture on the right shows the terrain at Theni.

cosmic muons. Fig. 2.2 shows the layout of the underground laboratory. The hall for the ICAL will have sufficient space for a 100 kt detector. A 3 km long access tunnel will be constructed under the mountain to reach the ICAL experiment hall.

2.2 The Iron CALorimeter (ICAL)

The Iron CALorimeter (ICAL) is a 50 kt magnetized detector to detect neutrino interactions induced by the atmospheric neutrinos. In the distant future, it may also serve as a far detector for a Neutrino Factory (NF) in a long baseline experiment. The detector is fine tuned to measure muon momentum produced in CC ν_μ interactions. It is also capable of detecting hadron showers produced in CC and NC neutrino interactions.

2.2.1 Primary Goal of the ICAL

The primary physics goals for the ICAL are as listed below.
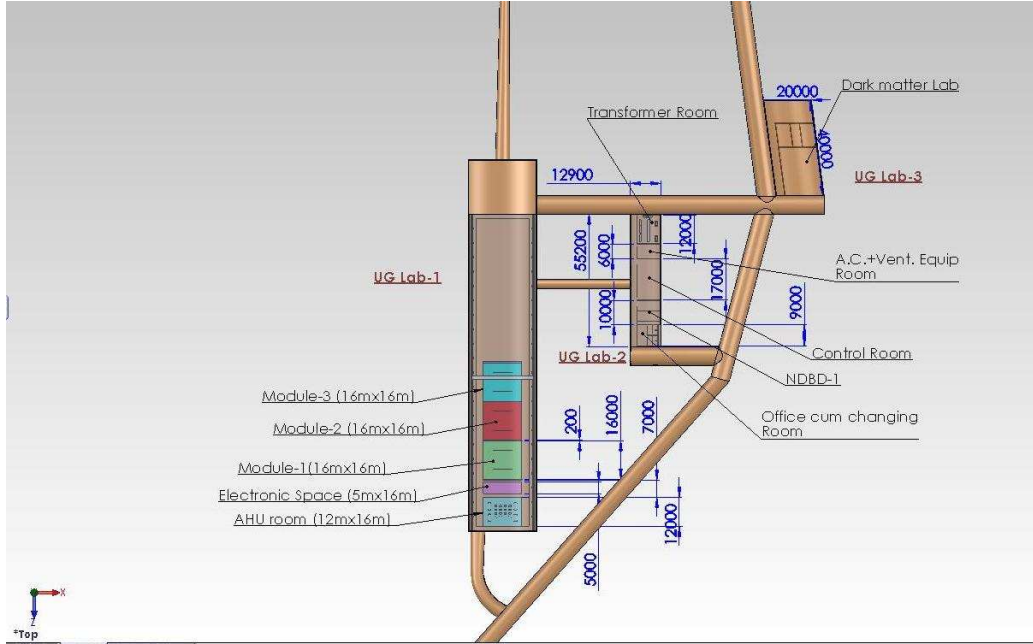
Figure 2.2: The layout of the INO cavern

1. Determine the neutrino mass hierarchy.

2. Make precision measurements of the parameters, $\sin^2 \theta_{23}$ and $|\Delta m_{32}^2|$.

3. Study of CP violation in the neutrino sector and test of CPT invariance.

4. Study of Non-Standard Neutrino Interactions (NSI).

5. Test the sterile neutrino oscillation hypothesis.

6. Observation of high energy cosmic muons and to determine the ratio the numbers of μ^- and μ^+.

Most of these goals will be achieved through the observation of the matter effects in the $P_{\mu\mu}$ survival channel.

2.2.2 The Design of the ICAL

In order to meet most goals of the ICAL experiment, the proposed detector should have as large mass as possible, in order to collect statistically significant number of

events. It should have good energy and direction resolutions for muons and neutrinos. And it should be economical to build. Keeping in mind these requirements, the INO collaboration has chosen the ICAL detector as described below for the oscillation experiment.
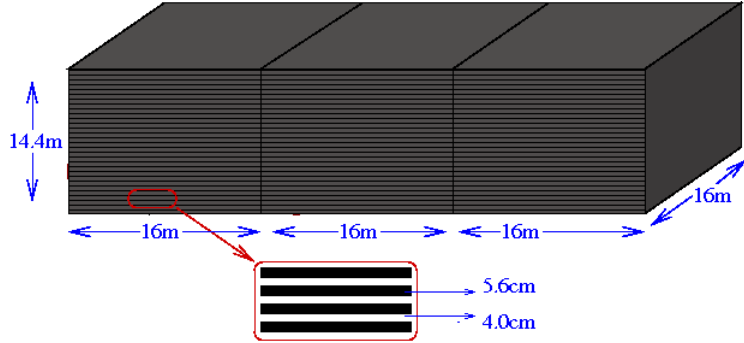
Figure 2.3: A schematic diagram of the ICAL detector

The detector consists of 3 identical modules, with dimensions 16 m × 16 m × 14.4 m. It consists of 150 alternate layers of iron plates and Resistive Plate Chambers (RPCs). The modular structure of the detector allows flexibility in the construction and operation. Data taking can start as soon as one of the modules is complete. The iron plates act as the target mass for the neutrino interactions. The RPCs are the active detection elements, which measure the passage of particles through them. The iron plates are magnetized with an average magnetic field of 1.5 Tesla. The magnetic field causes a charged particle to travel along a curved path. Fig. 2.3 shows the layout of the ICAL detector. The current specifications for the ICAL detector and RPCs is given in Table 2.1. These numbers have been chosen based on the ICAL detector simulations keeping in mind the balance of the detector performance and the cost.

The major components of the ICAL experiment are under research and development at the various INO collaborating institutes, universities and at industrial facilities. An engineering prototype of the ICAL with the RPCs, iron plates and the magnet is planned at the Madurai center.

Number of modules	3
Module dimensions	16m × 16m × 14.5m
Detector dimensions	48.4m × 16m × 14.5m
Number of layers	150
Iron plate thickness	56 mm
Gap for RPC trays	40 mm
Gap for RPC trays	40 mm
Magnetic field	1.3–1.5 Tesla

Table 2.1: Important parameters of the ICAL detector according to the current specifications

2.3   ICAL Particle Detection Capabilities

The signature of neutrino oscillation is contained in the $(E_\nu, \cos\theta_\nu)$ distribution of the neutrino events observed in the detector. The CC interactions of neutrinos produce charged leptons in the final state. Hence, the distribution of muon and electron events also contain the oscillation signature.

The CC ν_μ interactions produce muons and hadrons in the detector. Muons lose their energy primarily through ionization, as they propagate through the detector. The direction of propagation is affected by multiple coulomb scattering and the magnetic field in the detector. They typically give one hit point per RPC layer. The hits in different layers can be joined to form a muon track. The muon energy (E_μ), direction $(\cos\theta_\mu)$ and its charge can then be reconstructed using the information of the hit position and time. Measurement of the muon E_μ and $\cos\theta_\mu$ along with its charge is the mainstay of the ICAL detector. As discussed in Chapter 3, the muon energy can be reconstructed with resolutions of (10–25)%. The cosine of the muon zenith angle $\cos\theta_\mu$ can be reconstructed with resolutions of 0.005–0.045. (Equivalently, the θ_μ resolution is of about 1°).

The hadrons passing through the ICAL give rise to hadron showers, whose energy can be calibrated. The hadron energy, $E'_h = E_\nu - E_\mu$ can be measured with resolutions of (40–80)% [76]. The hadron shower direction $(\cos\theta_h)$ may also be reconstructed. By combining the energy and direction of the muons and hadrons, one can reconstruct the neutrino energy(E_ν) and direction$(\cos\theta_\nu)$ [77]. The ability to observe the hadron

showers in the GeV energy range is a unique feature of the ICAL, where the matter effects in the neutrino oscillation are important.

The ICAL physics analysis can be carried out using a subset of these observables, e.g. E_ν, $\cos\theta_\nu$, E_μ, $\cos\theta_\mu$, E'_h and $\cos\theta_h$. For the work presented in this thesis, we have carried out the analysis using the observables $(E_\mu, \cos\theta_\mu)$.

The CC interaction of ν_e gives rise to electrons in the final state. Since the electrons lose their energy rapidly due to ionization and bremsstrahlung, they can cross only a few layers of RPC. With fewer hits, the energy and direction of electrons cannot be reconstructed in the ICAL. The neutral current events of all neutrino flavors produce only the hadron showers. It may be possible to distinguish the hit points created by an electron and those produced in the NC showers. If the CC ν_e events can be identified, they may lead to enhancement of the ICAL physics sensitivities.

2.4 Resistive Plate Chambers (RPCs)

The Resistive Plate Chamber forms the heart of the ICAL detector. It is a gaseous detector, based on the principle of ionization of gas through charged particles. The RPCs were first introduced in 1981 by R. Santonico and R. Cardrelli to simplify and overcome the operation of Planar Spark Chambers [78]. The RPCs are easy and inexpensive to construct and offer a robust operation. The RPCs have large output signals and good timing resolutions of about 1 ns. They give spatial resolution of a few cm. All these characteristics make them a desirable choice for the ICAL detector.

2.4.1 Construction

The basic features of an RPC detector is shown schematically in Fig. 2.4. An RPC consists of two parallel electrodes which have large bulk resisitivity ($10^{10} - 10^{12}$ $\Omega - cm$). Typically glass or bakelite is used to construct the electrodes. The electrodes are separated by a few mm by means of spacers. A high voltage is applied across the electrodes to form a uniform electric field between the two planes. To ensure the uniformity of the field, the electrodes are coated with a thin layer of graphite. On
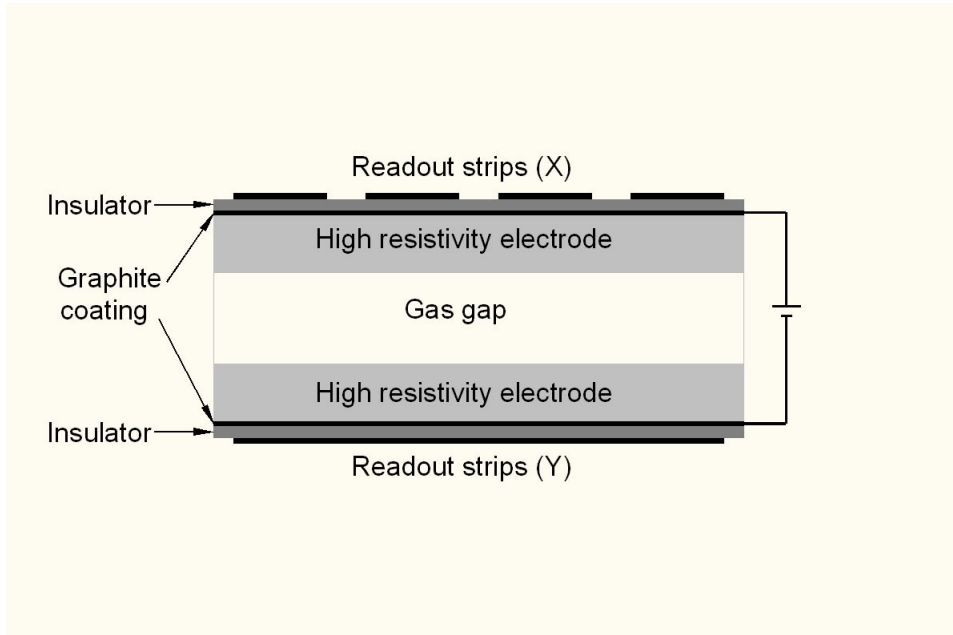
Figure 2.4: Layout of the Resistive Plate Chamber

top of the graphite layer, an insulating layer is applied to isolate the readout strips from the electrodes. The spacers are made from high bulk resistivity polycarbonate material. The volume between the electrodes is filled with a gas mixture, which makes up the ionizing medium. Generally, the gas mixture consists of Freon (Avalanche mode), Argon (Streamer mode), Isobutane and SF_6. The exact gas mixture and their proportion depend on the mode of operation as explained below.

2.4.2 Principle of Operation

An energetic particle passing through the RPC ionizes gas (Freon or Argon) along its trajectory. Electrons and ions produced in ionization start travelling towards anode and cathode, respectively. While the drift speed of electrons is large, ions move at a lower speed. The primary electrons, being accelerated in the electric field, produce further ionization of the gas on their way to the anode. As they move towards the anode, they induce a signal on the nearest pick up strip.

Due to the electron-ion recombination process, photons are produced in the gas, which may give rise to secondary ionization at points far from the primary ionization

area. The remedy to this problem is Isobutane, which absorbs the photons, preventing them to travel far in the gaseous volume. An electronegative gas such as Freon absorbs the free electrons produced in an avalanche triggered by the primary ionization, thus preventing the onset of the streamer mode (as explained below). The high resistive electrodes keep the area of discharge limited so that the rest of the detector can still remain active. The uniform application of an electric field gives RPCs very good timing resolutions compared to wire chambers.

The RPCs can be operated in (i) Avalanche, and (ii) Streamer modes.

1. **Avalanche Mode :** In this mode, the primary ionization causes multiplication of electrons, as those initially produced are accelerated towards the cathode. The avalanche mode of operation is suitable for high particle rate applications. However, the signal induced with this mode is low($\sim$ 1 pC), requiring an amplifier in the front-end electronics the for read out systems. This mode of operation keeps the RPC aging low and it can be operated continuously for long period of time.

2. **Streamer Mode :** In the streamer mode, the gas gain is set high by reducing the amount of the photon absorbing gas. When the photons propagate large distances, they cause additional avalanches. A conductive channel may be formed between the two electrodes through which the local electrode surfaces are discharged. The streamer mode operation of RPC gives large signals of $\sim$ 100 pC, reducing the demand on the read out electronics. However, it currently suffers from aging problems. If the streamer mode is used in an experiment, the RPCs need to be replaced after a few years of operation.

There are different types of RPCs for different applications, such as Trigger RPC and Timing RPC. They can also have different designs like the single gap RPC, Double gap RPC, Multi-gap RPC, Micro RPC and Hybrid RPC. Currently, it is envisaged that single gap glass RPCs of dimensions $2 \times 2 \ m^2$ will be operated in avalanche mode for the ICAL experiment. Table 2.2 shows the current specifications for the RPCs [79]. The proposed scheme for the read out electronics and DAQ systems for the RPCs are described in [75].

Number of RPC layers	150
RPC dimensions	1,800 mm× 1,910 mm × 20 mm
Readout strip width	30 mm
Number of RPC units/Layer	192
Number of RPC units	28,800 (97,505 m^2)
Number of readout strips	3,686,400

Table 2.2: Current RPC specifications for the full 50 kt ICAL detector

2.4.3   Gas Flow System for RPC

The ICAL detector will have a recyclable gas system [75] to circulate the chosen gas mixture in the RPCs. Recycling of the gas will be economical and help to minimize the impact on the environment. The entire detector will be divided into several zones, with each zone having its own gas system. Argon, isobutane and R134a will be carried to the mass flow controllers for mixing according to the desired ratio. Uniform distribution in each zone will be accomplished by using flow resistors. To avoid the situation of over pressure, control of exhaust pressure and relief bubblers will be used.

2.5   The ICAL Magnet

The electromagnet of ICAL is an important component of the detector to achieve the primary physics goals of the experiment. The magnetic field is required to measure the energy and charge of the muons using the curvature of their trajectories in the magnetic field. The steel plates of the electromagnet also provide the target mass for neutrino interactions.

The exact design of the ICAL magnet will be governed by the following criteria.

- **Field Uniformity :** A uniform magnetic field is desired for optimal recon-
  struction of muon momentum and charge. In order to contain the magnetic
  field inside the iron plates and to minimize field leakage into air, a gap-less
  toroidal magnet design will be used.

Figure 2.5: Top : Arrangement for the ICAL magnet coil slots in three modules, Bottom : A single ICAL module with the coils inserted.

- **Modularity :** To ensure flexibility in the ICAL construction and operation, the detector will be constructed as independent modules with their own magnets.

- **Optimal Copper to Iron Ratio :** Operating costs and construction costs are governed by the copper to iron ratio. A higher value of the ratio results in lower power consumption and cooling requirement and hence lower operating cost, but at a higher fixed cost of construction. On the other hand, a lower value of the ratio results in higher operating cost and lower fixed cost. The cooling requirement is determined by temperature tolerances of other components of the detector, e.g. that of electronics and RPC operations.

Currently, a toroidal (gap-less) design is being envisaged for the ICAL magnet

[75]. In this design, the copper coils pass through two rectangular slots in the iron plates. Fig. 2.5 schematically shows the geometry of inserting the coils into the iron plates. The dimensions of the coil slots are chosen so that a uniform magnetic field can be generated in the iron plates in a large volume. This design also allows insertion and removal of the RPC trays easily.
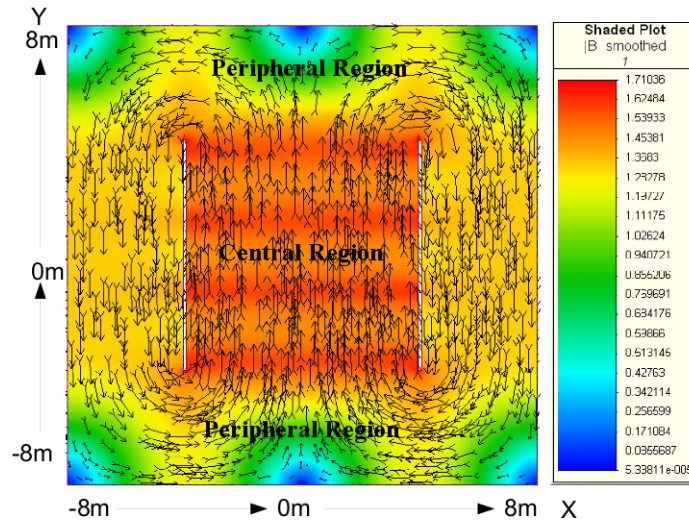
Figure 2.6: The magnetic field map in the X-Y plane for a single ICAL module

To produce an average field of 1.3 Tesla in a single module, a coil with a capacity of 40,000 ampere-turns is required. The field variation is less than 0.3% across the iron plates. Fig. 2.6 shows a simulated magnetic field map in a module in the X-Y plane. This map has been simulated with the Magnet 6.0 package [80]. The magnetic field is uniform in the central and in the side region of the module. The variation in the field is less than 0.25% along the X-axis. It changes rapidly in the peripheral region and changes direction. In the Y- direction, it starts falling beyond the coil length of 4 m. The reconstruction of muons depend significantly on the region of the magnetic field it passes through.

2.6 Chapter Summary

The Iron Calorimeter(ICAL) is an upcoming atmospheric neutrino experiment, whose primary goal is to determine the neutrino mass hierarchy. The total mass of the ICAL is approximately 50 kt. It is made up of 150 alternate layers of iron plates and RPCs. The iron plates are magnetized with an average field of 1.3 Tesla to enable the separation of ν_μ and $\overline{\nu}_\mu$ events. The ICAL is primarily optimized to measure the muon energy and direction with fine resolutions (10–15% and 1°, respectively) and high reconstruction efficiency(80%) as well as high charge identification efficiency ($\geq$ 95%). Various components of the ICAL detector are under research and development at the collaborating institutions.

Chapter 3

ICAL Detector Simulations for Muon Reconstruction

In order for the ICAL to achieve its oscillation physics goals, it needs to measure the $(E_\mu, \cos\theta_\mu)$ distribution of neutrino induced muons as accurately as possible, with a high efficiency. The ICAL experiment uses a Kalman Filter (KF) based algorithm to reconstruct the muon momentum and charge. Given the design and the geometry of the ICAL, it has a muon energy threshold of about 0.5 GeV.

The ICAL software code for the ICAL detector simulation and reconstruction has been developed by the INO collaboration. Fig. 3.1 shows the major steps performed for the ICAL simulations. The muon reconstruction for the ICAL is based on the concept of MINOS reconstruction [81, 82]. In this chapter, we briefly outline the steps involved in simulating and reconstructing muon tracks. Later, we describe the ICAL response to muons obtained from these simulations.

3.1   GEANT4 Simulations and Hits Digitization

The ICAL detector simulation code uses GEANT4 [83] to simulate the detector geometry and propagation of particles. The full ICAL detector geometry has been incorporated in GEANT4, including the iron plates, RPCs, spacers, support struc-

Neutrino Event Generator NUANCE/GENIE

ICAL Geometry and Magnetic Field Simulation in GEANT4

Fixed Energy/Direction particles for detector performance studies

Propagate particles in the ICAL through GEANT4, considering various physics processes

Obtain signals in the Sensitive Detector(RPCs)

Digitize the signals to obtain strip information

Muon and Hadron Reconstruction

Physics Analysis

Figure 3.1: ICAL Detector Simulation Chain

tures and the coils for the electromagnet. GEANT4, version 4.9.4.p02 has been used for the work presented here. The magnetic field map of the ICAL, obtained from the magnet simulation [80] is also specified as an input to GEANT4 simulation and muon reconstruction.

The task of the GEANT4 simulation, is then, to simulate the propagation of particles, given this geometry. The particles are propagated into the detector while taking into account all possible physics processes. GEANT4 starts propagating a particle in small steps from its vertex position, until the particle comes to the rest or it leaves the detector. For the results reported in this thesis, the production cut in GEANT4 was set to 0.01 mm. The production cut is the minimum distance by which GEANT4 must propagate the particle. The energy cut was set to (10 eV, 100 TeV).

As a particle passes through the sensitive detector (e.g. RPC), GEANT4 produces signals in the X and Y strips, called hits. The hit positions generated by GEANT4 are then digitized according to the strip width. In order to simulate a realistic detector, the hits are created with an inefficiency of 5% and with a multiplicity of 1.4 hits[1]. The final information stored for the particle reconstruction is the X and Y strip numbers, the RPC layer number, time of the hit and the pulse height. Even though the pulse height information is recorded, so far it is not being used in the event reconstruction.

Typically, muons passing through the detector give a hit point pattern with one hit per layer, though multiple hits in single layers are possible. These hits can be cleanly joined to form a muon track. When a hadron or an electron passes through the detector, it gives multiple hits per layer due to different energy loss mechanisms, creating a shower of hits. Fig. 3.2 illustrates the hit pattern created by a muon and hadron in a neutrino interaction.

Fig. 3.3 and Fig. 3.4 show the hit positions produced by a 1 GeV and 5 GeV muon in the ICAL detector. The reconstruction of muon momentum is carried out in two steps, (i) Track Finder, and (ii) Track Fitter, to be described in the following sections.

---

[1]These numbers are based on the on-going development studies of RPCs by the INO collaboration.
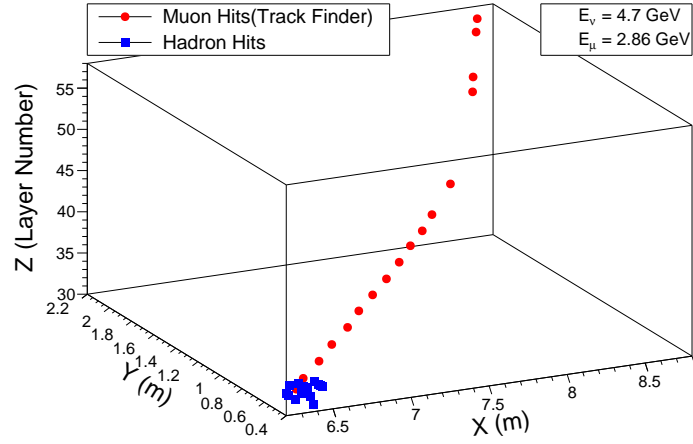
Figure 3.2: Hit pattern given by a muon and hadrons produced in a neutrino interaction. Muons typically produce one hit per layer, whereas hadrons produce multiple hits per layer.
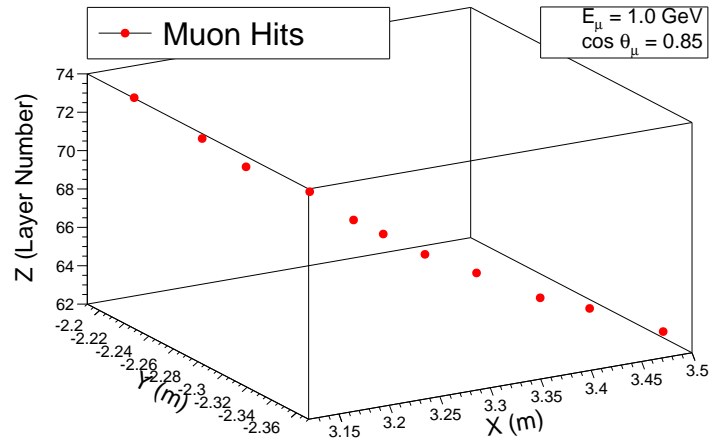
Figure 3.3: Hit pattern given by a 1 GeV μ^- with $\cos\theta = 0.85$ with vertex in the central region of the ICAL.
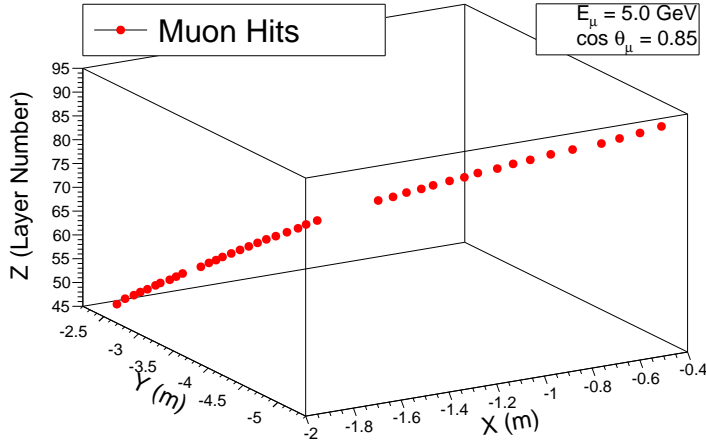
Figure 3.4: Hit pattern given by a 5 GeV μ^- with $\cos\theta = 0.85$ with vertex in the central region of the ICAL.

3.2 The Track Finder

The muon track reconstruction begins with the Track Finder algorithm, which starts by combining X, Y strip numbers and the layer number to form three dimensional hits. All possible hits are formed, considering multiple hits in a given strip and a given layer. These hits could have been generated due to the passage of a muon or a hadron. A simple algorithm which uses a criterion on the number of hits per layer is used to separate hits created by muons and hadrons.

Once the muon hits are identified, the Track Finder attempts to find possible muon tracks by progressively traversing along the muon hits along various paths. In this process, it forms various collections of hits called clusters, triplets, simple/matched/preferred associations of triplets. The ICAL Track Finder algorithm is similar to the one used for the MINOS far detector [81, 82]. Whether the muon is going in the upwards or the downwards direction is determined by the timing information of the hits.

3.3 The Track Fitter

After the Track Finder has selected the candidate hit points, the next task is to reconstruct the muon track. Most importantly, the muon energy, direction, charge and the vertex position need to be reconstructed for the physics analysis. The ICAL reconstruction package employs a Kalman Filter based reconstruction algorithm for the muon track reconstruction. It uses information about the muon energy loss, multiple scattering and the magnetic field to reconstruct the muon track.

3.3.1 The Kalman Filter

The Kalman Filter(KF) is a recursive algorithm [84, 85] to estimate the parameters of a dynamical system in the presence of process noise (due to stochastic driving process) and measurement noise (errors in the measurement). It was first proposed by R. E. Kalman in 1960. It has been shown that the Kalman Filter provides the optimal estimate of the parameters in case of a linear dynamic system. For non-linear systems, the Extended Kalman Filter technique has been developed [87]. Here, we briefly describe the discrete Kalman Filter method.

We start with the state vector defined as,

$$\mathbf{x}_k = (x, y, dx/dz, dy/dz, q/p), \tag{3.1}$$

where x and y are hit point positions, and dx/dz, dy/dz are the slopes with respect to the ICAL layers. And q and p are the charge and the momentum of the muon.

To understand the operation of the Kalman Filter, consider a z layer labelled (k-1). For this layer, we provide an initial guess for the state vector, $\mathbf{x}_{k-1}$ and an error covariance matrix $\mathbf{C}_{k-1}$. The goal is to obtain an estimate of the state vector in the next layer k. Given the motion of a muon in the presence of magnetic field and other physical processes, we construct a 5×5 propagation matrix $\mathbf{F}_{k-1}$. As the muon travels through the detector material, it loses energy through ionization. Its trajectory is also affected by coulomb multiple scattering. These two processes are stochastic processes, which constitute the process noise in the Kalman Filter

terminology. The process noise covariance matrix $\mathbf{Q}_{k-1}$ is evaluated for the current layer. Finally, the measurement function $\mathbf{H}_k$ and the measurement error covariance matrix $\mathbf{V}_k$ are constructed. The measurement function $\mathbf{H}_k$ is taken to be,

$$\mathbf{H}_k = \begin{pmatrix} 1 & 0 & 0 & 0 & 0 \\ 0 & 1 & 0 & 0 & 0 \end{pmatrix}. \tag{3.2}$$

The measurement error matrix is calculated by taking the error in the position measurement to be $w/\sqrt{12}$, where w is the strip width.

With these inputs, the KF algorithm predicts the state vector $\mathbf{x}_k$ in the next layer of the detector. An important quantity, called the Kalman gain, $\mathbf{K}_k$ is calculated from the state covariance matrix $\mathbf{C}_k$. The Kalman gain decides whether the prediction, $\mathbf{F}_{k-1}\mathbf{x}_{k-1}$ for the next layer, or the measurement $\mathbf{m}_k$, has more influence on the filtered state vector.

The Kalman update equations are as follows.

$$\mathbf{C}_k^{k-1} = \mathbf{F}_{k-1}\mathbf{C}_{k-1}\mathbf{F}_{k-1}^T + \mathbf{Q}_{k-1}, \tag{3.3}$$

$$\mathbf{K}_k = \mathbf{C}_k^{k-1}\mathbf{H}_k^T \left(\mathbf{V}_k + \mathbf{H}_k\mathbf{C}_k^{k-1}\mathbf{H}_k^T\right)^{-1}, \tag{3.4}$$

$$\mathbf{x}_k = \mathbf{F}_{k-1}\mathbf{x}_{k-1} + \mathbf{K}_k \left(\mathbf{m}_k - \mathbf{H}_k\mathbf{F}_{k-1}\mathbf{x}_{k-1}\right), \tag{3.5}$$

$$\mathbf{C}_k = \left(\mathbf{1} - \mathbf{K}_k\mathbf{H}_k\right)\mathbf{C}_k^{k-1}. \tag{3.6}$$

Eqn. 3.3 extrapolates the state covariance matrix $\mathbf{C}_{k-1}$ to the next layer, denoted as, $\mathbf{C}_k^{k-1}$. Together, Eqn. 3.3–3.6 extrapolates the state vector and the error covariance matrix to the next layer. The same procedure is followed for the subsequent layers, by relabelling them as $(k-1)^{th}$ layer. This iteration is started from the first layer of hit, where x,y are taken from the hit in that layer, dx/dz, dy/dz are taken from hits in first two layers and q/p is set to 0. After iterating over the entire track in the forward and reverse direction several times, the state vectors for various layers converge, if the KF algorithm succeeds. We are most interested in the state vector at the beginning of the track, which gives an estimate of the muon vertex position, as well as its momentum, direction and charge.

3.3.2   Implementation of the Propagator and the Noise Matrices

By assuming that the muon always moves perpendicular to the z layers, the propagation matrix $\mathbf{F}_{k-1}$ is written as follows.

$$\mathbf{F}_{k-1} = \begin{pmatrix} 1 & 0 & \delta z & 0 & \frac{1}{2}B_y\delta z^2 \\ 0 & 1 & 0 & \delta z & -\frac{1}{2}B_x\delta z^2 \\ 0 & 0 & 1 & 0 & B_y\delta z \\ 0 & 0 & 0 & 1 & -B_x\delta z \\ 0 & 0 & 0 & 0 & 1+\epsilon \end{pmatrix}, \tag{3.7}$$

where B_x, B_y and B_z are the components of magnetic field and δz is the distance between two RPC layers. In order to extrapolate the muon momentum (q/p) to the next layer more accurately, a numerical method is used to obtain the element $(\mathbf{F}_{k-1})_{55}$, as described below.

The propagation of a muon from one layer to the next is done using the Swimmer package [88]. The Swimmer package works by numerically propagating the muon in small steps of 5 mm to the next layer. For each small step, the coordinate system is rotated in such a way that the magnetic field points along the z direction in the local frame. The muon follows a helical trajectory in this local coordinate system whose equation of motion is simplified. For every small step taken by the Swimmer package, $|\mathbf{B}|$ is considered to be constant and the ionization energy loss is subtracted from the starting energy of the muon. As we hit the next layer, the Swimmer package transform the coordinate system to the ICAL frame and gives the state vector prediction. Thus the state vector $\mathbf{x}_k$ is obtained numerically. The last column of $\mathbf{F}_{k-1}$ can then be obtained by linearizing the propagator function about the current state vector.

3.3.3   Implementation of the Noise Covariance Matrix

The propagation of a muon is affected by fluctuations in its energy loss and multiple scattering through small angles. In order to account for these stochastic processes,

the noise covariance matrix is constructed as,

$$\mathbf{Q}_k = \begin{pmatrix} \mathbf{Q}_k^{MS}{}_{4\times 4} & 0_{1\times 1} \\ 0_{1\times 1} & \mathbf{Q}_k^{\delta E}{}_{1\times 1} \end{pmatrix}, \tag{3.8}$$

where $\mathbf{Q}_k^{MS}$ is the 4×4 block matrix related to the multiple scattering. $\mathbf{Q}_k^{\delta E}$ is the standard deviation of the muon energy loss. The description of $\mathbf{Q}_k^{MS}$ can be found in [81, 82] and in [86].

The energy loss term $\mathbf{Q}_k^{\delta E}$ is evaluated as,

$$\mathbf{Q}_k^{\delta E} = \left(0.25 \frac{\Delta E}{p^2} \frac{ds}{dz} \right)^2. \tag{3.9}$$

Here, ΔE is the mean energy loss for a muon travelling perpendicular to the layer and s is the length travelled by the muon.

3.3.4 The Output of the Kalman Filter

We obtain the state vector estimate for each layer from the track fitter. Of particular importance are the muon energy and the direction at the estimated vertex position. If the track is reconstructed as two or more tracklets, then the above information is reported for each tracklet. The goodness of the track fitting is found by calculating the χ^2 defined as:

$$\chi^2 = \sum_i \left[\left(\frac{x_i^{filtered} - x_i^{measured}}{\sigma_x} \right)^2 + \left(\frac{y_i^{filtered} - y_i^{measured}}{\sigma_y} \right)^2 \right], \tag{3.10}$$

where $x_i^{filtered}$ and $y_i^{filtered}$ are the filtered x and y positions for the ith hit point. $x_i^{measured}$ and $y_i^{measured}$ are the measured x and y positions. σ_x $(= w/\sqrt{12})$ and σ_y $(= w/\sqrt{12})$ are the errors in x and y position measurements. The degrees of freedom are calculated as $dof = 2N_{hits} - 5$, with N_{hits} being the number of hit points.

Fig. 3.5 and Fig. 3.6 show the comparison of the raw hits, track fitter hits and the track finder hits for two muons with $E_\mu = 1$ GeV, travelling at two different zenith
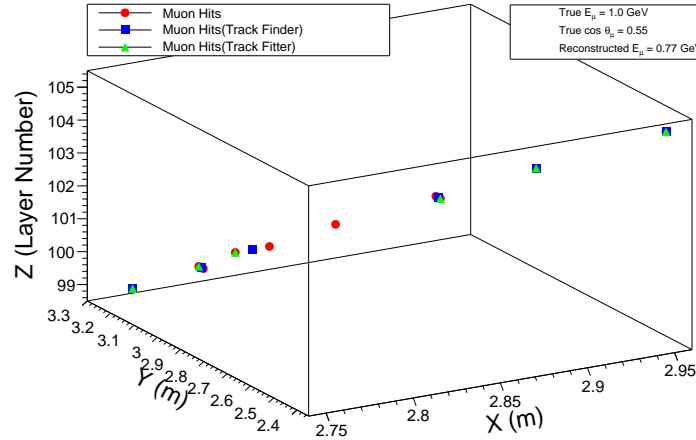
Figure 3.5: Hits selected by the Track Finder and the Track Fitter algorithm for 1 GeV μ^- with $\cos\theta = 0.55$. This track is reconstructed at 0.77 GeV.

angles.

3.4   Muon Response Parametrization

In the data analysis of the real ICAL experiment, one would use the reconstructed energy and direction of particles to obtain the predicted distribution of muons and hadrons. This would involve passing the generator level particle information through the reconstruction code, imposing various cuts on events, based on the position and timing of the hit points and the goodness of track reconstruction. However, this is a complicated task, which requires a very detailed detector simulation analysis. To simplify the physics analysis in the current work, the detector response to muons has been parametrized in terms of four important quantities : (i) energy resolution (σ_E), (ii) zenith angle resolution ($\sigma_{\cos\theta}$), (iii) reconstruction efficiency (ϵ_R), and (iv) charge identification efficiency, CID (ϵ_C). All these quantities are obtained as a function of true muon energy (E_μ) and direction ($\cos\theta_\mu$), separately for μ^- and μ^+. They are stored in the form of a look-up table for use in the physics analysis.

41
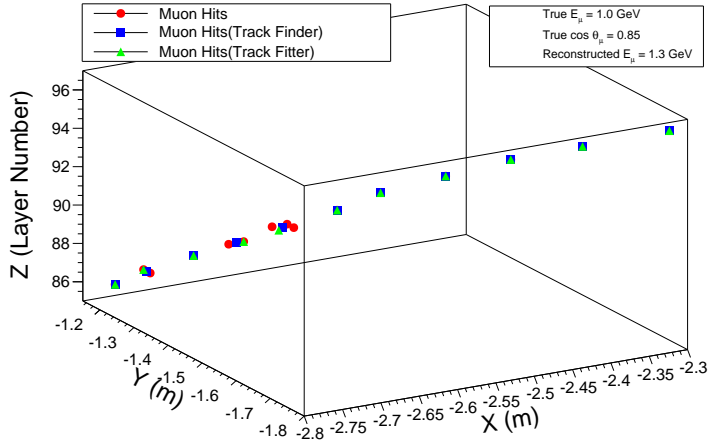
Figure 3.6: Hits selected by the Track Finder and the Track Fitter algorithm for 1 GeV μ^- with $\cos\theta = 0.85$. This track is reconstructed at 1.3 GeV.

3.4.1 Inputs to prepare the Look-up table

To obtain the look-up table, we simulate 10,000 muons of fixed energy(E_μ) and zenith angle($\cos\theta$) using the ICAL simulation. The vertex position of the muons is set in the central volume of the detector with a uniform smearing of $\pm(400,400,600)$ cm around the point $(0,0,0)$, which is the centre of the detector. The magnetic field is approximately uniform in this region except for the boundaries (Fig. 2.6). We assume that the detector response obtained in this region can be extrapolated to the entire volume of the detector. The azimuthal angle ϕ is smeared uniformly between $(0-2\pi)$. The energy and direction (E_μ, $\cos\theta_\mu$) are not smeared. We have also assumed here implicitly that the muon and hadron hit separation efficiency is 100%. Background hits from other sources such as CC ν_e and NC events, cosmic muons, random noise are neglected. As the ICAL detector simulation progress, these assumptions will be relaxed in future and a more detailed analysis will be performed.

We have prepared the look-up table in the range, $E_\mu = [0.6,25]$ GeV (20 sample points), and for $\cos\theta = [-1,1]$ (20 sample points). This is the muon energy range, relevant for the ICAL oscillation analysis. For each one of the 400 possible combinations of energy and direction, we simulate, digitize and reconstruct the muon tracks to obtain the distributions of reconstructed energy and direction.

(a) E_μ=0.8 GeV

(b) E_μ=1 GeV

(c) E_μ=5 GeV

(d) E_μ=15 GeV
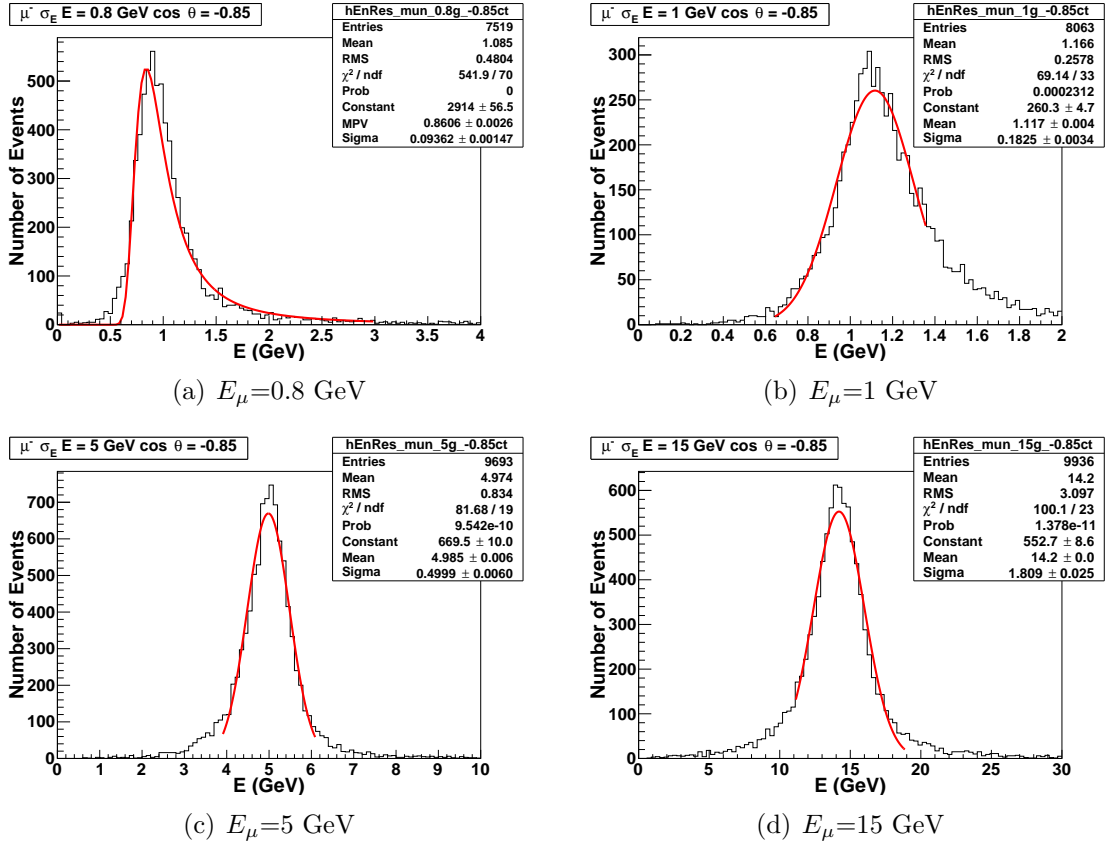
Figure 3.7: Reconstructed energy distribution for $\cos\theta_\mu$=-0.85 for four different muon energies : (a) E_μ=0.8 GeV, (b) E_μ=1 GeV, (c) E_μ=5 GeV, and (d) E_μ=15 GeV

3.4.2 Muon Resolutions and Efficiencies

Fig. 3.7 shows a few distributions of the reconstructed E_μ. Only those events are selected to make the reconstructed distributions, for which $\chi^2/ndf < 10$. We notice that the muon energy resolutions are strong functions of true energy and direction. We notice also that the reconstructed energy distributions have tails or a hump structure on one or both sides of the peak.

The deviation of the shape from the Gaussian distribution mainly arise because the muon reconstruction algorithm has not yet been completely fine tuned. For example, in cases, where a muon is passing through the support structure, hit points may be missing for several layers. The KF algorithm does not get measurements for these layers to produce an accurate filtered output in this part of the track, which results in

poor reconstruction. This issue is more relevant for those tracks which are travelling in near vertical directions, and also for the high energy muons, which are likely to travel long paths through the vertical support structures. In such cases, a genuine single track may be reconstructed as multiple tracklets and with poor resolution. Some other dead spaces such as the RPC gaps and the magnet coils also create similar effects. Partially contained events also give rise to poor energy reconstruction. Although, we obtained the azimuthal angle averaged muon response, more realistically, the ICAL response is ϕ dependent [77]. The direction of the magnetic field and the different detector dimensions along the X and Y direction break the azimuthal symmetry.

The normal distribution function cannot be fitted with the reconstructed energy distribution in the full range in most cases. A Landau distribution convoluted with the Gaussian function would make more appropriate fits to these distributions. While the ICAL muon reconstruction algorithms are being updated, we obtain the energy resolutions and efficiencies from the current reconstruction code as follows to keep the analysis simple. We perform fits with the normal distribution function around the peak of the distribution, in the range $E\mu \pm$ FWHM, where FWHM is the full width at half maxima found from the distribution. We obtain better fits in this restricted energy range. Fig. 3.7 shows such fits superimposed on the distributions. Such fits give a reduced χ^2 of about 2–8. The standard deviation σ obtained from this fit gives the energy resolution σ_E. In case of $E_\mu < 1$ GeV, the Landau distribution function is used for the fitting.

The relative muon energy resolution (R) at energy E_μ is defined as,

$$R = \frac{\sigma_E}{E_\mu} \tag{3.11}$$

While the above fitting procedure is somewhat arbitrary, it is expected that with the further development of the ICAL reconstruction algorithms, the deviation of non-gaussian distribution will be largely suppressed. Therefore, we optimistically calculate the muon reconstruction efficiency in the range $E \pm 5\sigma_E$. The reconstruction efficiency and its error are defined to be,

$$\epsilon_R \equiv \frac{\text{Number of reconstructed muons}(N_R)}{\text{Number of incident muons}(N_{\text{Total}})}, \tag{3.12}$$

$$\delta\epsilon_R = \sqrt{\frac{\epsilon_R(1-\epsilon_R)}{N_{\text{Total}}}}, \tag{3.13}$$

where N_R and N_{Total} are the number of reconstructed (in the range $E \pm 5\sigma_E$) and incident muon events (=10,000).

The CID efficiency and its error are defined as,

$$\epsilon_{\text{CID}} \equiv \frac{N_{\text{CID}}}{N_R}, \tag{3.14}$$

$$\delta\epsilon_{\text{CID}} = \sqrt{\frac{\epsilon_{\text{CID}}(1-\epsilon_{\text{CID}})}{N_R}}, \tag{3.15}$$

where N_{CID} is the number of muon events reconstructed with correct muon charge (in the range $E \pm 5\sigma_E$).

Fig. 3.8 shows the reconstructed muon $\cos\theta_\mu$ distributions. Here, the double-Gaussian function fits may be used. However, for simplicity in the analysis, we use the normal function fits to obtain the $\cos\theta$ resolutions in all cases.

3.4.3 Results

Fig. 3.9 shows the ICAL muon response for three representative directions, e.g. $\cos\theta_\mu$ = -0.85, -0.55 and -0.35. Figure 3.9(a) shows the relative energy resolution as a function of true energy. It can be seen that as the muon energy increases from 1 GeV to 7 GeV, the resolution improves. In this range, with the increasing muon energy, more hits are produced in different layers, with appreciable bending of the muon in the magnetic field, which results in better energy estimation. At higher energies, the muon starts to leave the detector, giving partially contained events. The curvature of the muon also reduces due to high energy. These factors results in the poor track fit and hence the energy resolutions begin to worsen. In general, the muons which travel vertically have better resolutions than the one which travel horizontally. (Excluding

(a) E_μ=0.8 GeV

(b) E_μ=1 GeV

(c) E_μ=5 GeV

(d) E_μ=15 GeV
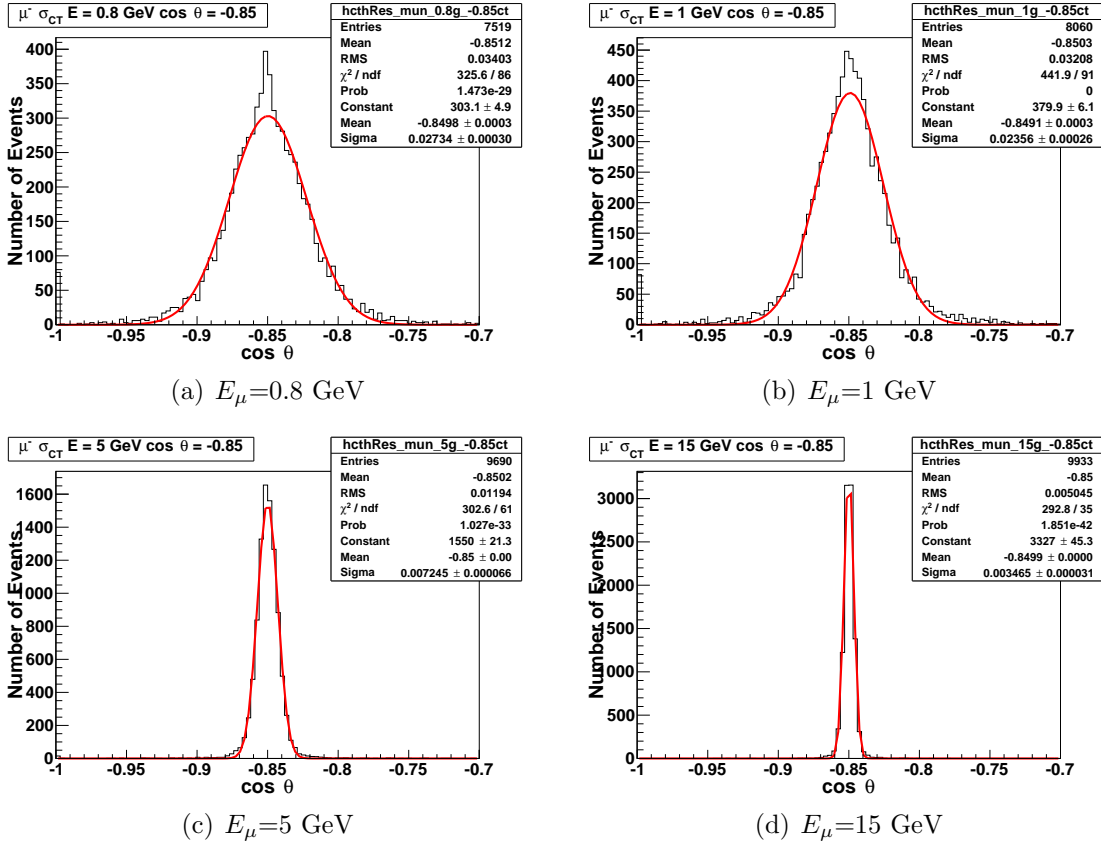
Figure 3.8: Reconstructed $cos\theta$ distribution for $\cos\theta_\mu$=-0.85 for four different muon energies : (a) E_μ=0.8 GeV, (b) E_μ=1 GeV, (c) E_μ=5 GeV, and (d) E_μ=15 GeV

the muon which goes in between two RPC layers.) The muon energy can be best reconstructed in the energy range 5–8 GeV.

Fig. 3.9(b) shows the muon direction reconstruction, in terms of $\cos\theta_\mu$. Here, the double-Gaussian function fits might be used. However, for simplicity in the analysis, the $\cos\theta$ resolution is obtained by fitting the normal distribution function to the reconstructed $\cos\theta$ distribution in all cases. The $\cos\theta_\mu$ resolutions are found to be in the range 0.005–0.045. They always improve with the increasing energy, consistent with the fact that higher energy muons create more hit points, resulting in better direction reconstruction from the fit. This corresponds to a zenith angle reconstruction of better than 1°.

Fig. 3.9(c) shows the efficiencies of muon reconstruction. The reconstruction ef-

(a) Energy Resolution

(b) $\cos\theta_\mu$ Resolution

(c) Reconstruction Efficiency
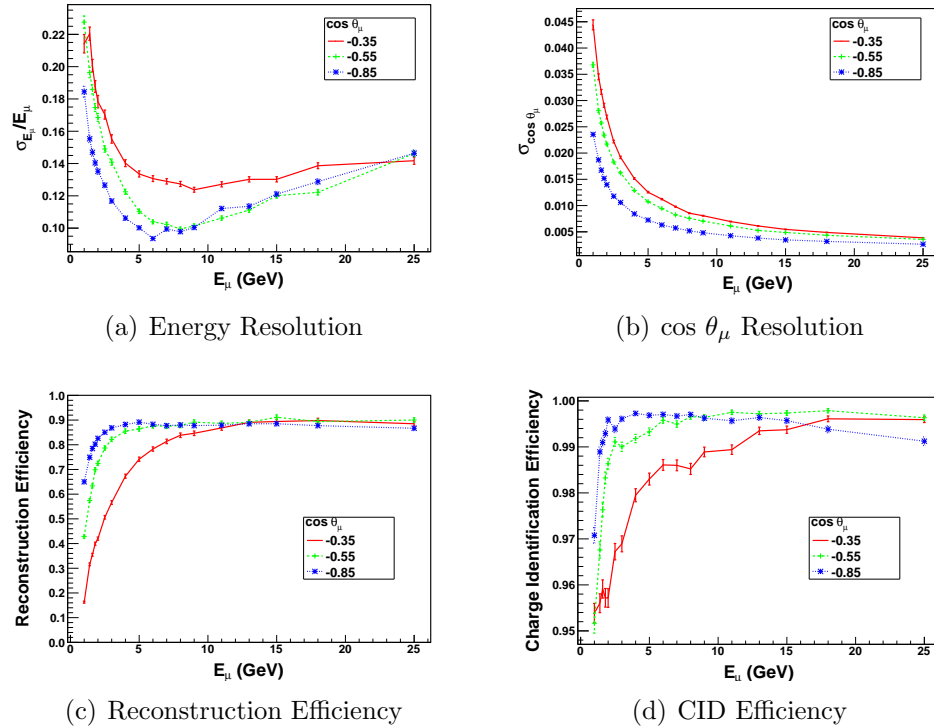
(d) CID Efficiency

Figure 3.9: The energy resolution (a), $\cos\theta_\mu$ resolution (b), the reconstruction efficiency (c), and the charge identification efficiencies (d), for μ^- as a function of the true muon energy and for three cases of true muon zenith angle. The red, green and blue lines are for the zenith angle bins with $\cos\theta_\mu = (-0.4, -0.3), (-0.6, -0.5), (-0.9, -0.8)$ respectively.

ficiency improves with the energy, ranging from about 40% at 1 GeV to 80% at 15 GeV, for $\cos\theta_\mu$ = -0.55. This trend is again consistent with the fact that with higher muon energy, more hits are available to the KF for reconstruction. The efficiency of reconstruction becomes poor for $|\cos\theta_\mu| < 0.25$, due to small number of hits. At almost horizontal angles, e.g. $\cos\theta_\mu$=0.05, the efficiency of reconstruction becomes zero.

Finally, Fig. 3.9(d) shows the muon charge-identification (CID) efficiency. It is seen to be varying from 95% at 1 GeV to almost 100% at 15 GeV. At still higher energy, it slightly degrades due to the small curvature of the muon in the magnetic field. As will be seen in Chapter 5, the high CID efficiency of ICAL plays an important role for the neutrino mass hierarchy determination.

The up-going and down-going muons exhibit identical muon response. The reconstruction of μ^+ is also identical to that of μ^- for all energies and angle. Both these features are expected from symmetry considerations.

3.5   Chapter Summary

The ICAL experiment is optimized primarily for measuring the muon momentum and the zenith angle with good resolutions and efficiencies to achieve its physics goals. A muon passing through the ICAL gives rise to a hit pattern which can be joined to form a track, whereas a hadron passing through the ICAL gives rise to a hadron shower pattern. The muon momentum can be estimated by measuring its curvature in the magnetic field of the detector. A GEANT4-based simulation code has been developed by the INO collaboration for the ICAL simulations.

The muon momentum and charge are reconstructed using a Kalman Filter derived algorithm in the ICAL reconstruction code. For the analysis in this thesis, the muon response of the ICAL is parametrized in terms of its energy resolution, direction resolution, reconstruction efficiency and charge-identification efficiency. A muon response look-up table has been prepared for usage in the physics analysis. With certain assumptions about the muon reconstruction, it is found that at 5 GeV, the average muon energy resolution is about 12%. The average $\cos\theta_\mu$ resolution is 0.01. (θ_μ resolution is less than 1°.) The average efficiencies of muon reconstruction and charge identification are found to be 80% and 99% at this energy.

The muon reconstruction degrades when it passes a significantly long path in the dead spaces such as the support structures, RPC gaps and the magnet coils. Partially contained events also contribute to degraded energy resolutions and low efficiency. Also, the muons which are travelling at grazing angles with respect to the iron plates ($|\cos\theta_\mu| <0.25$) cannot be reconstructed well due to low number of hits. The optimal muon reconstruction happens in the range 5–8 GeV, which is an important region for the mass hierarchy determination.

Chapter 4

Atmospheric Neutrino Oscillation Analysis

The ICAL experiment will study oscillation physics in the atmospheric neutrino section. In this chapter, we briefly describe the neutrino fluxes, cross sections and the neutrino event generator NUANCE. We then outline the analysis procedure to simulate the data, including event generation, incorporation of the oscillation effects, and folding in the ICAL muon response. The treatment of systematic errors and the χ^2 analysis are described finally.

4.1 Atmospheric Neutrino Flux

The earth's atmosphere is constantly being bombarded by high energy cosmic rays. The primary cosmic rays mainly consists of protons, with a small fraction of Helium nuclei and heavy ions. When the cosmic rays interact with nuclei in the earth's atmosphere, they produce pions, kaons and other particles. The charged pions decay into neutrinos (Fig. 4.1) through the following decay chain for π^+,

$$\pi^+ \;\;\rightarrow\;\; \mu^+ + \nu_\mu, \tag{4.1}$$

$$\mu^+ \;\;\rightarrow\;\; e^+ + \overline{\nu}_\mu + \nu_e, \tag{4.2}$$

$$\tag{4.3}$$
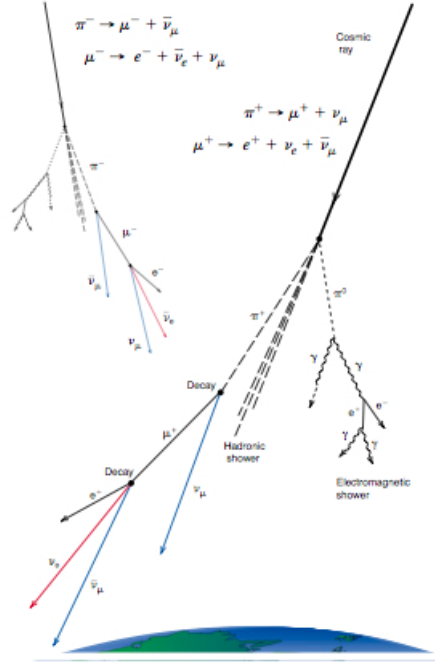
Figure 4.1: Generation of atmospheric neutrinos

and for π^-,

$$\pi^- \quad \rightarrow \quad \mu^- + \bar{\nu}_\mu, \tag{4.4}$$

$$\mu^- \quad \rightarrow \quad e^- + \nu_\mu + \bar{\nu}_e. \tag{4.5}$$

These neutrinos are known as the atmospheric neutrinos. At low energies (E < 1 GeV), where the muons decay before reaching the ground, the ratio of muon neutrinos to the electron neutrinos is 2:1, as seen from the above reactions. At higher energies, this ratio increases because not all muons decay before reaching the ground. The primary cosmic rays are modulated with the 11 year solar cycle and so are the atmospheric neutrino fluxes. The average height of neutrino production is 15 km above the mean sea level.

A three dimensional analytic calculation of the atmospheric neutrino flux can be found in [89]. More detailed predictions are obtained by carrying out complicated Monte Carlo simulations. Various groups [90, 91, 92] provide such predictions. The difference in the predictions from these group are due to different modelling of the

hadron shower models in the primary cosmic ray interaction.
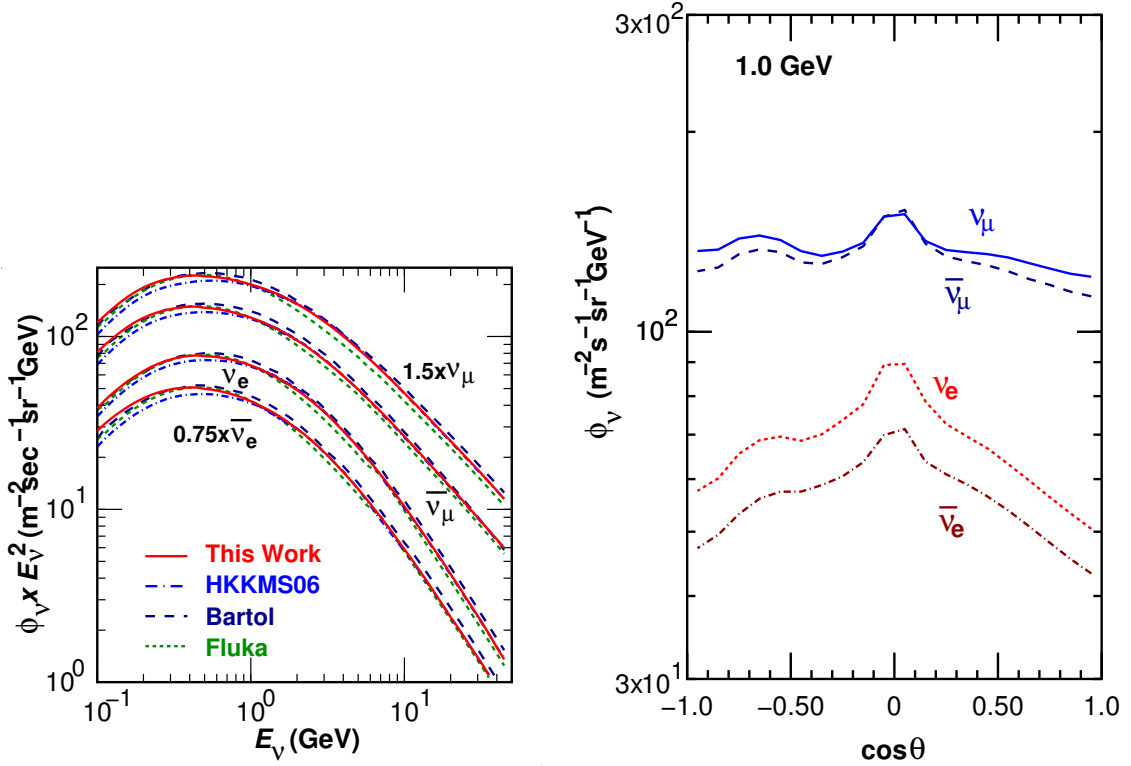
(a) Averaged over all zenith angles and azimuthal (b) Averaged over the azimuthal angle at 1 GeV
angles

Figure 4.2: Atmospheric neutrino flux at Tamika location predicted by the HONDA et. al. Figure adopted from [90].

Fig. 4.2 shows the flux prediction (HONDA et. al.) at the SK location. In the work presented in this thesis, the HONDA flux at the SK location has been used. The atmospheric neutrino flux peaks around 800 MeV, sharply falling afterwards. It is highly symmetric in the zenith angle and the azimuthal angle. Due to geomagnetic field variations over the earth, the primary cosmic ray spectrum at different locations are different. This results in the variation of the neutrino flux at different locations. Fig. 4.3 shows the preliminary flux as calculated for Theni. The flux at Theni is lower than the flux at Kamioka for lower neutrino energy. It is also asymmetric in the azimuthal angle at Theni. However, this will not affect the major physics goals for the ICAL significantly as the main region of interest is above 4 GeV.
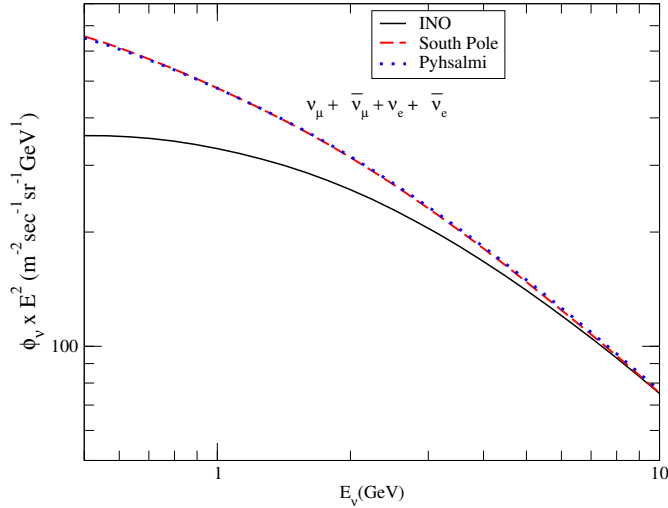
Figure 4.3: Comparison of neutrino flux at INO and SK sites. The flux is averaged over all zenith and azimuthal angles and summed over all neutrino flavors. [93]

4.2   Neutrino Interactions

The neutrinos passing through the ICAL can interact with the constituent nuclei through Charged Current(CC) or Neutral Current(NC) interaction processes. Additionally, the interactions can be classified in terms of final state particles produced and on the scattering kinematics. e.g. quasi-elastic (QE), resonance (RS), deep inelastic (DIS), coherent (CO) and diffractive (DF). Fig. 4.4 shows the NUANCE prediction for the neutrino cross sections for these processes as a function of energy [94]. The quasi-elastic process dominates at low energies. At intermediate energies, the resonance processes become important, where one or more pions and other mesons may be produced. At still higher energy, the deep inelastic process takes over. Resonance cross sections have not been understood well so far and they have large uncertainties in the prediction. This region is important for the ICAL experiment and more measurements on the iron target will be required to control the cross section systematics. The cross sections for anti-neutrinos are approximately one third of the corresponding neutrino cross sections due to the requirement of the angular momentum conservation in the interaction. Some of the reviews on neutrino cross section can be found in [94, 95, 96].
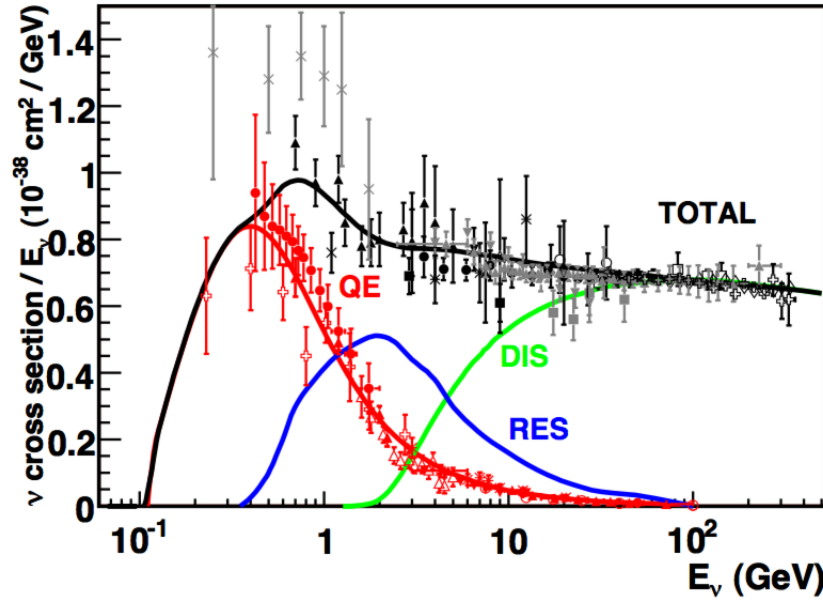
Figure 4.4: Neutrino-nucleon cross section prediction from NUANCE [94] and comparison with data

4.3 The NUANCE event generator

To simulate the neutrino-nucleon interactions in the ICAL detector, we use the neutrino event generator NUANCE (version 3.5) [97]. It incorporates the differential cross section calculations for charged current and neutral current interactions for all nuclear constituents of the materials used in the detector, for all neutrino flavors, and for all possible interaction processes. Additionally, it contains the models of particle transport in the nuclei and the hadronization models, which depict how the particles produced in the primary neutrino interactions emerge as final state particles for an experiment to observe. The event kinematics are generated based on the differential cross sections.

A simplified geometry of the ICAL detector is specified to NUANCE[1]. Given the detector constituent nuclei, NUANCE calculates the cross sections for all the proccesses specified in the input. NUANCE can use neutrino fluxes for the atmospheric neutrinos, accelerator beam, nucleon decay and supernova neutrinos. For this work, we have used the atmospheric neutrino fluxes provided by HONDA et al. [90]

---

[1]Since NUANCE was originally created for the SK simulations and has not been updated recently, it cannot accept the full ICAL detector geometry.

at Kamioka location. The exposure can be specified in terms of number of events or years. If the exposure is specified as number of years, NUANCE introduces statistical fluctuations in the generated number of events. The output of NUANCE consists of the interaction vertex position and the 4-momentum (p^μ) of the initial, intermediate and the final state particles for each event. This information is equivalent to the true energy and direction of all particles.

4.4 Choice of Observables

While the atmospheric neutrinos provide a natural source with broad ranges of energies and baselines, they also pose a challenge in the measurement of the same. Experimentally, it is difficult to reconstruct both the neutrino energy and direction accurately. In comparison, the energy and direction of the outgoing leptons produced in interactions can be measured easily. Therefore, in this analysis, we have adopted the muon energy and direction ($E_\mu, \cos\theta_\mu$) as the observables.

The distribution of the outgoing muon produced in a CC ν_μ interaction can be obtained as :

$$\frac{d^2 N_\mu}{dE_\mu \, d(\cos\theta_\mu)} = N \int_0^\infty dE_\nu \int_{-1}^1 d(\cos\theta_\nu) \frac{d^2 \Phi_\nu}{dE_\nu \, d(\cos\theta_\nu)} P_{\mu\mu}(E_\nu, \cos\theta_\nu) \frac{d^2 \sigma(\nu_\mu N \to \mu^- X)}{dE_\mu \, d(\cos\theta_\mu)},$$
$$(4.6)$$

where N is the exposure. The first term in the integrand represents the differential flux. The second term is the ν_μ survival probability and the third term is the differential cross section. In this equation, we have considered only the $\nu_\mu \to \nu_\mu$ disappearance channel. An analogous expressions can be written for the $\nu_e \to \nu_\mu$ channel.

We can obtain the true distribution of muons in ($E_\mu, \cos\theta_\mu$) from Eqn. 4.6. While it is straight forward to obtain the muon distribution from this equation, it has to be done for all possible interaction processes and neutrino flavors. The number of such combinations is 600. Instead of calculating the event distributions manually for all 600 interaction channels, in this analysis, we equivalently use NUANCE to obtain ($E_\mu, \cos\theta_\mu$) distribution, as explained in the next section. The use of NUANCE offers the additional benefit that the hadronization models and final state interactions in a

neutrino interaction are taken into account by NUANCE, which are not reflected in Eqn. 4.6.

4.5 Oscillation Analysis Procedure

The physics analysis of atmospheric neutrino events requires simulations which can be broadly classified into four steps : (i) Event Generation, (ii) inclusion of the oscillation effects, (iii) folding in the detector response, and (iv) the χ^2 analysis. By the end of step (iii), we obtain the measured distribution of muons, which contains the signature of the oscillation parameters and the mass hierarchy. The task of the χ^2 analysis in (iv) then, is to extract the oscillation parameters from this distribution. A ROOT-based [105] package in C++ has been developed for the oscillation analysis.

4.5.1 Event Generation

As the ICAL detector doesn't yet exist, we need to simulate an "Observed data" set which we expect to observe in the actual experiment. We use NUANCE to simulate this "Observed data", for a specified period of time. The total number of ν_μ events coming from the $\nu_\mu \to \nu_\mu$ and the $\nu_e \to \nu_\mu$ channels is given as,

$$\frac{d^2N}{dE_\nu d(\cos\theta_\nu)} = N_T \times N_D \times \sigma_{\nu_\mu} \times \left[P_{\mu\mu} \frac{d^2\Phi_{\nu_\mu}}{dE_\nu d(\cos\theta_\nu)} + P_{e\mu} \frac{d^2\Phi_{\nu_e}}{dE_\nu d(\cos\theta_\nu)} \right] , \quad (4.7)$$

where N_T is the exposure time and N_D is the number of targets in the detector. Here Φ_{ν_μ} and Φ_{ν_e} are the fluxes of ν_μ and ν_e respectively, and $P_{\alpha\beta}$ is the $\nu_\alpha \to \nu_\beta$ oscillation probability. The number of muon events can be found from Eqn. 4.6.

The real experimental data set will contain statistical fluctuations around the exact event rate obtained from Eqn. 4.6 and 4.7. A realistic physics analysis may be carried out by taking a large ensemble of such simulated "Observed data" sets with statistical fluctuations in the number of events and use them to carry out the χ^2 analysis [98, 99, 100, 101]. However, in this first analysis for the ICAL physics

simulations, we work with the "Asimov" data set, which gives median sensitivities [102].

We obtain the "Asimov" data set by reducing the statistical fluctuations in the number of events introduced by NUANCE. This is achieved by generating a very large number of neutrino interactions (for an exposure of 50 kt $\times$ 1000 years) and then scaling them down to the desired exposure for the χ^2 analysis. Generating such a large data set repeatedly, using oscillated flux with different set of oscillation parameters is extremely time consuming and computationally impractical for the χ^2 analysis. The remedy to this problem is the use of the "Re-Weighting" algorithm, as explained in Section 4.5.2.

4.5.2 Inclusion of Oscillations

The "Re-Weighting" algorithm is based on the MC accept-reject algorithm. In this method, we need to generate the event set only once and then we can obtain the distribution of oscillated events for any given set of oscillation parameters. Using NUANCE, we generate ν_μ events for the $\nu_\mu \to \nu_\mu$ channel assuming no oscillations. For the $\nu_e \to \nu_\mu$ channel, ν_μ are generated assuming that all ν_e got oscillated into ν_μ. These neutrinos are generated in the energy range $0.5 - 100$ GeV.
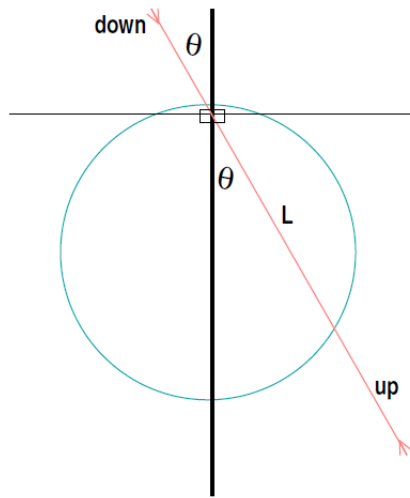
Figure 4.5: Geometry of neutrino path length

Fig. 4.5 shows the geometry of the path length L travelled by the atmospheric

neutrino. For a given $\cos \theta_\nu$, the path travelled between the production point and the detector is

$$L = \sqrt{(R + L_0)^2 - (R \sin \theta_\nu)^2} - R \cos \theta_\nu \,, \tag{4.8}$$

where R is the radius of the earth (6378 Km) and L_0 is the average height of the atmospheric neutrino production, taken here to be 15 km.

For an un-oscillated ν_μ coming from the $\nu_\mu \rightarrow \nu_\mu$ channel, we calculate its survival oscillation probability $P_{\mu\mu}(L, E)$. Here, E and L (or equivalently $\cos \theta_\nu$) are obtained from the NUANCE output for each event. Probability $P_{\mu\mu}$ is calculated using the oscillation probability code included in NUANCE [97]. The three flavor probability is calculated by considering neutrino propagation in the earth with the PREM density profile [103]. The details of this oscillation probability calculation are described in [104]. We next impose the event Re-Weighting algorithm as follows. To decide whether an un-oscillated ν_μ event survives the oscillations to be detected as a ν_μ, a uniform random number r is generated between 0 and 1. If $P_{\mu e} \leq r < P_{\mu e} + P_{\mu\mu}$, we keep this event as a ν_μ event. Otherwise this ν_μ is considered to have oscillated into a different flavor. When $P_{\mu e} + P_{\mu\mu} < r$, this is equivalent to $\nu_\mu \rightarrow \nu_\tau$ oscillation. When a ν_τ from this appearance channel interacts, it produces a τ^-, which decays into a μ^- with 17% branching ratio. In the current analysis, we neglect the tau induced muons. However, in a more realistic analysis, they need to be taken into account.

Analogously, to decide which neutrinos are detected as ν_μ in the $\nu_e \rightarrow \nu_\mu$ channel, we fold-in the oscillation probability $P_{e\mu}$ as follows. We again use the event Re-Weighting algorithm, where, for each event a random number r is generated between 0 and 1. If $r < P_{e\mu}$ we label the event as a ν_μ event, otherwise we discard it.

At this point, we have the true distribution of the oscillated ν_μ events in the ICAL detector. We can bin the events in terms of any observable of our choice. In this thesis work, we consider $(E_\mu, \cos \theta_\mu)$ as observables. The ν_μ events from $\nu_\mu \rightarrow \nu_\mu$ as well as $\nu_e \rightarrow \nu_\mu$ oscillation channels are added to form the μ^- event sample. Similarly, we form the μ^+ event sample.

The muons are binned according to their energy(E_μ) and direction ($\cos \theta_\mu$). The muon energy range is taken to be E_μ = 0.5 - 15.5 GeV (300 bins) and the $\cos \theta_\mu$ range is -1 to $+1$ (20 bins). The energy range is determined by the muon detection

threshold of the ICAL, which is around 0.5 GeV. We keep track of μ^- and μ^+ events separately in the entire analysis. Now, we have the true distribution of muon energy (E_μ) and the cosine of the zenith angle ($\cos\theta_\mu$). The binning scheme mentioned above is the pre-smearing binning scheme, where we bin the true muon event distribution.

The effect of the Re-Weighting algorithm is illustrated in Fig. 4.6 for the energy bin 2 GeV $\leq E_\mu <$ 3 GeV. It can be seen that the symmetric zenith angle distribution is distorted due to the oscillation effects. To generate this plot, we have used the oscillation parameters given in Table 4.1 and take the exposure to be 50 kt $\times$ 10 years.

Parameter	$\sin^2 2\theta_{12}$	$\sin^2 2\theta_{23}$	$\sin^2 2\theta_{13}$	$\Delta m_{21}^2(\text{eV}^2)$	$|\Delta m_{32}^2|(\text{eV}^2)$	δ_{CP}	Hierarchy
True Value	0.86	1.0	0.113	7.6 $\times 10^{-5}$	2.424 $\times 10^{-3}$	0.0	Normal

Table 4.1: True values of the neutrino oscillation parameters used for the precision measurement analysis.
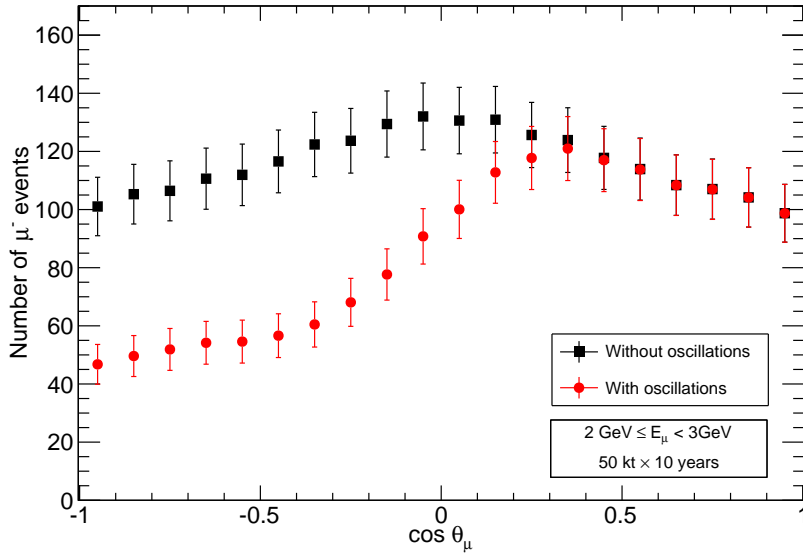
Figure 4.6: Zenith angle distribution of μ^- events for the bin 2 GeV $\leq E_\mu <$ 3 GeV, without and with flavor oscillations. The detector efficiencies have not been included here. The error bars shown here are statistical.

The Re-Weighting algorithm described above is an immensely useful method for the oscillation analysis involving muons. Without its application, one would have to

use the differential cross sections for all possible combinations of neutrino flavors, targets and interactions processes. Though straight forward, it is a cumbersome process considering the large number of possible combinations of the above quantities. Also, in the case of NUANCE event generation, it allows to use the same set of events for various sets of oscillation parameters. Generating a large set of NUANCE interactions is a computationally intensive task. The "Re-Weighting" algorithm requires the event generation only once and hence drastically reduces the computation requirements.

4.5.3 Folding in the Detector Response

Having incorporated the oscillation effects into the muon distribution, we next fold in the ICAL detector response to muons. As described in the Section 3.4.3, the ICAL muon response is parametrized in terms of the muon energy resolution, $\cos\theta_\mu$ resolution, the reconstruction efficiency and the charge identification efficiency. Two different methods have been explored to fold in the detector response : (i) using random numbers, and (ii) using the functional smearing.

In the random number method, we smear the true energy and direction of the muon by generating random numbers for these two quantities according to their resolution functions. The efficiencies are folded in using the MC accept-reject algorithm, similar to the one used to incorporate the oscillation effects. While this method resembles the reality more closely, it also brings in additional statistical fluctuations coming from the detector measurements. Since we want to work with the "Asimov" data set, we need to substantially dilute these fluctuations. Note that these fluctuations are in addition to the fluctuations in the number of events coming from the NUANCE data set. This requires us to work with an even larger data set than 1000 yr × 50 kt, significantly increasing the computing time. To avoid this problem, we use the functional smearing described in the rest of this analysis[2].

The functional smearing method to fold in the resolutions and efficiencies is completely deterministic. We first apply the reconstruction efficiency (ϵ_{R-}) for μ^- by multiplying the number of events in a given true energy (E_μ) and true zenith angle

---

[2]The random number smearing method will be useful when we study the ICAL physics sensitivities with the fluctuations in the "Observed" data set.

$(\cos\theta_\mu)$ bin with the corresponding reconstruction efficiency:

$$N_{\mu-}(E_\mu, \cos\theta_\mu) = \epsilon_{R-}(E_\mu, \cos\theta_\mu) \times N_{\mu-}^{\text{true}}(E_\mu, \cos\theta_\mu), \tag{4.9}$$

where $N_{\mu-}^{\text{true}}$ is the number of μ^- events in a given $(E_\mu,\ \cos\theta_\mu)$ bin. The same operation is carried out to obtain the number of μ^+ events. This equation simply scales down the number of events in various bins according to their reconstruction efficiencies.

Next, we mix the μ^- and μ^+ events in different bins according to their charge identification effciencies. The CID efficiency (ϵ_{C-} for μ^- and ϵ_{C+} for μ^+ event sample) is next applied as follows:

$$N_{\mu-}^C = \epsilon_{C-} \times N_{\mu-} + (1 - \epsilon_{C+}) \times N_{\mu+}, \tag{4.10}$$

where $N_{\mu-}$ and $N_{\mu+}$ are the number of μ^- and μ^+ events, respectively, given by Eqn. (4.9). Now, $N_{\mu-}^C$ is the number of μ^- events after taking care of the CID efficiency. All the quantities appearing in QE. (4.10) are functions of E_μ and $\cos\theta_\mu$.

(a) Zenith angle distribution   (b) Muon Energy spectrum
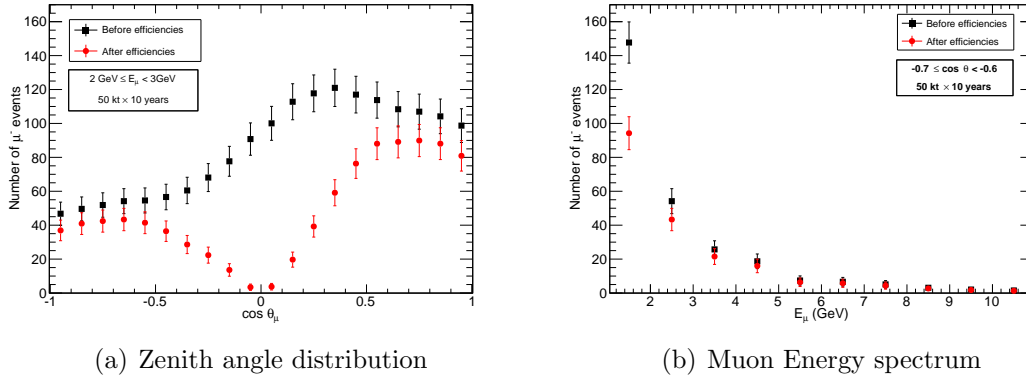
Figure 4.7: Muon event distribution of oscillated μ^- events. Panel (a) shows the zenith angle distribution for the bin 2 GeV $\leq E_\mu <$ 3 GeV, after taking into account detector efficiencies. Panel (b) shows the muon energy distribution for the bin -0.7 $\leq \cos\theta_\mu <$ -0.6. The error bars shown here are statistical.

Fig. 4.7(a) shows the zenith angle distribution of events obtained before and after applying the reconstruction and CID efficiencies in the bin 2 GeV $\leq E_\mu <$ 3 GeV.

Notice that the number of events fall sharply for bins around the horizontal direction, e.g. $\cos\theta_\mu \approx 0$. This can be understood by recalling that the horizontally travelling muons are difficult to reconstruct. The CID efficiency also falls for the more horizontal bins and the result is that there are hardly any events for bins with $-0.2 \leq \cos\theta_\mu < 0.2$. Fig. 4.7(b) shows the muon energy distribution for the same operation in the bin $-0.7 \leq \cos\theta_\mu < -0.6$. We notice that the number of muon events fall significantly at lower energy compared the at the high energy. This behaviour is consistent with the ICAL muon reconstruction efficiency in Fig. 3.9(c).

Finally, we fold in the muon resolutions σ_E and $\sigma_{\cos\theta}$ as follows:

$$(N_{\mu^-}^D)_{ij} = \sum_k \sum_l N_{\mu^-}^C(E_\mu^k, \cos\theta_\mu^l) \ K_i^k(E_\mu^k) \ M_j^l(\cos\theta_\mu^l) \,, \tag{4.11}$$

where $(N_{\mu^-}^D)_{ij}$ denotes the number of muon events in the ith E-bin and the jth $\cos\theta$-bin after applying the energy and angle resolutions. Here E and $\cos\theta$ are the measured muon energy and zenith angle. The summation is over the true energy bin k and true zenith angle bin l, with E_μ^k and $\cos\theta_\mu^l$ being the central values of the kth true muon energy and l^{th} true muon zenith angle bin. The quantities K_i^k and M_j^l are the integrals of the detector resolution functions over the bins of E and $\cos\theta$, the measured energy and direction of the muon, respectively. These are evaluated as:

$$K_i^k(E_\mu^k) = \int_{E_{L_i}}^{E_{H_i}} dE \frac{1}{\sqrt{2\pi}\sigma_{E_\mu^k}} \exp\left(-\frac{(E_\mu^k - E)^2}{2\sigma_{E_\mu^k}^2}\right) \,, \tag{4.12}$$

and

$$M_j^l(\cos\theta_\mu^l) = \int_{\cos\theta_{L_j}}^{\cos\theta_{H_j}} d\cos\theta \frac{1}{\sqrt{2\pi}\sigma_{\cos\theta_\mu^l}} \exp\left(-\frac{(\cos\theta_\mu^l - \cos\theta)^2}{2\sigma_{\cos\theta_\mu^l}^2}\right) \,, \tag{4.13}$$

where $\sigma_{E_\mu^k}$ and $\sigma_{\cos\theta_\mu^l}$ are the energy and zenith angle resolutions, respectively, in these bins. We perform the integrations between the lower and upper boundaries of the measured energy (E_{L_i} and E_{H_i}) and the measured zenith angle ($\cos\theta_{L_j}$ and $\cos\theta_{H_j}$). For the extreme $\cos\theta$ bins, the bins are taken to be $(-\infty, -0.9)$ and $[0.9, +\infty)$ while integrating, and the events are assigned to the bins $[-1, -0.9]$ and $[0.9, 1]$, respectively. These integral limits take care of the event pile up at the end points. At low energies, $E_\mu^k < 1$ GeV, the integrand in Eqn. (4.12) is replaced with the Landau

distribution function, as the reconstructed energy distribution obtained from ICAL simulations is specified in terms of this function.

(a) Zenith angle distribution
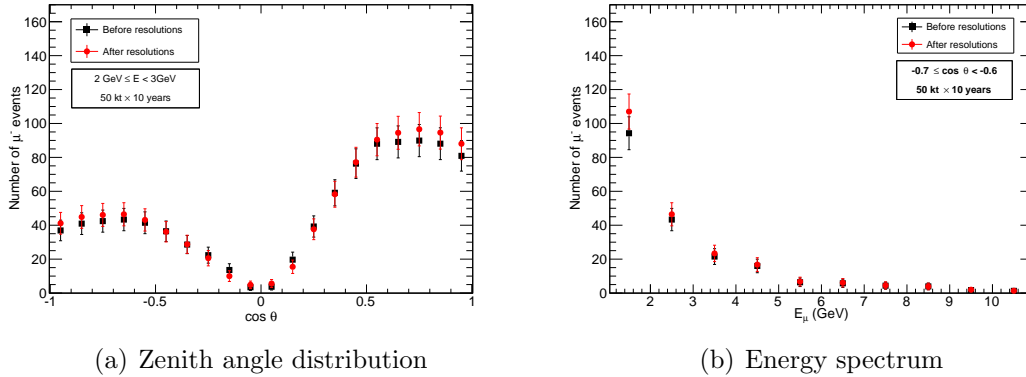
(b) Energy spectrum

Figure 4.8: Panel (a) shows the zenith angle distribution of μ^- events for the bin 2 GeV $\leq E_\mu <$ 3 GeV before and after including energy and zenith angle resolution function. Panel (b) shows the effect of same operation on the muon energy spectrum for the bin -0.7 $\leq \cos\theta_\mu <$ -0.6. Here E and θ are the measured energy and measured zenith angle, respectively. The error bars shown here are statistical.

Fig. 4.8(a) shows the zenith angle distribution of μ^- events before and after folding in the resolution functions. The angular dependence seems to get only slightly diluted. This is attributed to the good angular resolution of the detector. Fig. 4.8(b) shows the effect of resolution on the muon energy spectrum for the bin -0.7 $\leq \cos\theta_\mu <$ -0.6. Again, at low energy, where the muon energy resolution is relatively coarse ($\sim 22\%$), the effect of resolution is larger compared to the higher energies.

Table 4.2 shows the total number of muon events measured in the energy range 0.8-10.8 GeV at various stages of the analysis for an exposure of 50 kt $\times$ 10 years. Note the sharp fall in statistics due to the reconstruction efficiencies. The reconstruction efficiencies are particularly poor for the near-horizontal bins where the reconstruction of the muon tracks is very hard. The small increase in the number of events after applying the energy resolution function is due to the spill-over of events from the low-energy part of the spectrum to measured energies greater than 0.8 GeV. The spillover to the energy bins with $E_\mu >$10.8 GeV is comparatively small. The zenith angle resolution leaves the number of muon events nearly unchanged.

	μ^-	μ^+
Unoscillated	14311	5723
Oscillated	10531	4188
After Applying Reconstruction and CID Efficiencies	4941	2136
After Applying $(E, \cos\theta)$ Resolutions	5270	2278

Table 4.2: Number of muon events produced in CC ν_μ interactions at various stages of the analysis for an exposure of 50 kt $\times$ 10 years in the energy range 0.8-10.8 GeV.

4.5.4 The χ^2 Analysis

Typically, neutrino experiments deal with low count rates due to small interaction cross sections. Because of it, in the binned χ^2 analysis, many bins may not receive sufficient number of events. The common, Gaussian definition of χ^2 requires that each bin should contain at least 5 events [106]. Even for a moderately large size neutrino experiment, this requirement may not be satisfied for several bins. Therefore, we make use of the Poisson χ^2 definition in the oscillation analysis, which correctly takes care of the statistical errors in case of low counts.

We use the following definition of χ^2 :

$$\chi^2_{\text{ino}}(\mu^-) = \min_{\xi_k} \sum_{i=1}^{N_E} \sum_{j=1}^{N_{\cos\theta}} 2\left[(N_{ij}^{\text{pred}} - N_{ij}^{\text{obs}}) - N_{ij}^{\text{obs}} \ln\left(\frac{N_{ij}^{\text{pred}}}{N_{ij}^{\text{obs}}}\right)\right] + \sum_{k=1}^{5} \xi_k^2, \quad (4.14)$$

with

$$N_{ij}^{\text{pred}} = N_{ij}^0 \left(1 + \sum_{k=1}^{5} \pi_{ij}^k \xi_k\right). \quad (4.15)$$

Here, N_{ij}^{pred} and N_{ij}^{obs} are the expected and observed number, respectively, of μ^- events ($N_{\mu^-}^D$) in a given $(E, \cos\theta)$ bin. N_E and $N_{\cos\theta}$ are the number of measured energy and $\cos\theta_\mu$ bins, respectively. Their values are different for different analyses and will be mentioned in the relevant sections. In Eqn. 4.14, the standard Poisson χ^2 has been modified to include the systematic errors via the method of pulls [107]. The first term is the standard Poisson χ^2 and the second term represents the pull penalty contribution. The quantities π_{ij}^k and ξ_k appearing in Eqn. 4.15 are going to be explained in Section 4.5.5 along with the description of the systematic errors considered in this analysis.

N_{ij}^{obs} is obtained for a set of assumed "true value" of the oscillation parameters. N_{ij}^0 is the predicted number of events for a given set of oscillation parameters without considering the systematics. e.g. It is the measured distribution of muons as obtained in 4.5.3.

For each set of oscillation parameters, we calculate the χ^2 separately for the μ^- and μ^+ data samples, and add them to obtain the total χ^2 as

$$\chi_{\text{ino}}^2 = \chi_{\text{ino}}^2(\mu^-) + \chi_{\text{ino}}^2(\mu^+). \tag{4.16}$$

4.5.5 Systematic Errors

The systematic uncertainties are included via the "pull" variables ξ_k, one each for every systematic uncertainty σ_k. In Eqn. 4.15, π_{ij}^k is the change in the number of events in the $(ij)^{\text{th}}$ bin caused by varying the value of kth pull variable ξ_k by σ_k. For determining π_{ij}^k, we have used a procedure similar to the one described in [107].

In this analysis we have considered the following five systematic uncertainties [3].

1. Flux normalization error 20%

2. Cross section error, 10%

3. Overall 5% systematic on the number of events

4. Tilt error 5% (error in neutrino energy spectrum)

5. Zenith angle error 5%

Even though the aforementioned errors are specified for neutrinos, we calculate π_{ij}^k from the number of muon events. The errors are propagated from neutrinos to muons through NUANCE generated event distribution. The first three systematics are energy-angle independent errors and the corresponding π_{ij}^k simply becomes σ_k. Here σ_k is the percentage error mentioned above. The coefficients for the tilt error are energy dependent and are obtained using the following method [107]. The event

---

[3]More experimental systematics will be included in future.

spectrum is calculated with the predicted atmospheric neutrino fluxes and then with the flux spectrum shifted according to

$$\Phi_\delta(E) = \Phi_0(E) \left(\frac{E}{E_0} \right)^\delta \simeq \Phi_0(E) \left(1 + \delta \ln \frac{E}{E_0} \right) , \qquad (4.17)$$

where $E_0 = 2$ GeV and δ is the 1σ systematic tilt error, taken to be 5%. Then the corresponding π_{ij}^4 is obtained as,

$$\pi_{ij}^4 = \frac{N_{ij}^{\text{Tilted}} - N_{ij}^{\text{Nominal}}}{N_{ij}^{\text{Nominal}}}. \qquad (4.18)$$

Here N_{ij}^{Tilted} and N_{ij}^{Nominal} are the event distributions generated using the tilted and the nominal fluxes, respectively. Finally, the zenith angle error coefficient is obtained as,

$$\pi_{ij}^5 = \sigma_5 \times < \cos \theta_\mu >_{ij}, \qquad (4.19)$$

where $< \cos \theta_\mu >_{ij}$ is the central values of the $(ij)^{\text{th}} \cos \theta_\mu$ bin.

4.5.6 χ_{ino}^2 Minimization Method

χ_{ino}^2 defined in Eqn. 4.14 is to be minimized with respect to all five pull variables and three oscillation parameters of interest. Since this χ_{ino}^2 is constructed from the MC simulations, it is difficult to minimize it with the standard numerical techniques with respect to 8 parameters simultaneously. Therefore, we adopt a semi-analytic approach. We first minimize the χ_{ino}^2 in Eqn. 4.14 by taking its derivative with respect to ξ_k.

$$\frac{\partial \chi_{\text{ino}}^2}{\partial \xi_l} = 0 \qquad (4.20)$$

After some algebra and keeping only the linear terms in ξ_l, we obtain,

$$\Sigma_{i,j} \pi_{ij}^l \left(N_{ij}^p - N_{ij}^o \right) + \Sigma_k \left(\Sigma_{i,j} N_{ij}^o \pi_{ij}^k \pi_{ij}^l \right) + \xi_l = 0. \qquad (4.21)$$

Here the summation over indices indicate the summation of the E_μ and $\cos \theta_\mu$

terms for brevity. We have five simultaneous linear equations in ξ_l, which are easily solvable using the standard techniques. The solution minimizes the χ^2_{ino} with respect to the pull variables. χ^2_{ino} is next minimized with respect to the relevant oscillation parameters by using a grid sampling method depending on the physics sensitivities to be studied.

4.6   Chapter Summary

The ICAL will study oscillations in the neutrinos produced in the interaction of the cosmic rays with the nuclei in the Earth's atmosphere. We use the event genera-tor NUANCE to simulate the neutrino-nucleon interactions in the ICAL detector using un-oscillated neutrino fluxes. The oscillation effects are incorporated in the generated "unoscillated" events using the "Re-Weighting" algorithm, which is based on MC accept-reject algorithm. The ICAL detector resolutions and efficiencies are then folded in to obtain the measured distribution of muon $(E_\mu, \cos\theta_\mu)$. The physics sensitivities presented in this thesis are obtained using the "Asimov" data set. We incorporate 5 systematic errors in the χ^2 analysis via the method of pulls. χ^2_{ino} is minimized with respect to the pull variables and oscillation parameters to obtain the physics sensitivities.

Chapter 5

Neutrino Mass Hierarchy Determination with ICAL

Determination of the neutrino mass hierarchy is currently one of the outstanding problems in neutrino physics. With the recent discovery of a non-zero and relatively large θ_{13} value, many experiments have taken up this issue [108]. Currently, two different approaches are under consideration for determining the mass hierarchy. The first approach exploits the earth matter effects, as neutrinos travel long distances in the Earth. This approach is taken up by the accelerator experiments such as NOνA [55, 56, 57], LBNE [58], and LBNO[59] with long baselines of about 1000 - 2000 km. The atmospheric neutrino experiments like the ICAL and PINGU[62] will also use the matter effect approach to determine the mass hierarchy. The second approach is to make very accurate measurement of neutrino oscillation pattern over a medium baseline of 50 – 60 km in reactor neutrino disappearance [109]. This is the approach taken up by JUNO [66, 110] and RENO-50 [67].

(a) L = 7000 km, ν_μ

(b) L = 9000 km, ν_μ
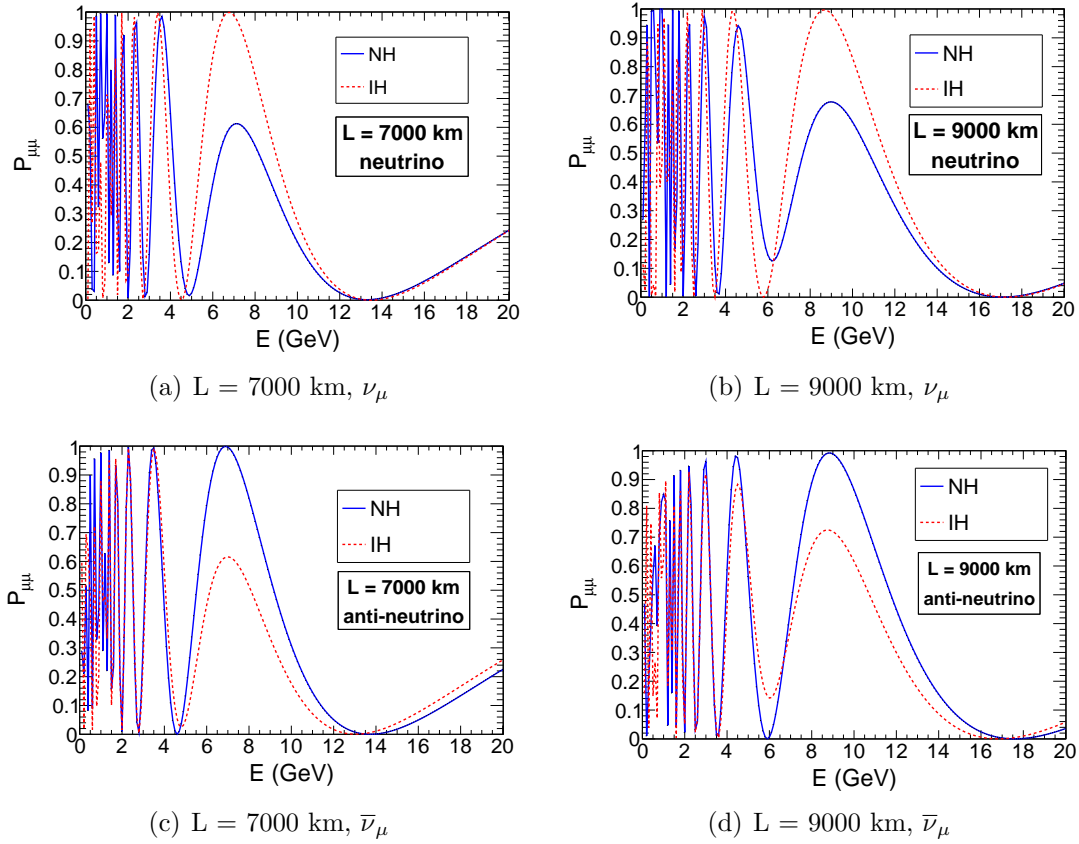
(c) L = 7000 km, $\overline{\nu}_\mu$

(d) L = 9000 km, $\overline{\nu}_\mu$

Figure 5.1: $P_{\mu\mu}$ for NH and IH for baselines of 7000 km and 9000 km. The top panels are for neutrinos and the bottom panels for anti-neutrinos. It can be seen that due to the matter effects, $P_{\mu\mu}$ is suppressed for NH for the neutrinos. In the case of anti-neutrinos, $P_{\mu\mu}$ is suppressed for IH.

5.1 Mass Hierarchy Determination with Atmospheric Neutrinos

The problem of the neutrino mass hierarchy determination with atmospheric neutrinos has been explored extensively over the past few years [111]-[130]. As discussed in Section 1.3, the neutrino passing though matter can undergo MSW resonance and can give rise to different oscillation probabilities for neutrinos and anti-neutrinos. For the atmospheric neutrino ν_μ disappearance experiment, the matter effects in $P_{\mu\mu}$ arise from the $P_{\mu e}$ and $P_{\mu\tau}$ components. The resonance condition occurs for the oscillation

parameter θ_{13}:

$$\tan\theta_{13}^m = \frac{\Delta m_{31}^2 \sin 2\theta_{13}}{\Delta m_{31}^2 \cos 2\theta_{13} \pm 2\sqrt{2}G_F n_e E}. \tag{5.1}$$

In the above equation, the positive sign is for the neutrinos and the negative sign for the anti-neutrinos, and n_e is the electron density of the material. As the neutrinos pass through the core and the mantle regions of the earth, the above resonance condition can be satisfied depending on the energy and the zenith angle, and $P_{\mu\mu}$ can substantially differ from the vacuum probability. This is illustrated in Fig. 5.1 for two different baselines of 7000 km and 9000 km. It can be seen in Fig. 5.1(a) and Fig. 5.1(b) that due to the MSW resonance, $P_{\mu\mu}$ is suppressed for neutrinos in the case for the normal hierarchy, while there is no effect for the anti-neutrinos. Whereas, in the case of the inverted hierarchy, the $P_{\mu\mu}$ is suppressed for the anti-neutrinos, as can seen from Fig. 5.1(c) and Fig. 5.1(d). This is the central idea for the MH determination in the long baseline experiments.

It has been shown in [131] that a magnetized detector with fine resolution is a good choice to determine the mass hierarchy. In the case of the atmospheric neutrinos, the neutrino energy range of 5–10 GeV and baselines of 7000–11,000 km correspond to the regions from where the highest MH sensitivity can be achieved. By measuring the event rates for μ^- and μ^+, the mass hierarchy may be determined. The large difference seen in Fig. 5.3 in $P_{\mu\mu}$ for NH and IH can significantly be diluted when the detector resolutions and the efficiencies are folded in. The ICAL experiment has an average energy resolution of 10% in the muon energy range of 5–10 GeV and the $\cos\theta_\mu$ resolution of 2%. The CID efficiency of the ICAL gives it an extra advantage, where the event rates for μ^- and μ^+ can be determined separately. Without the CID capability, a large event statistics is required to determine the MH. This is the case with PINGU [62, 132], ORCA [63], HK [64] and T2HK [65], all of which are megaton class detectors.

5.2   Details of the Analysis

The mass hierarchy is defined as Normal if $\Delta m_{31}^2 > 0$. If $\Delta m_{31}^2 < 0$ then the hierarchy is defined as Inverted. However, the magnitude of Δm_{31}^2 is different for NH ($|\Delta m_{32}^2| +$

$|\Delta m_{21}^2|$) and for IH ($|\Delta m_{32}^2| - |\Delta m_{21}^2|$), which leads to differences in the oscillation frequencies. The atmospheric mass squared difference that is measured in the $\nu_\mu \to \nu_\mu$ disappearance channel [133] is given by,

$$\Delta m_{\text{eff}}^2 = \Delta m_{31}^2 - (\cos^2 \theta_{12} - \cos \delta_{\text{CP}} \sin \theta_{13} \sin 2\theta_{12} \tan \theta_{23})\Delta m_{21}^2 . \qquad (5.2)$$

We define the mass hierarchy to be normal if $\Delta m_{\text{eff}}^2 > 0$ and inverted if $\Delta m_{\text{eff}}^2 < 0$. With this definition of the MH, the oscillation frequencies remain the same for both NH and IH.

ICAL can rule out the wrong mass hierarchy with a significance of $n\sigma$, where $n = \sqrt{\Delta\chi_{\text{ino}}^2}$, and

$$\Delta\chi_{\text{ino}}^2 = \chi_{\text{ino}}^2(\text{false}) - \chi_{\text{ino}}^2(\text{true}). \qquad (5.3)$$

Here, $\chi_{\text{ino}}^2(\text{true})$ is calculated by fitting the true mass hierarchy to the observed data set and $\chi_{\text{ino}}^2(\text{false})$ is calculated by fitting the wrong mass hierarchy to the observed data set. We use χ_{ino}^2 defined in Eqn. 4.16. The significance of ruling out the wrong mass hierarchy is $n\sigma$, with $n = \sqrt{\Delta\chi_{\text{ino}}^2}$.

Parameter	True Value	Marginalization Range
$\sin^2 2\theta_{12}$	0.86	
$\sin^2 \theta_{23}$	0.4,0.5,0.6	$\sin^2 \theta_{23}(\text{true}) \pm 0.1$
$\sin^2 2\theta_{13}$	0.08,0.10,0.12	$\sin^2 2\theta_{13}(\text{true}) \pm 0.03$
$\Delta m_{21}^2 (\text{eV}^2)$	7.5×10^{-5}	
$\Delta m_{\text{eff}}^2 (\text{eV}^2)$	2.4×10^{-3}	$[2.1 - 2.6] \times 10^{-3}$
δ_{CP}	$0°$	$[0 - 360] °$

Table 5.1: True values of oscillation parameters used for the mass hierarchy analysis.

For the χ^2 analysis of ICAL, we have used N_E=20 (in the range $E_\mu = [1,11]$ GeV) energy bins and $N_{\cos\theta}$=80 (in the range $\cos\theta_\mu = [-1,1]$) $\cos\theta_\mu$ bins in Eqn. 4.14, for all the results presented here. These numbers have been chosen after performing a binning optimization, as described in Section 5.3. The true values of oscillation parameters with which N^{obs} is simulated for the MH analysis are mentioned in Table 5.1.

Fig. 5.2 shows the zenith angle distribution of μ^- events for NH and IH. Panel (a)
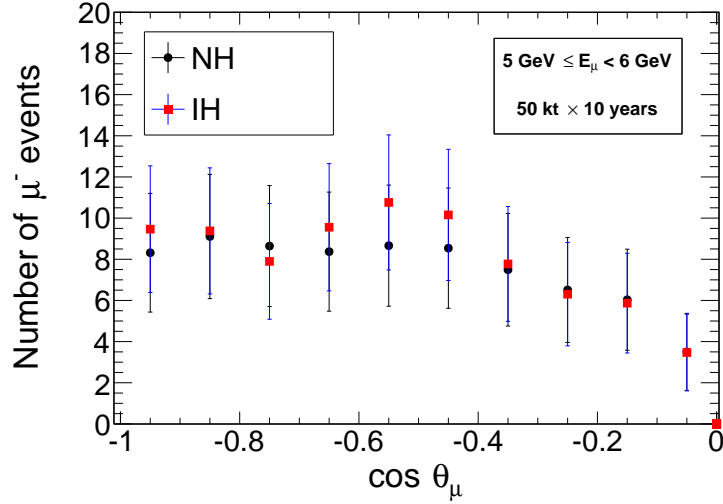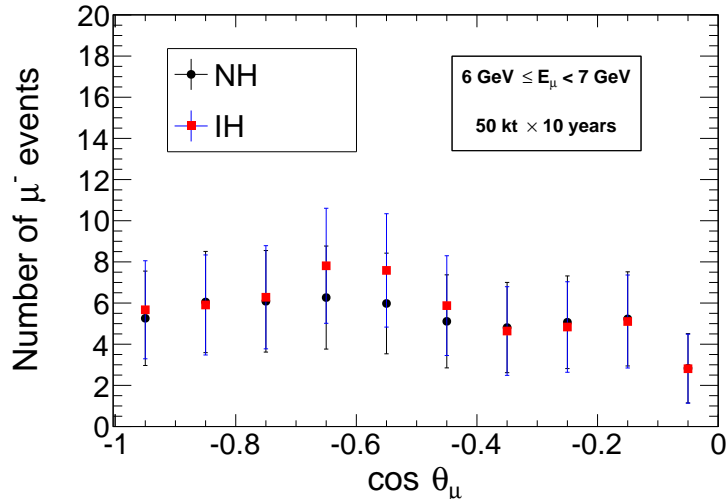
(a) E_μ = 5-6 GeV

(b) E_μ = 6-7 GeV

Figure 5.2: Comparison of μ^- zenith angle distributions for NH and IH, for the muon energy bin (a) 5–6 GeV, and (b) 6–7 GeV. An exposure of 50 kt × 10 years and the central values of the benchmark oscillation parameters have been used. The ICAL detector response has been folded in to obtain the event distributions.

is for the muon energy bin 5-6 GeV, while panel (b) is for the muon energy bin 6-7 GeV. It can be seen that the number of μ^- events are suppressed for the NH due to the matter effects around $\cos\theta_\mu =$ -0.5. There is no suppression of μ^- events in case of IH. The opposite scenario happens for the μ^+ events. e.g. There is a suppression of μ^+ events if the hierarchy is IH and there is no suppression if the hierarchy is NH. This figure illustrates why the charge identification capability is important for ICAL. Even though the difference in $P_{\mu\mu}$ is large for NH and IH at the probability level (Fig. 5.1), we notice here that after folding in the detector response, the difference in the number of events is small.

Fig. 5.3 shows the distribution of χ^2 in the plane $E_\mu - \cos\theta_\mu$. Notice that the major contribution to $\Delta\chi^2$ comes from the region spanning $E_\mu \sim$ 5-8 GeV and muon $\cos\theta_\mu \sim$ (-0.4) – (-0.8). The neutrino mass hierarchy sensitivity arises in the energy range 5–8 GeV. At these neutrino energies, the outgoing muon travels along almost the same direction as the neutrino. Hence the neutrino and muon energy-angle region from where the maximum hierarchy sensitivity arises, due to the difference in the NH and IH event rates is consistent. The difference in the χ^2 distribution for μ^- and μ^+ comes due to different event statistics and scattering kinematics.

5.3   Binning Optimization

For the analysis of the real ICAL data, one would like to perform an unbinned likelihood analysis to extract maximum information on the oscillation parameters. However, in the current work, we are performing a binned analysis of the simulated data. The neutrino oscillation probability vary rapidly as functions of neutrino energy and zenith angle and consequently in the muon energy/zenith angle. As a rule of thumb, the bin width should be of the order of the width of the resolution function for the concerned bin. Taking wider bins can wash out these rapid features in the $(E_\mu, \cos\theta_\mu)$ distribution, diluting the mass hierarchy sensitivity. Whereas using too fine binning may result in bin-to-bin correlation of the data as well as insufficient statistics for several bins.

Fig. 5.4 show the ICAL mass hierarchy $\Delta\chi^2$ as a function of number of E_μ and $\cos\theta_\mu$ bins. Here we use the fixed parameter χ^2 to avoid the complication of marginal-
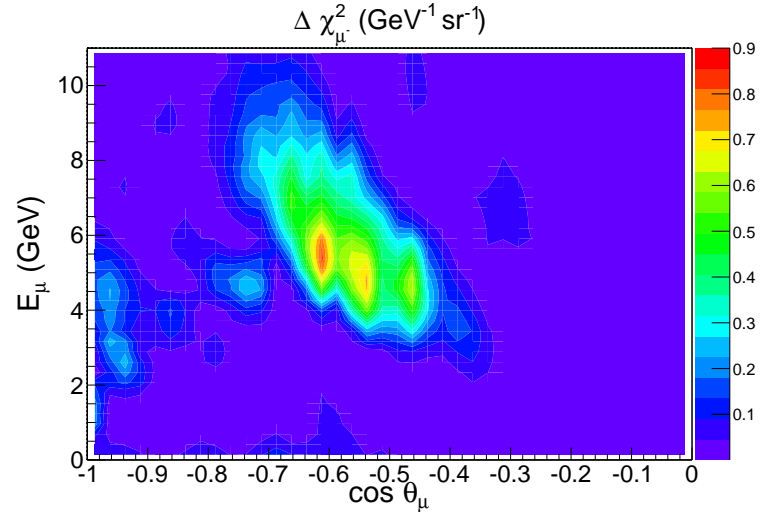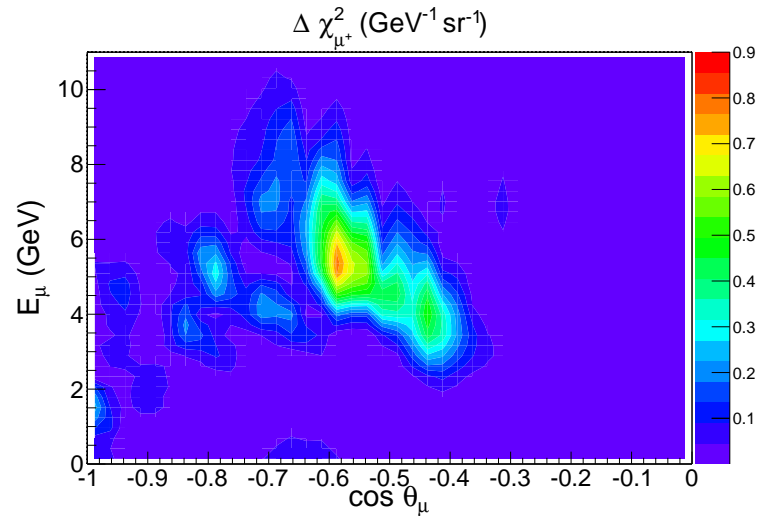
(a) $\Delta\chi^2(\mu^-)$

(b) $\Delta\chi^2(\mu^+)$

Figure 5.3: χ^2 distribution in the plane $E_\mu - \cos\theta_\mu$, for (a) μ^-, and (b) μ^+. An exposure of 50 kt $\times$ 10 years and the central values of the benchmark oscillation parameters have been used.
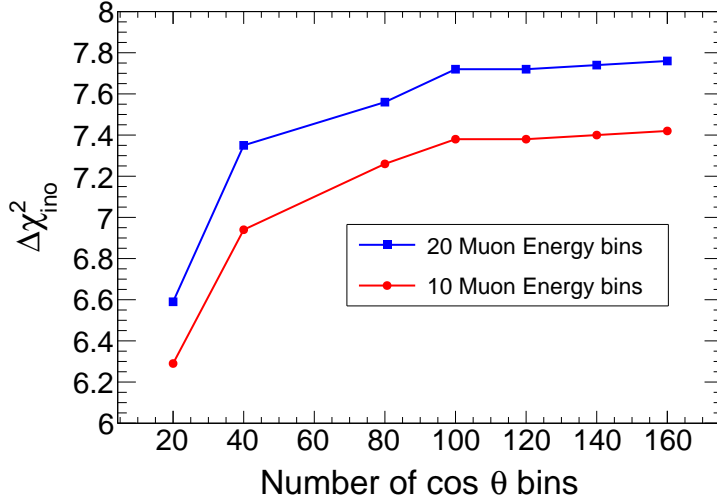
Figure 5.4: Fixed parameter χ^2 as a function of number of E_μ and $\cos\theta_\mu$ bins. An exposure of 50 kt $\times$ 10 years and the central values of the benchmark oscillation parameters have been used.

ization, which is irrelevant for the binning optimization studies. While generating this plot, we have used the central values of the benchmark oscillation parameters and considered an exposure of 50 kt $\times$ 10 years. It can be seen that χ^2 rises rapidly while going from 20 to 100 $\cos\theta_\mu$ bins, before getting saturated. It also rises while going from 10 to 20 E_μ bins. We have checked that for 40 E_μ bins, there is no significant gain in χ^2. Using large number of bins results in higher computing time without giving a substantial improvement in the hierarchy sensitivity. Therefore, we have chosen to work with 20 E_μ bins and 80 $\cos\theta_\mu$ bins as an optimal choice. As noted in Section 3.4.3, the average ICAL muon energy and $\cos\theta$ resolutions are about 15% and 2%. These resolutions permit the binning scheme considered here.

5.4 Sensitivity for fixed oscillation parameters

Fig. 5.5 shows the mass hierarchy sensitivity for $\sin^2\theta_{23} = 0.5$ and for three different values of $\sin^2 2\theta_{13}$. It can be seen that for 10 years of ICAL operation, the wrong hierarchy can be ruled out at a significance of 2.7σ (2.7σ), for $\sin^2 2\theta_{13} = 0.1$, if the true hierarchy is normal (inverted). We find that χ^2_{ino} increases linearly with increasing exposure, as the hierarchy measurement is dominated by statistics. Also,
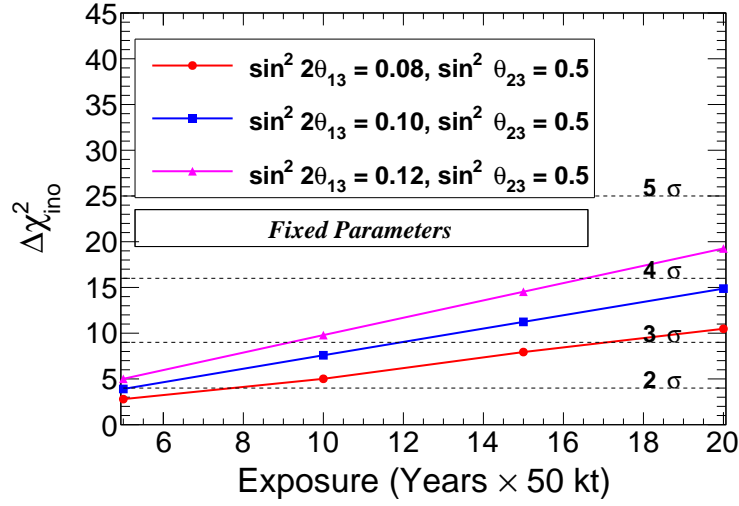
(a) True Hierarchy : Normal
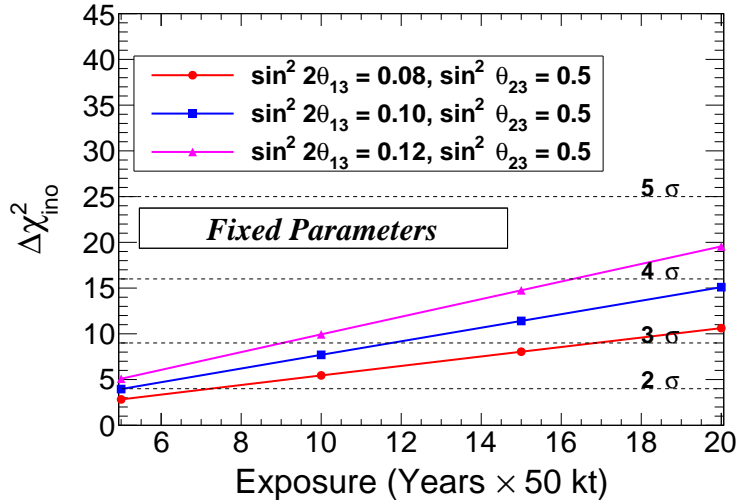
(b) True Hierarchy : Inverted

Figure 5.5: Mass hierarchy sensitivity for the fixed oscillation parameters, and $\sin^2 \theta_{23} = 0.5$

the MH discovery sensitivity is almost identical for the normal and inverted hierarchy. A larger value of θ_{13} enhances the sensitivity. This can be understood from the fact that the matter effects are enhanced for large θ_{13} and give rise to a larger difference in the μ^- and μ^+ event rates [134]. Larger θ_{23} values also enhance the MH discovery sensitivity due to enhanced matter effects [134]. Fig. 5.6 shows χ^2_{ino} for $\sin^2 \theta_{23} = 0.4$ and 0.6. With 10 years of ICAL exposure, 3.8σ hierarchy determination may be made if $\sin^2 2\theta_{13} = 0.12$ and $\sin^2 \theta_{23} = 0.6$. Depending upon the true values of $\sin^2 2\theta_{13}$ and $\sin^2 \theta_{23}$, the ICAL can discover the MH with a significance of $(2.2\text{--}3.8)\sigma$ with 10 years of data and assuming that these parameters are known exactly.

5.5 Sensitivity after marginalization over the oscillation parameters

In the previous section, we assumed that the neutrino oscillation parameters are known to an infinite precision. However, this is not the case. Certain combinations of the oscillation parameters with the wrong MH may mimic the signal for the true MH. While obtaining the MH discovery sensitivity, we must take this into account. In order to get a realistic estimate of the hierarchy sensitivity, we must allow for the current 3σ uncertainty in the oscillation parameters while fitting the data. The marginalized $\Delta\chi^2_{\text{ino}}$ is found by allowing $\sin^2 \theta_{23}$, $\sin^2 2\theta_{13}$ and Δm^2_{eff} to vary in the ranges indicated in Table 5.1. The solar oscillation parameters $(\sin^2 2\theta_{12}, \Delta m^2_{21})$ are kept fixed at values mentioned in Table 5.1, as they do not play a significant role in the MH analysis. We also keep δ_{CP} fixed at $0°$.

Fig. 5.7 shows the marginalized sensitivity for $\sin^2 \theta_{23} = 0.5$. We observe that for 10 years of ICAL exposure and for $\sin^2 2\theta_{13} = 0.1$, the statistical significance for the hierarchy discovery drops to 2.4σ from 2.7σ(for fixed parameters) after marginalization. The marginalized $\Delta\chi^2_{\text{ino}}$ for non-maximal $\sin^2 \theta_{23}$ is shown in Fig. 5.8. If $\sin^2 2\theta_{13} = 0.12$ and $\sin^2 \theta_{23} = 0.6$, ICAL can determine the hierarchy with a 3σ significance for 10 year of exposure. Depending on the true values of the oscillation parameters, the MH may be determined with a significance between $(1.4\text{--}3.3)\sigma$ with a 10 year run.

(a) True Hierarchy : Normal

(b) True Hierarchy : Inverted

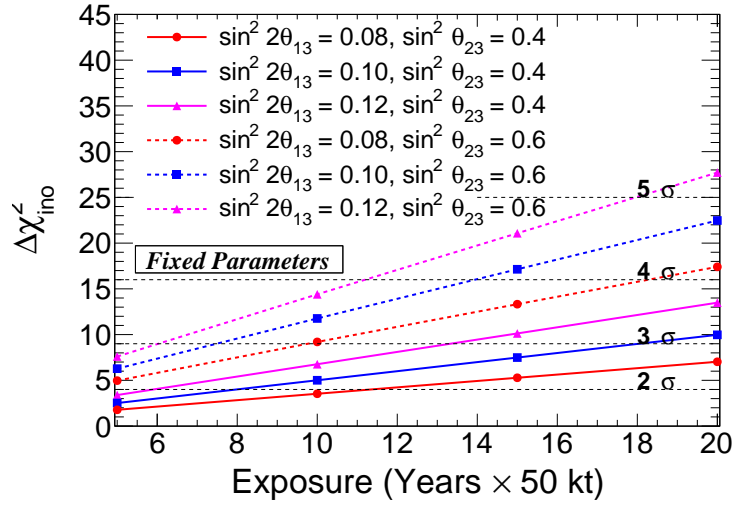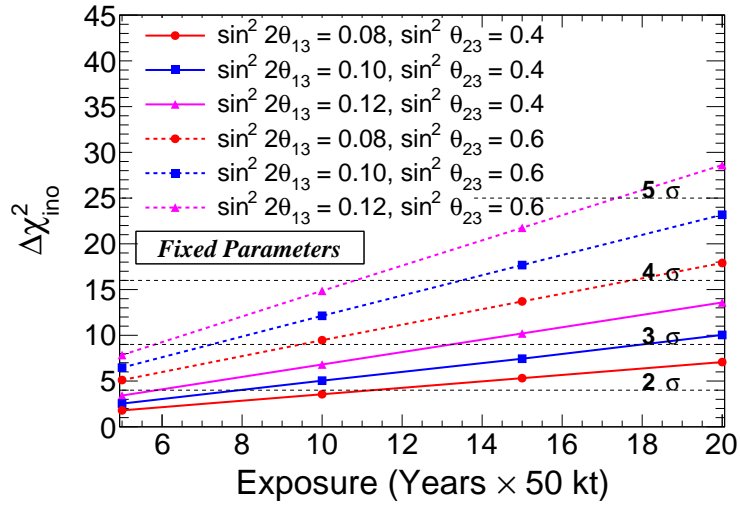Figure 5.6: Mass hierarchy sensitivity for the fixed oscillation parameters, and $\sin^2 \theta_{23} = 0.4, 0.6$
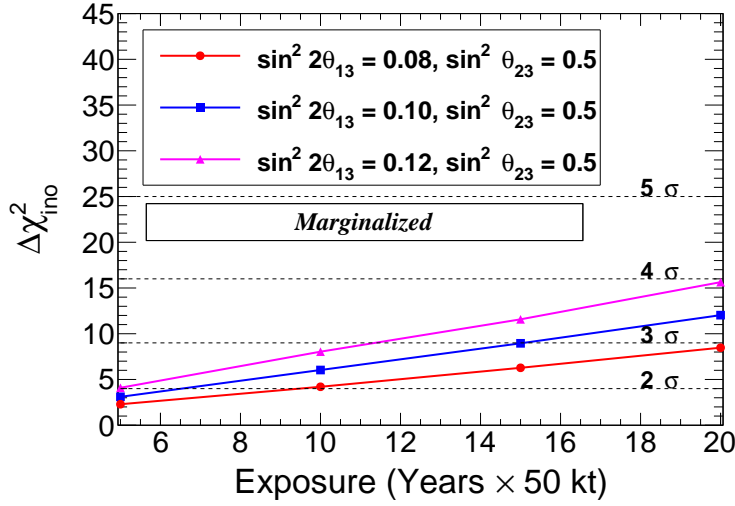
(a) True Hierarchy : Normal
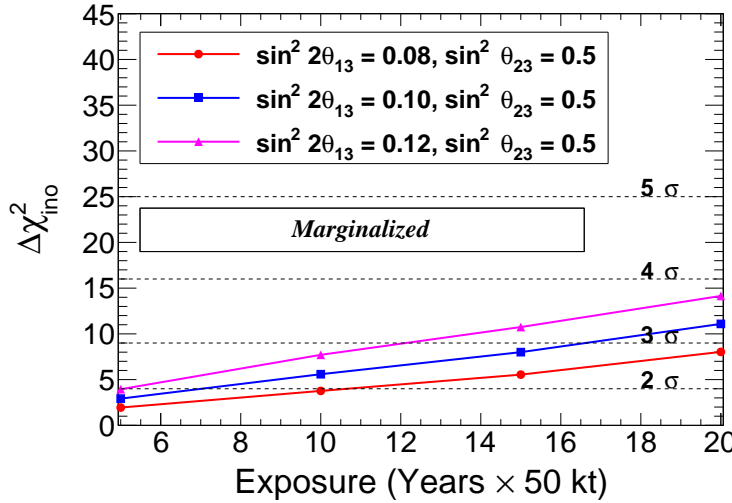
(b) True Hierarchy : Inverted

Figure 5.7: Marginalized mass hierarchy sensitivity for $\sin^2 \theta_{23} = 0.5$

5.6 Effect of Systematic Errors

The atmospheric neutrino flux predictions have large systematic uncertainties associated with them. This is in contrast to the accelerator neutrino experiments where the flux uncertainties can be kept under control with a near and a far detector setup and the beamline can be tuned to obtain the desired neutrino spectrum.
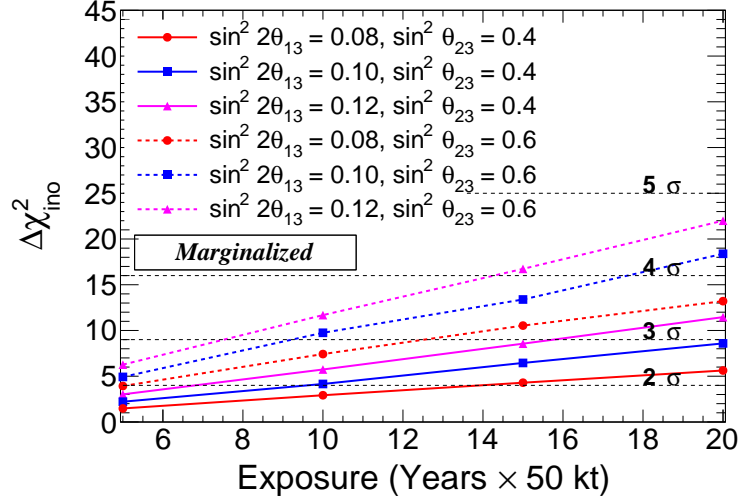
(a) True Hierarchy : Normal
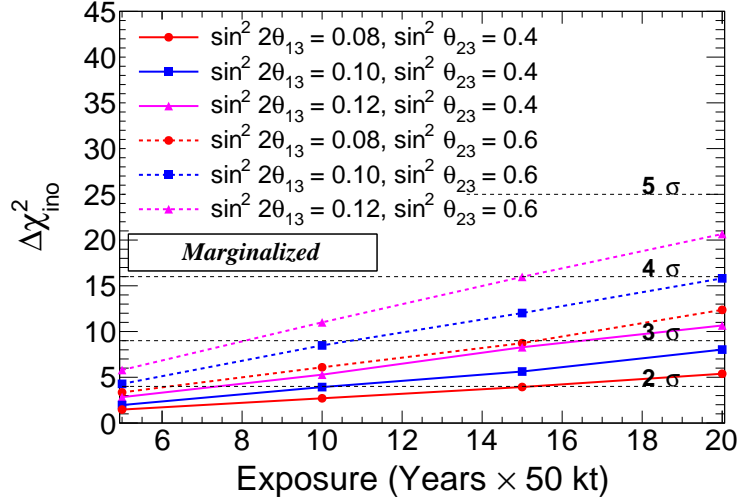
(b) True Hierarchy : Inverted

Figure 5.8: Marginalized mass hierarchy sensitivity for $\sin^2 \theta_{23} = 0.4$ and 0.6

For the ICAL analysis, we have considered five systematics as described in Section 4.5.5. We have checked that the uncertainty of the flux normalization, cross-section and the overall systematic produce minimal effect. The reason for such a behaviour is that these uncertainties are energy/angle independent and they get cancelled amongst up-going and down-going muon bins. The remaining two systematics on the neutrino energy spectrum (tilt error) and the zenith angle error are bin dependent and they create appreciable effects on the MH sensitivity. The most significant
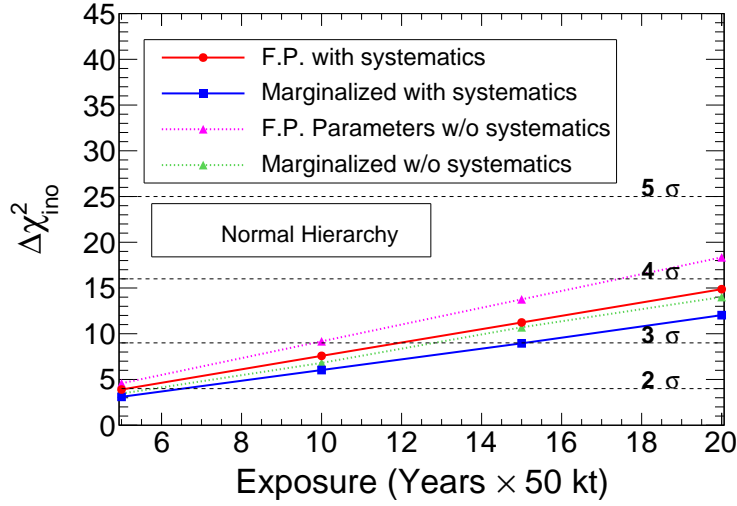
(a) True Hierarchy : Normal
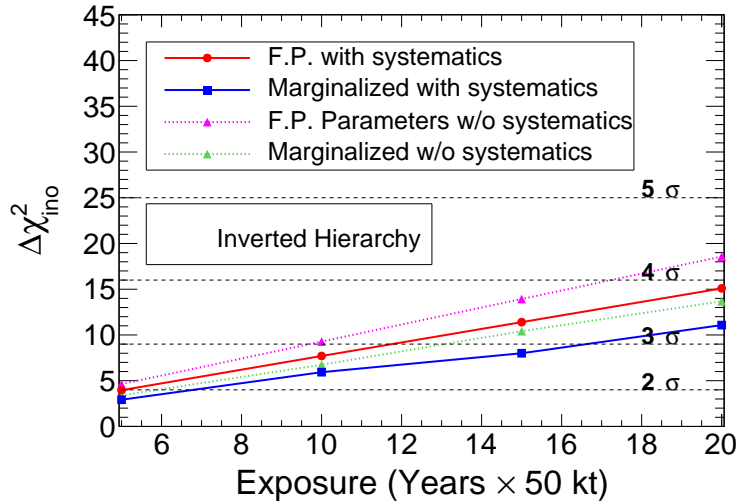
(b) True Hierarchy : Inverted

Figure 5.9: The effect of systematic error on MH sensitivity for Fixed and Marginalized oscillation parameters. The central values of the benchmark oscillation parameters have been used.

dilution in the ICAL sensitivity comes due to the error on the zenith angle. Fig. 5.9 shows the ICAL MH sensitivity without and with the inclusion of systematics, as a function of exposure, for the central values of the benchmark oscillation parameters. For an exposure of 50 kt $\times$ 10 years and fixed oscillation parameters, the significance of MH determination falls from 3.2σ to 2.8σ. In case of marginalized χ^2 it drops from 2.7σ to 2.4σ. We also note that with the inclusion of systematics, the linear

behaviour of χ^2 still holds. Thus, the MH sensitivity at the ICAL is dominated by statistics.

5.7 Sensitivity with Priors on Oscillation Parameters

By the time the ICAL detector starts taking data, values of the oscillation parameters $\sin^2 \theta_{23}$, $\sin^2 2\theta_{13}$ and $\Delta m^2_{\mathrm{eff}}$ will further be constrained by other accelerator and reactor neutrino experiments, such as T2K, NOνA, Daya Bay, RENO and Double Chooz. To reflect this, we add priors to χ^2_{ino} defined in Eqn. 4.16 :

$$
\begin{aligned}
\chi^2_{\mathrm{ino}} &= \chi^2_{\mathrm{ino}} + \left(\frac{\sin^2 2\theta_{23}(\mathrm{true}) - \sin^2 2\theta_{23}}{\sigma_{\sin^2 2\theta_{23}}} \right)^2 + \left(\frac{|\Delta m^2_{\mathrm{eff}}|(\mathrm{true}) - |\Delta m^2_{\mathrm{eff}}|}{\sigma_{\Delta m^2_{\mathrm{eff}}}} \right)^2 \\
&+ \left(\frac{\sin^2 2\theta_{13}(\mathrm{true}) - \sin^2 2\theta_{13}}{\sigma_{\sin^2 2\theta_{13}}} \right)^2 .
\end{aligned}
\tag{5.4}
$$

We have taken projected priors of 0.65% prior on $\sin^2 \theta_{23}$, 2% prior on $\Delta m^2_{\mathrm{eff}}$ and 0.1% prior on $\sin^2 2\theta_{13}$ [135]. Fig. 5.10 shows the comparison of χ^2_{ino} for fixed parameters, marginalized without priors and marginalized with priors. It is seen that with the addition of priors, the marginalized χ^2_{ino} is restored to the fixed parameter value. A more realistic analysis may be carried out by performing a global fit of the data from the ICAL, accelerator and reactor neutrino experiments, instead of adding priors. In such an analysis, higher MH sensitivities can be obtained due to, (i) the accelerator and reactor neutrino experimental constraint of the oscillation parameters, and (ii) their own MH sensitivities are combined with other experiments.

5.8 Sensitivity as a function of δ_{CP}

In the analysis so far, δ_{CP} was assumed to be fixed to $0°$. In Fig. 5.11, we show the effect on $\Delta\chi^2_{\mathrm{ino}}$ as a function of δ_{CP} (true). It can be seen that the fixed parameter
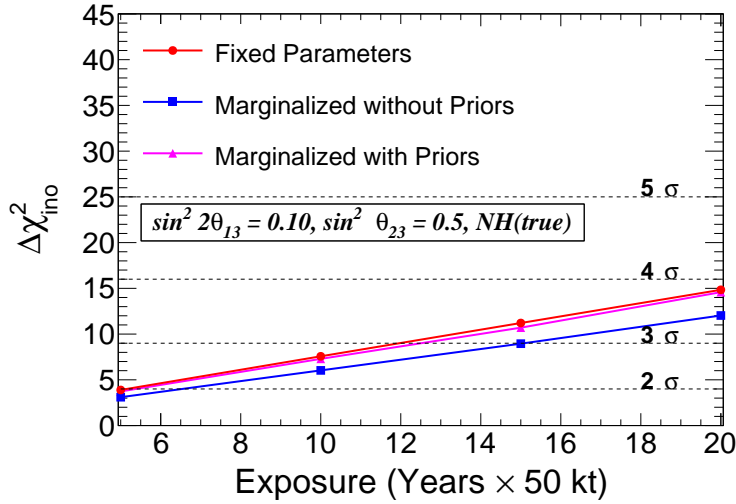
Figure 5.10: Marginalized hierarchy sensitivity with priors

$\Delta\chi^2_{\text{ino}}$ is independent of true δ_{CP} value (pink line). Further, a marginalization over δ_{CP} only, produces no change in the hierarchy sensitivity (blue line). A full marginalization over $\sin^2\theta_{23}$, $\sin^2 2\theta_{13}$, Δm^2_{eff} and δ_{CP} also gives the hierarchy sensitivity independent of true δ_{CP} value (red line). Therefore, it is not necessary to marginalize χ^2_{ino} over δ_{CP} and the mass hierarchy sensitivity at ICAL is independent of the δ_{CP} value. This feature is expected because of the fact that the $P_{\mu\mu}$ dependence on δ_{CP} is suppressed by the factor $\Delta m^2_{21}/\Delta m^2_{32}$ [134]. The fact that the MH determination is independent of δ_{CP} in the atmospheric experiments is complementary to the accelerator neutrino experiments T2K and NOνA, where the MH determination depends on the δ_{CP} value.

5.9   Summary

The determination of the neutrino mass hierarchy has become the prime goal in the area of neutrino physics after the discovery of a relatively large θ_{13}. The ICAL@INO experiment will exploit the earth matter effects for this measurement. Matter effects cause a suppression of $P_{\mu\mu}$ for NH in the neutrino energy range 5-10 GeV and for baselines of 7000 - 11,000 km. For true IH, $P_{\mu\mu}$ suppression occurs for the anti-neutrinos. The ICAL will attempt to discover the neutrino mass hierarchy by measuring the event rates for μ^- and μ^+. The fine muon energy and direction resolutions, high
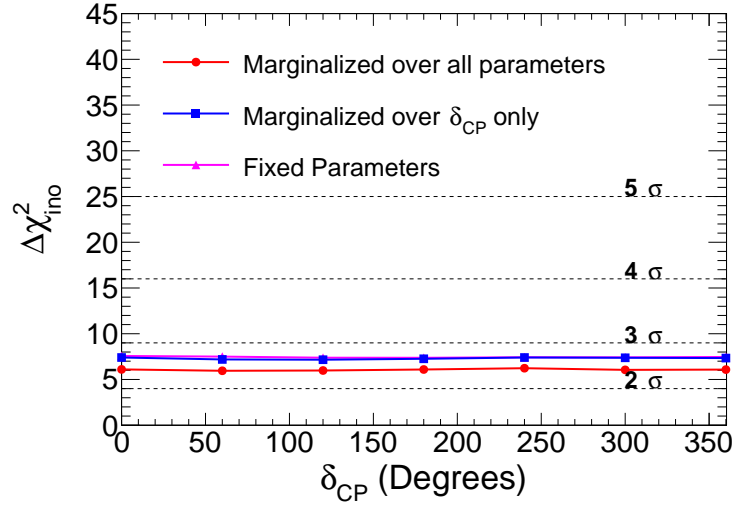
Figure 5.11: Effect of changing δ_{CP} on the sensitivity

reconstruction and CID efficiencies make the ICAL an ideal detector for this task.

We find that with 10 years of ICAL data, the mass hierarchy can be discovered with a significance of $(1.4\text{--}3.3)\sigma$ for the benchmark values of the oscillation parameters, after marginalizing the χ^2_{ino} over the allowed 3σ range of the parameters $\sin^2 2\theta_{13}$, $\sin^2 \theta_{23}$ and Δm^2_{31}. Addition of priors helps to restore the MH sensitivity to their fixed parameter values, or a significance of $(2.2 - 3.8)\sigma$ for 10 years. χ^2_{ino} rises linearly with the exposure. The MH sensitivities are identical for true NH and IH. The systematic errors in the neutrino energy spectrum (tilt error) and the zenith angle error contribute dominantly to lower the MH sensitivity. The MH discovery at ICAL with atmospheric neutrinos is independent of the phase δ_{CP}, which is a complementary feature to the long baseline neutrino experiments.

Chapter 6

Precision Measurements of Atmospheric Oscillation Parameters with ICAL

After the SK experiment established oscillations in the atmospheric neutrinos, the associated parameters $(\sin^2\theta_{23}, |\Delta m^2_{32}|)$ have been measured with increasing precision over time. The accelerator neutrino experiments MINOS and T2K have more recently greatly refined the precision on these parameters. The ICAL experiment, whose goal is to determine the neutrino mass hierarchy is also a good instrument for the precision measurement of the atmospheric parameters. ICAL will reconfirm the atmospheric neutrino oscillations and will provide the first observation of the first oscillation minimum in the $P_{\mu\mu}$ channel. By utilizing the matter effects, ICAL may also be able to provide hints on the octant of θ_{23}, if it is non-maximal.

6.1   Details of the Analysis

We simulate the "Observed" data set using the method described in Section 4.5. Since in this analysis we want to constrain $\sin^2\theta_{23}$ and $|\Delta m^2_{32}|$, and the variation of θ_{12} or $|\Delta m^2_{21}|$ within the current error bars is observed not to affect the results, we take the value of these two parameters to be fixed to those given in Table 4.1. We use a prior

on the parameter $\sin^2 2\theta_{13}$ as :

$$\chi^2 = \chi^2_{\text{ino}} + \left(\frac{\sin^2 2\theta_{13}(\text{true}) - \sin^2 2\theta_{13}}{\sigma_{\sin^2 2\theta_{13}}} \right)^2 , \tag{6.1}$$

where $\sigma_{\sin^2 2\theta_{13}}$ is the current 1σ error on $\sin^2 2\theta_{13}$, and is taken as 0.013 in this analysis. Of course, during the operation of INO, the error $\sigma_{\sin^2 2\theta_{13}}$ will reduce, and within a few years, $\sin^2 2\theta_{13}$ may be considered to be a fixed parameter.

6.2 Precision Measurement Results

To present the reach of the ICAL on the atmospheric parameters $\sin^2 \theta_{23}$ and Δm^2_{32}, we take the true values of the oscillation parameters as given in Table 4.1. Here, we use the parameter Δm^2_{32} ($= \Delta m^2_{31} - \Delta m^2_{21}$) instead of $|\Delta m^2_{31}|$, the current limits on which are given in [54]. The χ^2 values as functions of $\sin^2 \theta_{23}$ and $|\Delta m^2_{32}|$ are shown in Fig. 6.1(a) and 6.1(b), respectively. The minimum value of χ^2 in this analysis is 0, since the values of the oscillation parameters, as well as the NUANCE event set are identical for both "Prediction" and "Observation" in the χ^2 construction. (At the true point for the oscillation parameters.)
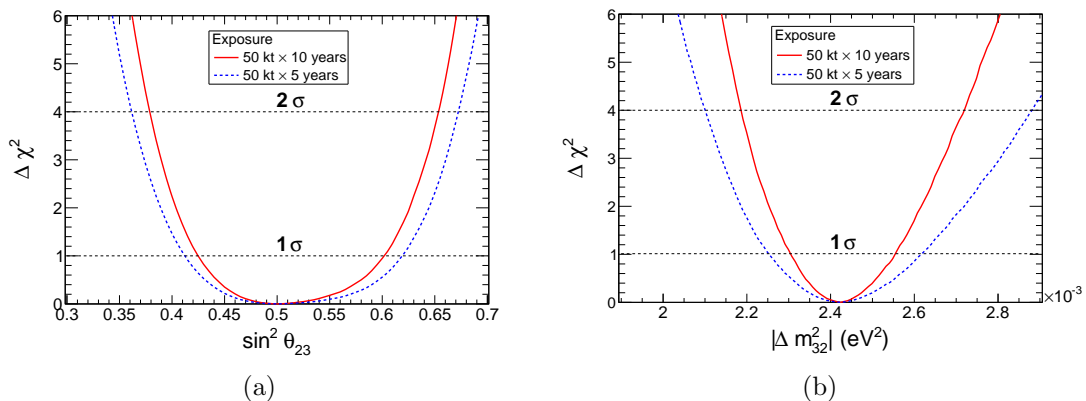

Figure 6.1: The panel (a) shows the χ^2 as a function of $\sin^2 \theta_{23}$ for $|\Delta m^2_{32}| = 2.424 \times 10^{-3}$ eV^2 and $\sin^2 \theta_{23}(\text{true}) = 0.5$. The panel (b) shows the χ^2 as a function of $|\Delta m^2_{32}|$ for $\sin^2 \theta_{23} = 0.5$ and $|\Delta m^2_{32}|(\text{true}) = 2.424 \times 10^{-3}$ eV^2

The precision on these parameters may be quantified by

$$\text{precision} = \frac{p_{max} - p_{min}}{p_{max} + p_{min}}, \tag{6.2}$$

where p_{max} and p_{min} are the largest and smallest value of the concerned oscillation parameters determined at the given C.L. from the atmospheric neutrino measurements at ICAL for a given exposure. We find that after 5 years of running of this experiment, ICAL would be able to measure $\sin^2 \theta_{23}$ to a precision of 20% and $|\Delta m^2_{32}|$ to 7.4% at 1σ. With 10 years exposure, these numbers improve to 17% and 5.1% for $\sin^2 \theta_{23}$ and $|\Delta m^2_{32}|$, respectively. The precision on $\sin^2 \theta_{23}$ is primarily governed by the event statistics, and is expected to improve with higher statistics. It will also improve as the systematic errors are reduced. If the flux normalization error were to come down from 20% to 10%, the precision on $\sin^2 \theta_{23}$ would improve to 14% for 10 years of exposure. Reducing the zenith angle error from 5% to 1% would also improve this precision to $\sim 14\%$. On the other hand, the precision on $|\Delta m^2_{32}|$ is governed by the L/E resolution of the detector.

A few more detailed observations may be made from the χ^2 plots in fig. 6.1. From Fig. 6.1(a) one can notice that the precision on θ_{23} when it is in the first octant ($\sin^2 \theta_{23} < 0.5$) is slightly better than when it is in the second octant ($\sin^2 \theta_{23} > 0.5$), even though the muon neutrino survival probability depends on $\sin^2 2\theta_{23}$ at the leading order. This asymmetry about $\sin^2 \theta_{23} = 0.5$ stems mainly from the full three-flavor analysis that we have performed in this study. In particular, we have checked that the non-zero value of θ_{13} is responsible for the asymmetry observed in this figure. On the other hand, the χ^2 asymmetry about the true value of $|\Delta m^2_{32}|$ observed in Fig. 6.1(b) is an effect that is present even with a two-flavor analysis.

The precisions obtainable at the ICAL for $\sin^2 \theta_{23}$ and $|\Delta m^2_{32}|$ are expected to be correlated. The correlated reach of ICAL for these parameters are shown in Figs. 6.2(a) and 6.2(b). These are the main results of this analysis. As noted above, our three-neutrino analysis should be sensitive to the octant of θ_{23}. Therefore we choose to present our results in terms of $\sin^2 \theta_{23}$ instead of $\sin^2 2\theta_{23}$. Though the constant-χ^2 contours still look rather symmetric about $\sin^2 \theta_{23} = 0.5$, that is mainly due to the true value of $\sin^2 \theta_{23}$ being taken to be 0.5. The values of $\sin^2 \theta_{23}$ away from 0.5 would make the contours asymmetric and would give rise to some sensitivity

to the octant of θ_{23}, as we shall see later.

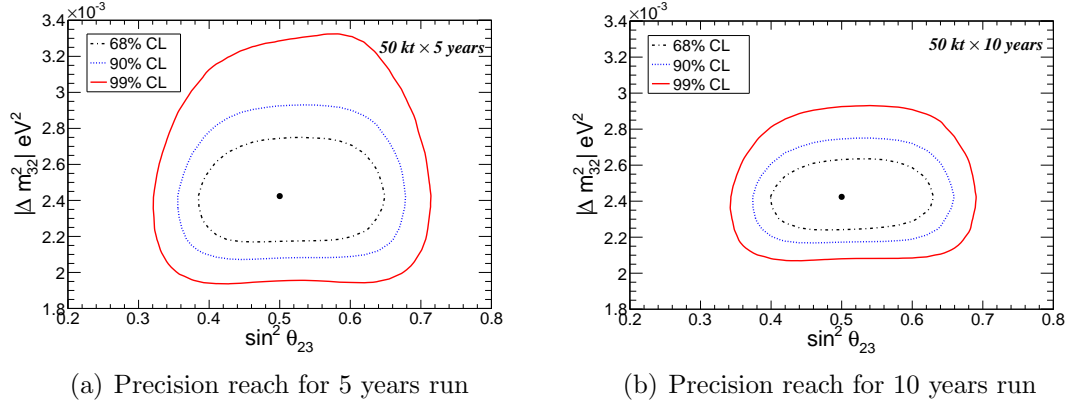(a) Precision reach for 5 years run   (b) Precision reach for 10 years run

Figure 6.2: The precision reach expected at ICAL in the $\sin^2\theta_{23} - |\Delta m^2_{32}|$ plane at various confidence levels. The black(broken), blue(dotted) and red(solid) lines show 68%, 90% and 99% C.L contours. The true values of $\sin^2\theta_{23}$ and $|\Delta m^2_{32}|$ used for generating data are shown by the black dots. The true values of other parameters used are given in Table 4.1. Panel (a) is for five-year running of the 50 kt detector while (b) is for ten years exposure.

6.3 Binning Study

For this analysis, we have taken $\cos\theta$ bins of width 0.1. The muon angle resolution in ICAL is however better than 1° for almost all values of the zenith angle. Therefore, it is possible to take finer bins. In order to study the impact of our choice of binning on the precision measurements of $\sin^2\theta_{23}$ and $|\Delta m^2_{32}|$ in ICAL, we reduce the $\cos\theta$ bin size to 0.05 and the size of the E bins to 0.5 GeV. In Fig. 6.3, we show the effect of taking these finer bins in E and $\cos\theta$ on the precision reach of the two parameters. The figure corresponds to 10 years of ICAL exposure. The finer bins bring only a marginal improvement in the precision measurement of both $\sin^2\theta_{23}$ and $|\Delta m^2_{32}|$. We therefore use 10 E_μ bins with width 1 GeV and 20 $\cos\theta_\mu$ bins with width 0.1.
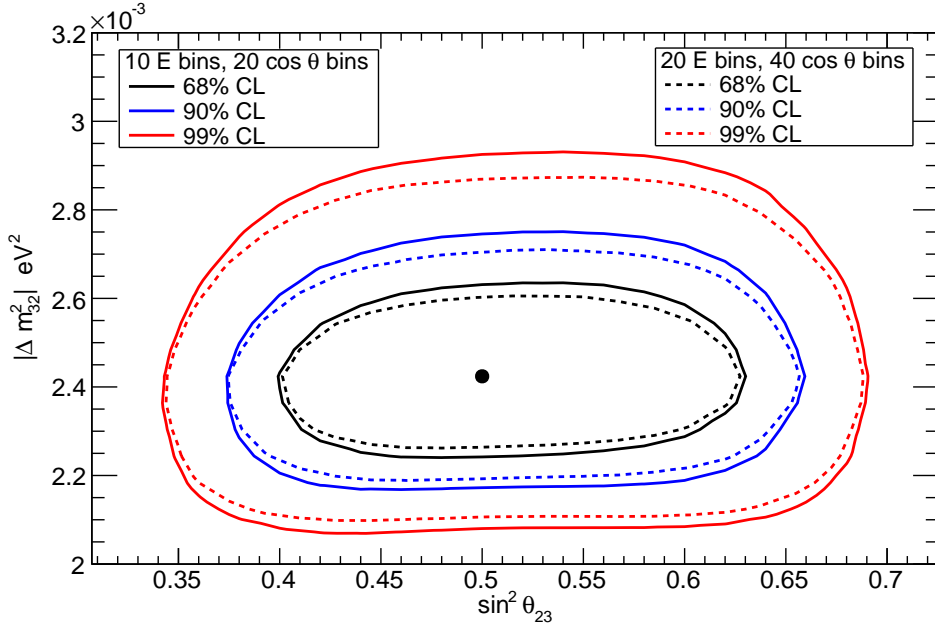
Figure 6.3: Effect of binning on the precision reach expected from the analysis of 50 kt × 10 years data of atmospheric neutrinos in ICAL. The black, blue and red lines show 68%, 90% and 99% C.L contours. The solid lines show the contours for (E, $\cos\theta$) bin widths of (1 GeV, 0.1) while the broken lines show the contours for (E, $\cos\theta$) bin widths of (0.5 GeV, 0.05).

6.4 Comparison of projected ICAL constraints with other Experiments

In Fig. 6.4 we show the comparison of the precision reach on the atmospheric neutrino oscillation parameters at ICAL with that obtained from other experiments currently. Note that here we use the parameter $\sin^2 2\theta_{23}$ instead of $\sin^2 \theta_{23}$ in order to make a direct comparison. The blue and red lines show the expected sensitivity from atmospheric neutrino measurements at ICAL after 5 years and the 10 years exposure, respectively. The green line is the 90% C.L.-allowed contour obtained by the zenith angle analysis of SK atmospheric neutrino measurements, while the pink line is the contour obtained by their L/E analysis [136]. The black line shows the 90% C.L. allowed region given by the combined analysis of the full MINOS data including 10.71×10^{20} POT for the ν_μ-beam, 3.36×10^{20} POT for the $\bar{\nu}_\mu$-beam, as well as the atmospheric neutrino data corresponding to an exposure of 37.9 kt-years [137].

The grey (dot-dot-dashed) line shows the T2K ν_μ disappearance analysis results for 3.01×10^{20} POT [138].
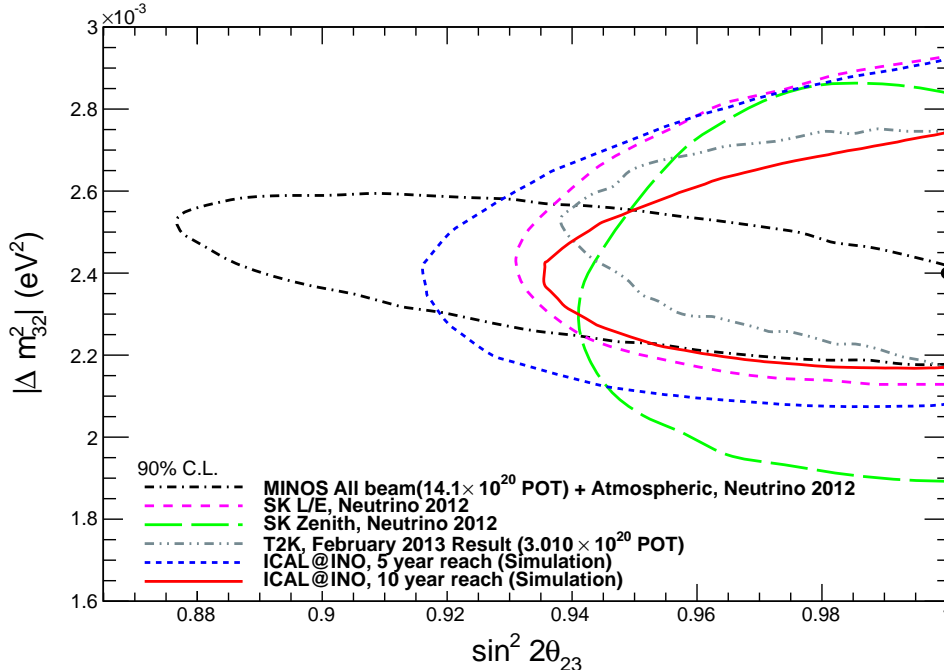
Figure 6.4: Comparison of the reach of ICAL@INO with the current results from other neutrino experiments. The black dot in the figure denotes the point where the ICAL data was generated. The true values of the other oscillation parameters are given in Table 4.1.

From Fig. 6.4 it may be observed that, with 5 years of exposure, ICAL will be able to almost match the precision on $|\Delta m^2_{32}|$ obtained from the SK L/E analysis currently. With 10 years data this will improve, though it will still not be comparable to the precision we already have from the MINOS experiment. Since the direction of neutrinos in MINOS is known accurately, their L/E is known to a greater precision and their measurement of $|\Delta m^2_{32}|$ is consequently more accurate. The precision of ICAL on $\sin^2 2\theta_{23}$ in 10 years may be expected to be comparable to what we currently have from SK. (Of course by the time ICAL completes 10 years, SK would have collected more data.) This precision is controlled to a large extent by the total number of events. It may be noticed that the sensitivity of ICAL to $\sin^2 2\theta_{23}$ and $|\Delta m^2_{32}|$ is not expected to surpass the precision we already have from the current set of experiments. In fact, the precision on these parameters are expected to improve

significantly with the expected data from T2K [44] and NOνA [56], and ICAL will not be competing with them as far as these precision measurements are concerned. (The recent T2K results [139] already claim a better precision than the ICAL reach in 10 years.) The ICAL data will however give complementary information on these parameters, which will significantly contribute to the improvement of the precision on the global fit.

6.5 Octact of θ_{23}
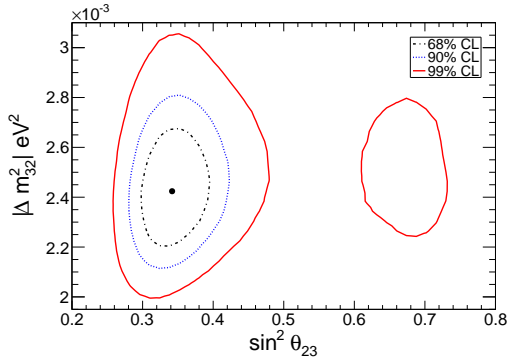
(a) $\sin^2 2\theta_{23} = 0.9$, first octant ($\sin^2 \theta_{23} = 0.342$)
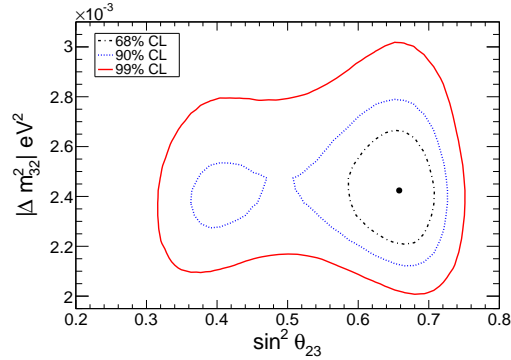
(b) $\sin^2 2\theta_{23} = 0.9$, second octant ($\sin^2 \theta_{23} = 0.658$)
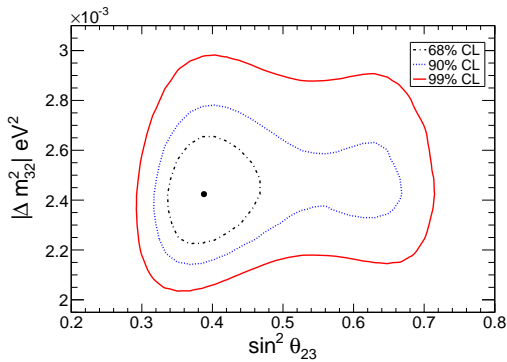
(c) $\sin^2 2\theta_{23} = 0.95$, first octant ($\sin^2 \theta_{23} = 0.388$)
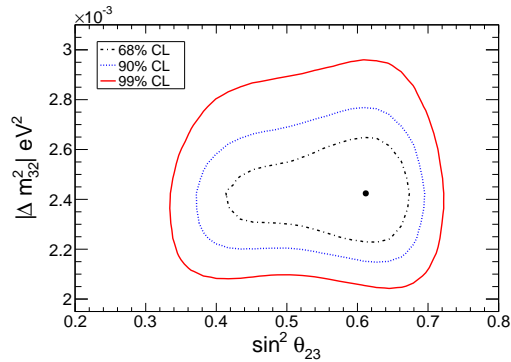
(d) $\sin^2 2\theta_{23} = 0.95$, second octant ($\sin^2 \theta_{23} = 0.612$)

Figure 6.5: The projected reach in the $\sin^2 \theta_{23} - |\Delta m^2_{32}|$ plane for four different non-maximal choices of θ_{23}. The black(broken), blue(dotted) and red(solid) lines show 68%, 90% and 99% C.L. contours for 10 years of 50 kt ICAL run. Note that we use normal hierarchy, and assume that it is already known.

The leading terms in $P_{\mu\mu}$ are proportional to $\sin^2 2\theta_{23}$ and the θ_{23} octant discrimination is not possible. However, the Earth matter effects in atmospheric neutrinos can be used to distinguish maximal from non-maximal θ_{23} mixing and can lead to the determination of the correct θ_{23} octant [140, 141, 142]. We show in Fig. 6.5 the potential of 10 years of ICAL run for distinguishing a non-maximal value of θ_{23} from maximal mixing in the case where $\sin^2 2\theta_{23} = 0.90$ ($\sin^2 \theta_{23} = 0.342, 0.658$) and $\sin^2 2\theta_{23} = 0.95$ ($\sin^2 \theta_{23} = 0.388, 0.612$). Note that the current 3σ allowed range of $\sin^2 2\theta_{23}$ is $(0.91, 1.0)$. The figure shows that, if the value of θ_{23} is near the current 3σ bound and in the first octant, then it may be possible to exclude maximal mixing to 99% C.L. with this 2-parameter analysis. If θ_{23} is in the second octant, or if $\sin^2 2\theta_{23}$ is larger than 0.9, the exclusion of the maximal mixing becomes a much harder task.

Fig. 6.5 can also be used to quantify the reach of ICAL for determining the correct octant of θ_{23}, if the value of $\sin^2 2\theta_{23}$ is known. This can be seen by comparing the χ^2 value corresponding to the true value of $\sin^2 \theta_{23}$, but in the wrong octant, with that corresponding to the true value of $\sin^2 \theta_{23}$. We find that, for $\sin^2 2\theta_{23} = 0.9$, i.e. just at the allowed 3σ bound, the octant can be identified at $>95\%$ C.L. with 10 years of ICAL run if θ_{23} is in the first octant. However if θ_{23} is in the second octant, the identification of the octant would be much harder: θ_{23} in the wrong octant can be disfavored only to about 85% C.L.. The situation is more pessimistic if $\sin^2 2\theta_{23}$ is closer to unity.

The precision on $|\Delta m_{32}^2|$ will keep improving with ongoing and future long baseline experiments. The inclusion of the information may improve the chance of ICAL@INO being able to identify deviation of θ_{23} from maximal mixing and its octant to some extent.

6.6 Conclusions

Even though the primary goal of the ICAL is to determine the neutrino mass hierarchy, it can also make precision measurements of the atmospheric parameters $(\sin^2 \theta_{23}, |\Delta m_{32}^2|)$.

We find that the values of $\sin^2 \theta_{23}$ and $|\Delta m_{32}^2|$ may be determined at an accuracy

of 17% and 5.1% respectively. The sensitivities with the data at ICAL only are not expected to be better than the current constraints. Indeed, some of the other experiments in the next decade may do much better. However the measurement at ICAL will be complementary and may be expected to contribute significantly towards the precision of parameters in a global fit.

By using the matter effects in the atmospheric neutrinos, ICAL may also be able to provide hints on θ_{23} octant and its deviation from maximality. We find that 10 years of ICAL can exclude maximal mixing or the θ_{23} value in the other octant to >95% C.L. only if the actual θ_{23} is in the first octant and close to the current 3σ lower bound to 99 % C.L., for true NH. Octant determination seems to be a difficult task with the ICAL data alone.

Chapter 7

Summary

The field of neutrino physics has evolved rapidly over the last 10 years. Several atmospheric, solar, reactor and accelerator neutrino experiments have established neutrino oscillations and have made precision measurements of the oscillation parameters.

The ICAL detector at INO is an upcoming experiment in India. It consists of a 50 kt magnetized iron calorimeter with 150 alternate layers of iron plates as target mass for neutrino interactions and the RPCs as active detector elements. The RPCs register the position and the time of the hit when a particle passes through it. The iron plates are magnetized with a field of 1.3–1.5 tesla, which will enable it to identify the charge of particles and to separate neutrinos and anti-neutrinos. The ICAL is optimized to measure the muon energy, direction and charge, produced in the CC ν_μ interactions in the energy range up to a few GeV.

Using the GEANT4-based simulation and reconstruction code developed by the INO collaboration, the muon response of the ICAL detector has been studied under certain assumptions. This software uses a Kalman Filter based algorithm to reconstruct the muon momentum, charge and the interaction vertex. The muon reconstruction in the ICAL detector is parametrized in terms of (i) energy resolution (σ_E), (ii) direction resolution ($\sigma_{\cos\theta}$), (iii) reconstruction efficiency (ϵ_R), and (iv) charge identification efficiency (ϵ_C) in the energy range 0.5–25 GeV and for all directions. We find that all these quantities are strongly dependent on the incident energy and direction. The energy resolutions for the muons is found to be 10–25 %, while the

$\cos \theta_\mu$ resolutions are about 0.005–0.045 (or the θ_μ resolution of about $1°$). The efficiency of reconstruction varies between 10–90 %, improving with energy. The charge identification efficiencies are found to be between 95–100 %. The presence of dead spaces such as the support structures, gaps between the RPCs, magnet coils, generally degrades the muon energy reconstruction, as no hits are recorded in these areas. Sometimes, a single muon track is reconstructed as two or more tracklets, resulting into a poor energy estimation. The best muon response is obtained around $E_\mu \sim$ 5–8 GeV, which is a very important region for the neutrino mass hierarchy discovery. The muon resolutions and the efficiencies are stored as a look-up table for the physics analysis.

For the oscillation analysis, a ROOT-based package has been developed for this thesis work. We use the event generator NUANCE to simulate the neutrino interactions inside the detector. To generate events, un-oscillated atmospheric neutrino fluxes have been used. The oscillation effects are then incorporated using the Re-weighting algorithm, which is based on the MC accept-reject algorithm. The Re-Weighting algorithm greatly helps to reduce the computing requirements for the analysis. We perform binning of the muon events in terms of $(E_\mu, \cos \theta_\mu)$. After obtaining the true muon distribution from the Re-Weighted NUANCE events, the ICAL muon response is folded in to smear it. Thus we obtain the measured distribution of muons. We then construct the χ^2 from the measured muon distributions. The systematic errors are included in the χ^2 analysis via the method of pulls. Five systematics have been considered in this analysis : (i) Flux normalization error, (ii) Cross-section error, (iii) Overall systematics, (iv) Tilt error, and (iv) Zenith angle error.

The ICAL will employ the Earth Matter effects in the atmospheric neutrinos to determine the neutrino mass hierarchy. The charge separation capability and the fine energy and direction resolutions gives the ICAL an edge over other experiments. The ICAL can determine the mass hierarchy to a significance of $(1.4–3.3)\sigma$ in a 10 years run, depending on the value of the oscillation parameters $\sin^2 \theta_{23}$ and $\sin^2 2\theta_{13}$. Including information on oscillation parameters obtained from other neutrino experiments will improve the statistical significance to $(2.2 - 3.8)\sigma$ in a 10 years run. The hierarchy measurement at ICAL is independent of the $\delta_{\rm CP}$ value.

The ICAL is also a suitable experiment to make precision measurements of the atmospheric oscillation parameters ($\sin^2 \theta_{23}, |\Delta m_{32}^2|$). With 10 years of ICAL data, we can determine $\sin^2 \theta_{23}$ and $|\Delta m_{32}^2|$ to a precision of 17 % and 5.1 %, respectively. We also explore the possibility of determining the deviation of θ_{23} from maximal mixing and its octant. We find that both these tasks will be possible with ICAL, if the true value of θ_{23} is close to its current 3σ bound and is in the first octant. Otherwise they appear to be difficult for the ICAL to determine. The ICAL data will be complementary to the LBL data for the precision measurement of the atmospheric parameters and will help to improve the global fits.

The results presented in this thesis are obtained by using only the information on the muon energy and direction. However, the ICAL can measure the hadron energy with coarse resolutions. Including the hadron energy information into the analysis will help to improve the ICAL physics sensitivities.

Bibliography

[1] S. Chatrchyan *et al.* [CMS Collaboration], Phys. Lett. B **716**, 30 (2012) [arXiv:1207.7235 [hep-ex]].

[2] G. Aad *et al.* [ATLAS Collaboration], Phys. Lett. B **716**, 1 (2012) [arXiv:1207.7214 [hep-ex]].

[3] R. N. Mohapatra, S. Antusch, K. S. Babu, G. Barenboim, M. -C. Chen, A. de Gouvea, P. de Holanda and B. Dutta *et al.*, Rept. Prog. Phys. **70**, 1757 (2007) [hep-ph/0510213].

[4] P. Minkowski, Phys. Lett. B **67**, 421 (1977).

[5] M. Gell-Mann, P. Ramond and R. Slansky, Conf. Proc. C **790927**, 315 (1979) [arXiv:1306.4669 [hep-th]].

[6] Z. Maki, M. Nakagawa and S. Sakata, Prog. Theor. Phys. **28**, 870 (1962).

[7] B. Pontecorvo, Sov. Phys. JETP **26**, 984 (1968) [Zh. Eksp. Teor. Fiz. **53**, 1717 (1967)].

[8] B. Kayser, arXiv:1206.4325 [hep-ph].

[9] S. M. Bilenky, arXiv:1208.2497 [hep-ph].

[10] M. Blennow and A. Y. .Smirnov, Adv. High Energy Phys. **2013**, 972485 (2013) [arXiv:1306.2903 [hep-ph]].

[11] S. P. Mikheev, A. Yu. Smirnov, Nuovo Cim. **C9**, 17 (1986).

[12] S. P. Mikheev, A. Yu. Smirnov, Sov. J. Nucl. Phys. **42**, 913 (1985).

[13] L. Wolfenstein, Phys. Rev. D **17**, 2369 (1978).

[14] Neutrino Unbound, http://www.nu.to.infn.it/

[15] J. N. Bahcall, A. M. Serenelli and S. Basu, Astrophys. J. **621**, L85 (2005) [astro-ph/0412440].

[16] J. N. Bahcall, A. M. Serenelli and S. Basu, Astrophys. J. Suppl. **165**, 400 (2006) [astro-ph/0511337].

[17] R. Davis, Prog. Part. Nucl. Phys. **32**, 13 (1994).

[18] R. Davis, Phys. Rev. Lett. **12**, 303 (1964).

[19] Bruce T. Cleveland *et al.* (Homestake), Astrophys. J. **496**, 505 (1998).

[20] C. Pena-Garay and A. Serenelli, arXiv:0811.2424 [astro-ph].

[21] J. N. Abdurashitov *et al.* (SAGE), Phys. Rev. **C80**, 015807 (2009), arXiv:0901.2200 [nucl-ex].

[22] W. Hampel *et al.* (GALLEX), Phys. Lett. **B447**, 127 (1999).

[23] F. Kaether, W. Hampel, G. Heusser, J. Kiko, T. Kirsten, Phys. Lett. **B685**, 47 (2010), arXiv:1001.2731 [hep-ex].

[24] K. S. Hirata *et al.* (Kamiokande), Phys. Rev. Lett. **63**, 16 (1989).

[25] Y. Fukuda *et al.* (Super-Kamiokande), Phys. Rev. Lett. **81**, 1158 (1998), hep-ex/9805021.

[26] J. Hosaka *et al.* (Super-Kamkiokande), Phys. Rev. **D73**, 112001 (2006), hep-ex/0508053.

[27] K. Abe *et al.* (Super-Kamiokande), Phys. Rev. **D83**, 052010 (2011), arXiv:1010.0118 [hep-ex].

[28] J. Boger *et al.* [SNO Collaboration], Nucl. Instrum. Meth. A **449**, 172 (2000) [nucl-ex/9910016].

[29] B. Aharmim *et al.* (SNO), Phys. Rev. **C87**, 015502 (2013), arXiv:1107.2901 [nucl-ex].

[30] B. Aharmim *et al.* (SNO), Phys.Rev. **C88**, 025501 (2013), arXiv:1109.0763 [nucl-ex].

[31] K. Eguchi *et al.* (KamLAND), Phys. Rev. Lett. **90**, 021802 (2003), hep-ex/0212021.

[32] S. Abe *et al.* (KamLAND), Phys. Rev. Lett. **100**, 221803 (2008), arXiv:0801.4589 [hep-ex].

[33] A. Gando *et al.* (KamLAND), Phys.Rev. **D88**, 033001 (2013), arXiv:1303.4667 [hep-ex].

[34] D. Casper *et al.* (IMB), Phys. Rev. Lett. **66**, 2561 (1991).

[35] K. S. Hirata *et al.* (Kamiokande), Phys. Lett. **B205**, 416 (1988).

[36] M. Sanchez *et al.* (Soudan 2), Phys. Rev. **D68**, 113004 (2003), hep-ex/0307069.

[37] Y. Fukuda *et al.* (Super-Kamiokande), Phys. Rev. Lett. **81**, 1562 (1998), hep-ex/980700

[38] Y. Ashie *et al.* (Super-Kamiokande), Phys. Rev. Lett. **93**, 101801 (2004), hep-ex/0404034.

[39] J. Hosaka *et al.* [Super-Kamiokande Collaboration], Phys. Rev. D **74**, 032002 (2006) [hep-ex/0604011].

[40] M. H. Ahn *et al.* (K2K), Phys. Rev. **D74**, 072003 (2006), hep-ex/0606032.

[41] Alec T. Habig, E. W. Grashorn (MINOS), hep-ex/0507018, 29th International Cosmic Ray Conference (ICRC 2005), Pune, India, 3-11 Aug 2005.

[42] D.G. Michael *et al.* (MINOS), Phys. Rev. Lett. **97**, 191801 (2006), hep-ex/0607088.

[43] P. Adamson *et al.* (MINOS), Phys. Rev. Lett. 110, **251801**, 251801 (2013), arXiv:1304.6335 [hep-ex].

[44] N. Abgrall *et al.* (T2KK. Abe), Nucl. Instrum. Meth. **A659**, 106 (2011), arXiv:1106.1238 [physics].

[45] K. Abe *et al.* (T2K), Phys. Rev. Lett. 111, **211803**, 211803 (2013), arXiv:1308.0465 [hep-ex].

[46] M. Apollonio *et al.* (CHOOZ), Eur. Phys. J. **C27**, 331 (2003), hep-ex/0301017.

[47] K. Abe *et al.* (T2K), Phys. Rev. Lett. **107**, 041801 (2011), arXiv:1106.2822 [hep-ex].

[48] P. Adamson *et al.* (MINOS), Phys. Rev. Lett. **107**, 181802 (2011), arXiv:1108.0015 [hep-ex].

[49] K. Abe *et al.* (T2K), Phys.Rev.Lett. **112**, 061802 (2014), arXiv:1311.4750 [hep-ex].

[50] F. P. An *et al.* (Daya Bay), Phys. Rev. Lett. **108**, 171803 (2012), arXiv:1203.1669 [hep-ex].

[51] Soo-Bong Kim *et al.* (RENO), Phys. Rev. Lett. **108**, 191802 (2012), arXiv:1204.0626 [hep-ex].

[52] Y. Abe *et al.* (Double Chooz), Phys. Rev. **D86**, 052008 (2012), arXiv:1207.6632 [hep-ex].

[53] F.P. An *et al.* (Daya Bay), Phys.Rev.Lett. **112**, 061801 (2014), arXiv:1310.6732 [hep-ex].

[54] G. L. Fogli, E. Lisi, A. Marrone, D. Montanino, A. Palazzo and A. M. Rotunno, Phys. Rev. D **86**, 013012 (2012) [arXiv:1205.5254 [hep-ph]].

[55] D. Ayres *et al.* (NOvA), hep-ex/0210005.

[56] I. Ambats *et al.* (NOvA), hep-ex/0503053.

[57] R. B. Patterson (NOvA), Nucl.Phys.Proc.Suppl. **235-236**, 151 (2013), arXiv:1209.0716 [hep-ex], XXV International Conference on Neutrino Physics and Astrophysics (Neutrino 2012).

[58] C. Adams *et al.* [LBNE Collaboration], arXiv:1307.7335 [hep-ex].

[59] A. Rubbia, J. Phys. Conf. Ser. **408**, 012006 (2013).

[60] S. Di Luise, PoS ICHEP **2012**, 387 (2013).

[61] S.K. Agarwalla *et al.* (LAGUNA-LBNO), arXiv:1312.6520 [hep-ph].

[62] M. G. Aartsen *et al.* [IceCube-PINGU Collaboration], arXiv:1401.2046 [physics.ins-det].

[63] U. F. Katz [for the KM3NeT Collaboration], [arXiv:1402.1022 [astro-ph.IM]].

[64] K. Abe, T. Abe, H. Aihara, Y. Fukuda, Y. Hayato, K. Huang, A. K. Ichikawa and M. Ikeda *et al.*, arXiv:1109.3262 [hep-ex].

[65] T. Ishida [Hyper-Kamiokande working group Collaboration], arXiv:1311.5287 [hep-ex].

[66] Y. -F. Li, [arXiv:1402.6143 [physics.ins-det]].

[67] International Workshop on"RENO-50" toward Neutrino Mass Hierarchy, 2013, http://home.kias.re.kr/MKG/h/reno50/ .

[68] D. N. Spergel *et al.* [WMAP Collaboration], Astrophys. J. Suppl. **148**, 175 (2003) [astro-ph/0302209].

[69] S. Hannestad, Prog. Part. Nucl. Phys. **65**, 185 (2010) [arXiv:1007.0658 [hep-ph]].

[70] J. Lesgourgues and S. Pastor, Adv. High Energy Phys. **2012**, 608515 (2012) [arXiv:1212.6154 [hep-ph]].

[71] H. V. Klapdor-Kleingrothaus, A. Dietz, L. Baudis, G. Heusser, I. V. Krivosheina, S. Kolb, B. Majorovits and H. Pas *et al.*, Eur. Phys. J. A **12**, 147 (2001) [hep-ph/0103062].

[72] N. Ackerman *et al.* [EXO-200 Collaboration], Phys. Rev. Lett. **107**, 212501 (2011) [arXiv:1108.4193 [nucl-ex]].

[73] C. .Kraus, B. Bornschein, L. Bornschein, J. Bonn, B. Flatt, A. Kovalik, B. Ostrick and E. W. Otten *et al.*, Eur. Phys. J. C **40**, 447 (2005) [hep-ex/0412056].

[74] J. Wolf [KATRIN Collaboration], Nucl. Instrum. Meth. A **623**, 442 (2010) [arXiv:0810.3281 [physics.ins-det]].

[75] M. S. Athar *et al.* [INO Collaboration], INO-2006-01.

[76] M. M. Devi, A. Ghosh, D. Kaur, L. S. Mohan, S. Choubey, et al., *Hadron energy response of the Iron Calorimeter detector at the India-based Neutrino Observatory*, *JINST* **8** (2013) P11003, [`arXiv:1304.5115`].

[77] A Simulations Study of the Response of ICAL Detector to Muons
Animesh Chatterjee, Meghna K, Kanishka Rawat, Tarak Thakore, et al.,
JINST **9**, P07001 (2014) [arXiv:1405.7243 [physics.ins-det]].

[78] R. Santonico and R. Cardarelli, Nucl. Instrum. Meth. **187**, 377 (1981).

[79] B. Satyanarayana, *Design and Characterisation Studies of Resistive Plate Chambers*, PhD thesis, (Department of Physics, IIT Bombay, PHY-PHD-10-701, 2009).

[80] Infolytica Inc., http://www.infolytica.com/en/products/magnet/

[81] John Marshall, A New Track Finding Package, MINOS doc-2104.

[82] John Marshall, A study of muon neutrino disappearance with the MINOS detectors and the NuMI neutrino beam, Fermilab-Thesis-2008-20, MINOS-doc-4849.

[83] S. Agostinelli *et al.* [GEANT4 Collaboration], Nucl. Instrum. Meth. A **506**, 250 (2003).

[84] Kalman R. E., Transactions of the ASME – Journal of Basic Engineering, 82 (1960).

[85] G. Welch, G. Bishop, Technical Report (1995), University of North Carolina at Chapel Hill.

[86] E. J. Wolin and L. L. Ho, Nucl. Instrum. Meth. A **329**, 493 (1993).

[87] Fujii, K., Extended Kalman Filter. Refernce Manual, http://www-jlc.kek.jp/subg/offl/kaltest/

[88] S. Seun, Muon Swimmer Package, based on 'Numerical Reciipes' section 16.2, Adaptive Stepsize Control for Runge-Kutta.

[89] G. Battistoni, A. Ferrari, P. Lipari, T. Montaruli, P. R. Sala and T. Rancati, Astropart. Phys. **12**, 315 (2000) [hep-ph/9907408].

BIBLIOGRAPHY

[90] M. Honda, T. Kajita, K. Kasahara and S. Midorikawa, Phys. Rev. D **83**, 123001 (2011) [arXiv:1102.2688 [astro-ph.HE]].

[91] G. D. Barr, T. K. Gaisser, P. Lipari, S. Robbins and T. Stanev, Phys. Rev. D **70**, 023006 (2004) [astro-ph/0403630].

[92] G. Battistoni, A. Ferrari, T. Montaruli and P. R. Sala, Astropart. Phys. **19**, 269 (2003) [Erratum-ibid. **19**, 291 (2003)] [hep-ph/0207035].

[93] M. Sajjad Athar, M. Honda, T. Kajita, K. Kasahara and S. Midorikawa, Phys. Lett. B **718**, 1375 (2013) [arXiv:1210.5154 [hep-ph]].

[94] J. A. Formaggio and G. P. Zeller, Rev. Mod. Phys. **84**, 1307 (2012) [arXiv:1305.7513 [hep-ex]].

[95] L. Alvarez-Ruso, Y. Hayato and J. Nieves, arXiv:1403.2673 [hep-ph].

[96] J. Beringer *et al.* [Particle Data Group Collaboration], Phys. Rev. D **86**, 010001 (2012).

[97] D. Casper, Nucl. Phys. Proc. Suppl. **112**, 161 (2002) [hep-ph/0208030].

[98] X. Qian, A. Tan, W. Wang, J. J. Ling, R. D. McKeown and C. Zhang, Phys. Rev. D **86**, 113011 (2012) [arXiv:1210.3651 [hep-ph]].

[99] E. Ciuffoli, J. Evslin and X. Zhang, JHEP **1401**, 095 (2014) [arXiv:1305.5150 [hep-ph]].

[100] M. Blennow, P. Coloma, P. Huber and T. Schwetz, arXiv:1311.1822 [hep-ph].

[101] M. Blennow, JHEP **1401**, 139 (2014) [arXiv:1311.3183 [hep-ph]].

[102] G. Cowan, K. Cranmer, E. Gross and O. Vitells, Eur. Phys. J. C **71**, 1554 (2011) [arXiv:1007.1727 [physics.data-an]].

[103] A. M. Dziewonski and D. L. Anderson, Phys. Earth Planet. Interiors **25**, 297 (1981).

[104] V. D. Barger, K. Whisnant, S. Pakvasa and R. J. N. Phillips, Phys. Rev. D **22**, 2718 (1980).

[105] R. Brun, F. Rademakers, Proceedings AIHENP'96 Workshop, Lausanne, Sep. 1996, Nucl. Inst. & Meth. in Phys. Res. A 389 (1997) 81-86. See also http://root.cern.ch/.

[106] Cash W., ApJ **228**, 939 (1982).

[107] M. C. Gonzalez-Garcia and M. Maltoni, Phys. Rev. D **70**, 033010 (2004) [hep-ph/0404085].

[108] R. N. Cahn, D. A. Dwyer, S. J. Freedman, W. C. Haxton, R. W. Kadel, Y. .G. Kolomensky, K. B. Luk and P. McDonald *et al.*, arXiv:1307.5487 [hep-ex].

[109] E. Ciuffoli, J. Evslin and X. Zhang, Phys. Rev. D **88**, no. 3, 033017 (2013) [arXiv:1302.0624 [hep-ph]].

[110] A. B. Balantekin, H. Band, R. Betts, J. J. Cherwinka, J. A. Detwiler, S. Dye, K. M. Heeger and R. Johnson *et al.*, arXiv:1307.7419 [hep-ex].

[111] J. Bernabeu, S. Palomares-Ruiz, A. Perez and S. T. Petcov, Phys. Lett. B **531**, 90 (2002) [hep-ph/0110071].

[112] M. C. Gonzalez-Garcia and M. Maltoni, Eur. Phys. J. C **26**, 417 (2003) [hep-ph/0202218].

[113] J. Bernabeu, S. Palomares Ruiz and S. T. Petcov, Nucl. Phys. B **669**, 255 (2003) [hep-ph/0305152].

[114] O. L. G. Peres and A. Y. .Smirnov, Nucl. Phys. B **680**, 479 (2004) [hep-ph/0309312].

[115] S. Palomares-Ruiz and S. T. Petcov, Nucl. Phys. B **712**, 392 (2005) [hep-ph/0406096].

[116] D. Indumathi and M. V. N. Murthy, Phys. Rev. D **71**, 013001 (2005) [hep-ph/0407336].

[117] R. Gandhi, P. Ghoshal, S. Goswami, P. Mehta and S. U. Sankar, Phys. Rev. D **73**, 053001 (2006) [hep-ph/0411252].

[118] S. Choubey and P. Roy, Phys. Rev. D **73**, 013006 (2006) [hep-ph/0509197].

[119] S. T. Petcov and T. Schwetz, Nucl. Phys. B **740**, 1 (2006) [hep-ph/0511277].

[120] D. Indumathi, M. V. N. Murthy, G. Rajasekaran and N. Sinha, Phys. Rev. D **74**, 053004 (2006) [hep-ph/0603264].

[121] S. Choubey, Nucl. Phys. Proc. Suppl. **221**, 46 (2011) [hep-ph/0609182].

[122] E. K. Akhmedov, M. Maltoni and A. Y. .Smirnov, JHEP **0705**, 077 (2007) [hep-ph/0612285].

[123] R. Gandhi, P. Ghoshal, S. Goswami, P. Mehta, S. U. Sankar and S. Shalgar, Phys. Rev. D **76**, 073012 (2007) [arXiv:0707.1723 [hep-ph]].

[124] E. K. .Akhmedov, M. Maltoni and A. Y. .Smirnov, JHEP **0806**, 072 (2008) [arXiv:0804.1466 [hep-ph]].

[125] R. Gandhi, P. Ghoshal, S. Goswami and S. U. Sankar, Phys. Rev. D **78**, 073001 (2008) [arXiv:0807.2759 [hep-ph]].

[126] A. Samanta, Phys. Rev. D **81**, 037302 (2010) [arXiv:0907.3540 [hep-ph]].

[127] A. Samanta and A. Y. .Smirnov, JHEP **1107**, 048 (2011) [arXiv:1012.0360 [hep-ph]].

[128] M. C. Gonzalez-Garcia, M. Maltoni and J. Salvado, JHEP **1105**, 075 (2011) [arXiv:1103.4365 [hep-ph]].

[129] V. Barger, R. Gandhi, P. Ghoshal, S. Goswami, D. Marfatia, S. Prakash, S. K. Raut and S U. Sankar, Phys. Rev. Lett. **109**, 091801 (2012) [arXiv:1203.6012 [hep-ph]].

[130] M. Blennow and T. Schwetz, JHEP **1208**, 058 (2012) [arXiv:1203.3388 [hep-ph]].

[131] R. Gandhi, P. Ghoshal, S. Goswami, P. Mehta and S. U. Sankar, Phys. Rev. D **73**, 053001 (2006) [hep-ph/0411252].

[132] D. Franco, C. Jollet, A. Kouchner, V. Kulikovskiy, A. Meregaglia, S. Perasso, T. Pradier and A. Tonazzo *et al.*, JHEP **1304**, 008 (2013) [arXiv:1301.4332 [hep-ex]].

[133] H. Nunokawa, S. J. Parke and R. Zukanovich Funchal, Phys. Rev. D **72**, 013009 (2005) [hep-ph/0503283].

[134] E. K. Akhmedov, R. Johansson, M. Lindner, T. Ohlsson and T. Schwetz, JHEP **0404**, 078 (2004) [hep-ph/0402175].

[135] P. Huber, M. Lindner, T. Schwetz and W. Winter, JHEP **0911**, 044 (2009) [arXiv:0907.1896 [hep-ph]].

[136] Y. Itow, SK Collaboration, "SK results presented at Neutrino 2012", http://neu2012.kek.jp.

[137] P. Adamson *et al.* [MINOS Collaboration], Phys. Rev. D **86**, 052007 (2012) [arXiv:1208.2915 [hep-ex]].

[138] T. Dealtry, T2K Collaboration, "Muon neutrino disappearance at T2K", http://indico.cern.ch/contributionDisplay.py?contribId=36&sessionId=12&confId=214998.

[139] K. Abe *et al.* (T2K), arXiv:1403.1532 [hep-ex].

[140] S. Choubey and P. Roy, Phys. Rev. D **73**, 013006 (2006) [hep-ph/0509197].

[141] V. Barger, R. Gandhi, P. Ghoshal, S. Goswami, D. Marfatia, S. Prakash, S. K. Raut and S U. Sankar, Phys. Rev. Lett. **109**, 091801 (2012) [arXiv:1203.6012 [hep-ph]].

[142] D. Indumathi, M. V. N. Murthy, G. Rajasekaran and N. Sinha, Phys. Rev. D **74**, 053004 (2006) [hep-ph/0603264].